Digital Comprehensive Summaries of Uppsala Dissertations
from the Faculty of Science and Technology 2716

Atomic Layer Deposition of Thin Films for Perovskite Solar Cells

Transport and Passivation Layers

BHAVYA RAKHEJA

ACTA UNIVERSITATIS
UPSALIENSIS
2026

ISSN 1651-6214
ISBN 978-91-513-2961-1
urn:nbn:se:uu:diva-598586

UPPSALA
UNIVERSITET

Dissertation presented at Uppsala University to be publicly examined in Siegbahnsalen, Lägerhyddsvägen 1, Uppsala, Friday, 6 November 2026 at 13:15 for the degree of Doctor of Philosophy. The examination will be conducted in English. Faculty examiner: Professor Feng Gao (Department of Physics, Chemistry and Biology, Linköping University, Linköping, 58183 Sweden).

Abstract

Rakheja, B. 2026. Atomic Layer Deposition of Thin Films for Perovskite Solar Cells. Transport and Passivation Layers. *Digital Comprehensive Summaries of Uppsala Dissertations from the Faculty of Science and Technology* 2716. 107 pp. Uppsala: Acta Universitatis Upsaliensis. ISBN 978-91-513-2961-1.

Over the past two decades, lead halide perovskite solar cells (PSCs) have matured from laboratory-scale technology to industrial application. State-of-the-art PSCs employ a p-i-n architecture comprising C_{60} and SnO_x electron transport layers (ETLs) atop perovskite. This thesis focuses on the investigation of SnO_x and AlO_x by Atomic layer deposition (ALD) for PSC applications and on understanding the ETL interfaces.

SnO_x ALD using tetrakis(dimethylamido)tin (TDMASn) and H_2O reactants, is investigated with respect to film properties, device performance, and interfacial chemistry. X-ray photoelectron spectroscopy (XPS) studies reveal that TDMASn renders the direct deposition of SnO_x on perovskite unsuitable. On $FAPbI_3$ and $FAPbBr_3$ surfaces, TDMASn induces FA^+ deprotonation, and further degradation. $FAPbI_3$ partially decomposes into PbI_2 and subsequently undergoes phase degradation, whereas TDMASn reacts with $FAPbBr_3$, causing Br^- migration into the SnO_x layer. These reactions preclude the SnO_x ALD on perovskites, making C_{60} a necessary yet imperfect solution due to its mechanical limitations and potential to induce non-radiative recombination at the perovskite/C_{60} interface.

For PSCs incorporating C_{60} between the perovskite and SnO_x, the H_2O dose used during SnO_x ALD plays a crucial role. High H_2O dose enables barrier-free transport and efficient PSC performance, whereas a low H_2O dose results in SnO_x with a slightly lower electron affinity value and oxide trap charges, which limits device performance. Furthermore, SnO_x growth on perovskite/C_{60} stacks can still introduce degradation pathways. Operando ambient-pressure XPS studies indicate the occurrence of halide migration through defects or the bulk of C_{60} during the SnO_x ALD, particularly in mixed iodide-bromide and pure-bromide compositions.

ALD AlOx interfacial treatment between the perovskite and C_{60} results in a similar V_{OC} with a slightly lower FF compared to reference PSCs, while providing a more stable power conversion efficiency. AlO_x ALD on perovskite causes surface alterations similar to those observed for SnO_x, including FA^+ deprotonation and interaction between the Al-precursor (trimethylaluminum) and Br- ions, which may contribute to the reduced FF. Overall, this thesis reveals challenges arising from ALD precursor reactivity and highlights the need for C_{60}-free compact layers that protect perovskites during SnO_x growth and eliminate the need for interfacial treatments at the perovskite/C_{60} interface.

Keywords: Perovskite Solar Cells, Atomic Layer Deposition, X-ray Photoelectron Spectroscopy, Surfaces and Interfaces

Bhavya Rakheja, Department of Materials Science and Engineering, Solar Cell Technology, Box 35, Uppsala University, SE-751 03 Uppsala, Sweden.

© Bhavya Rakheja 2026

ISSN 1651-6214
ISBN 978-91-513-2961-1
URN urn:nbn:se:uu:diva-598586 (http://urn.kb.se/resolve?urn=urn:nbn:se:uu:diva-598586)

To my family

List of Papers

This thesis is based on the following papers, which are referred to in the text by their Roman numerals.

I. **Rakheja, B.**, Hultqvist, A., Druenen, M. V., Törnblom, P., Larsson, F., Olsson, J., Hägglund, C., Johannesson, E., Duda, L., Rensmo, H., Johansson, E. M. J., Wallin, E., Törndahl, T. (2026) Investigation of Tin Oxide Atomic Layer Deposition on the Performance of Evaporated Perovskite Solar Cells. *Small*, e75573. https://doi.org/10.1002/smll.75573

II. **Rakheja, B.**, Hultqvist, A., Varma, R. M., Martin, N. M., Radetzky, K., Riva, S., Johannesson, E., Cappel, U. B., Rensmo, H., Johansson, E. M. J., Törndahl, T. (2025) Interfacial Chemistry between Formamidinium Lead Trihalide Perovskites and Atomic-Layer-Deposited Tin Oxide. *ACS Applied Energy Materials*, 8 (12): 8467–8478. https://doi.org/10.1021/acsaem.5c00968

III. **Rakheja, B.**, Martin, N. M., Hultqvist, A., Donzel-Gargand, O., Larsson, F., Druenen, M. V., Kokkonen, E., Johansson, E. M. J., Wallin, E., Törndahl, T. (2026) Ion Migration and Interface Evolution During in situ Growth of SnO_x on Perovskite/C_{60}: An Ambient Pressure X-ray Photoelectron Spectroscopy Study. *Journal of Materials Chemistry A*, 14 (48): 32966–32976. https://doi.org/10.1039/d6ta02190e

IV. **Rakheja, B.**, Li, B., Maniyarasu, S., Tockhorn, P., Hultqvist, A., Törndahl, T., Korte, L. (2026) Aluminum Oxide Interfacial treatment in Perovskite Solar Cells. *In manuscript.*

Papers are reproduced under the terms of the Creative Commons Attribution 4.0 International License (CC-BY 4.0), https://creativecommons.org/licenses/by/4.0/.

Contribution

- Paper I

  Performed most of the experimentation by preparing thin films by ALD, including part of the solar cell stack in collaboration with First Solar ETC AB. Conducted most of the materials and electrical characterization and part of the solar cell characterization. Mr. Pontus Törnblom supported with RIXS measurements and Dr. Adam Hultqvist supported with MOS fabrication. Analyzed the whole data, wrote and prepared the manuscript.

- Paper II

  Synthesized perovskite structures, including solar cell structures. Conducted solar cell measurements and materials characterization. Performed atomic layer deposition together with Dr. Adam Hultqvist. Conducted laboratory-based XPS measurements with Dr. Natalia M. Martin. Performed data analysis, wrote and prepared the manuscript.

- Paper III

  Conducted most of the experimental work. Performed ambient-pressure XPS measurements at MAX IV, Lund together with Dr. Natalia M. Martin, Dr. Adam Hultqvist, and Dr. Tobias Törndahl. Analyzed the whole data, wrote and prepared the manuscript.

- Paper IV

  Conducted XPS measurements at the Helmholtz-Zentrum Berlin für Materialien und Energie, Berlin, analyzed the resulting data, and wrote and prepared the manuscript.

Extended Bibliography

Contributed work during my postgraduate studies but not included in this thesis.

1. Varma, R.M., **Rakheja, B.**, Radetzky, K., Johannesson, E., Riva, S., García-Fernández, A., Félix, R., Hultqvist, A., Mukherjee, S., Cappel, U. B., Törndahl, T. & Rensmo, H. (2026) Energy Band Alignment and Interfaces in $FAPbI_3$ Perovskite Solar Cells: A Hard X-ray Photoelectron Spectroscopy Investigation. *ACS Applied Materials & Interfaces*, 18 (30): 42112–42124. https://doi.org/10.1021/acsami.6c08990

2. Prakash, S., Hägglund, C., Zhan, S., **Rakheja, B.**, Boschloo, G., & Mamedov, F. (2026) Characterization of F4TCNQ as a dopant in spiro-OMeTAD thin films by electron paramagnetic resonance spectroscopy. *Physical Chemistry Chemical Physics*, 28 (13): 7973–7983. https://doi.org/10.1039/d5cp04633e

3. Kumar, R., **Rakheja, B.**, Lamminen, N., Fasulo, F., Cachafeiro, M. A. T., Hanmandlu, C., Grandhi, G. K., Bag, M., Muñoz-García, A. B., Boschloo, G., Tress, W., Pavone, M., Vivo, P., & Johansson, E. M. J. (2025) Mechanistic Insights into Ionic Conduction in Lead Halide Perovskites and Perovskite-Inspired Materials. *Advanced Energy Materials*, 15 (45): e03331. https://doi.org/10.1002/aenm.202503331

4. Kumar, R., Beniwal, S., Suhail, A., **Rakheja, B.**, Bag, M., & Johansson, E. M. J. (2024) Controlling Electronic-Ionic Kinetics via Size Engineering in $CsPbBr_3$ Perovskite Nanocrystals. *The Journal of Physical Chemistry C*, 128 (33): 13917–13925. https://doi.org/10.1021/acs.jpcc.4c02991

Contents

1 Introduction 15
1.1 Semiconductor Physics 15
1.2 Perovskites 18
1.2.1 Crystal Structure 19
1.2.2 Electronic Structure 20
1.3 Solar Cells 21
1.3.1 P-N junction 21
1.3.2 Solar Cell Operation 23
1.3.3 Perovskite Solar Cell Structure 25
1.3.4 Tandem Solar Cells 27
1.3.5 Ion Migration 27

2 Atomic Layer Deposition 29
2.1 Properties of Atomic Layer Deposition 30
2.2 Atomic Layer Deposition in Perovskite Solar Cells 31
2.2.1 Electron Transport Layers 32
2.2.2 Hole Transport Layers 34
2.2.3 Passivation Layers 35

3 Scope of the Thesis 37

4 Experimental Details 40
4.1 Solar Cell Fabrication 40
4.1.1 Substrate Preparation 41
4.1.2 HTL Deposition 41
4.1.3 Perovskite Deposition 41
4.1.4 ETL Deposition 42
4.2 Metal-Oxide-Semiconductor Fabrication 43
4.3 Material Characterization 44
4.3.1 Photoemission Spectroscopy 44
4.3.2 *In situ* Quartz Crystal Microbalance 46
4.3.3 X-ray Diffraction 47
4.3.4 X-ray Reflectivity 49
4.3.5 Scanning Electron Microscopy 50
4.3.6 Optical Measurements 51

4.4 Device Characterization 52
4.4.1 J-V Measurements 52
4.4.2 External Quantum Efficiency 53

5 Results and Discussion 54
5.1 Tin oxide Properties and its Optimization for Incorporation in p-i-n PSCs 54
5.1.1 Development of the ALD Process 54
5.1.2 Physical Properties 55
5.1.3 Chemical Properties 56
5.1.4 Optical Properties 59
5.1.5 Electronic Properties 60
5.1.6 Solar Cell Performance 61
5.2 Electron Transport Layer Interfaces in p-i-n PSCs 66
5.2.1 ALD of Tin Oxide on Perovskite 66
5.2.2 ALD of Tin Oxide on Perovskite/C_{60} 72
5.3 Passivation Layer by ALD in p-i-n PSCs 81
5.3.1 Interfacial Chemistry 81
5.3.2 Solar Cell Analysis 84

6 Conclusion and Outlook 87

7 Acknowledgments 91

8 Popular Science Summary 94

9 Populärvetenskaplig sammanfattning 96

10 References 98

Declaration of AI Use

Generative Artificial Intelligence (Microsoft copilot) was solely used for improving the language and correcting grammatical errors.

Abbreviations

GW	Gigawatts
PV	Photovoltaics
PSC	Perovskite solar cells
VB	Valence band
E_G	Band gap
E_F	Fermi-energy
ϕ	Work-function
χ	Electron affinity
CB	Conduction band
MHP	Metal halide perovskite
PCE	Power conversion efficiency
FA^+	Formamidinium cation
MA^+	Methylammonium cation
t	Goldschmidt tolerance factor
UV	Ultraviolet
IR	Infrared
AM	Air mass
SCR	Space charge region
V_{bi}	Built-in potential
J_{pn}	Current density
V_{pn}	Applied bias
J_o	Reverse saturation current density
k_b	Boltzmann constant
T	Temperature
L_e	Electron diffusion length
L_h	Hole diffusion length
J_L	Photocurrent density
J_{SC}	Short circuit current density
V_{OC}	Open circuit voltage
MPP	Maximum power point
P_{MPP}	Maximum power point density
V_{MPP}	Maximum power point voltage
J_{MPP}	Maximum power point current density

P_{in}	Input power density
FF	Fill factor
SQ	Shockley-Queisser
ETL	Electron transport layer
HTL	Hole transport layer
CIGS	Copper indium gallium selenide
CdTe	Cadmium telluride
CTL	Charge transport layer
TCO	Transparent-conductive-oxide
SLG	Soda lime glass
spiro-OMeTAD	2,2',7,7'-Tetrakis[N,N-di(4-methoxy-phenyl)amino]-9,9'-spirobifluorene
PTAA	Poly[bis(4-phenyl)(2,4,6-trime-thylphenyl)amine]
PEDOT:PSS	Poly(3,4-ethylenedioxythiophene) polystyrene sulfonate
SAM	Self-assembled monolayer
C_{60}	Fullerene
PCBM	Phenyl-C61-butyric acid methyl ester
2T	Two-terminal
4T	Four-terminal
PEA^+	Phenylethyl ammonium cation
2D	Two-dimensional
ALD	Atomic layer deposition
CVD	Chemical vapor deposition
GPC	Growth-per-cycle
TDMASn	Tetrakis(dimethylamino) tin (IV)
DEZn	Diethylzinc
XPS	X-ray photoelectron spectroscopy
VO_x	Vanadium oxide
$NiCp_2$	Bis(cyclopentadienyl)nickel
$Ni(MeCp)_2$	Bis(ethylcyclopentadienyl)nickel
MeO-2PACz	[2-(3,6-dimethoxy-9H-carbazol-9-yl)ethyl]phosphonic acid
$Ni(^tBu\text{-}MeAMD)_2$	bis(N,N'-di-tert-butylacetamidinato)nickel
ITO	Indium-tin-oxide
2PACz	[2-(9H-carbazol-9-yl)ethyl]phosphonic acid
TMA	Trimethylaluminum
AIP	Aluminium triisopropoxide
PTFE	Polytetrafluoroethylene

DMSO	dimethyl sulfoxide
DMF	dimethylformamide
FTO	Fluorine-doped tin oxide
RH	Relative humidity
Me-4PACz	[4-(3,6-Dimethyl-9H-carbazol-9-yl)butyl]phosphonic acid
PFN-Br	Poly(9,9-bis(3'-(N,N-dimethyl)-N-ethylammoinium-propyl-2,7-fluorene)-alt-2,7-(9,9-dioctylfluorene))dibromide
PES	Photoemission spectroscopy or photo electron spectroscopy
KE	Kinetic energy
hv	Photon energy
BE	Binding energy
SOXPES	Soft X-ray photoelectron spectroscopy
HAXPES	Hard X-ray photoelectron spectroscopy
$IMFP$	Inelastic mean free path
AP-XPS	Ambient-pressure X-ray photoelectron spectroscopy
MS	Mass spectrometer
HR	High-resolution
QCM	Quartz crystal microbalance
DMA	Dimethylamine
XRD	X-ray diffraction
XRR	X-ray reflectivity
SEM	Scanning electron microscopy
EHT	Electron high tension
PL	Photoluminescence
T	Transmittance
R	Reflectance
EQE	External quantum efficiency
$\Phi_{AM\ 1.5G}$	Spectra irradiance of AM 1.5G solar spectrum
RIXS	Resonant inelastic X-ray scattering
SE	Spectroscopic ellipsometry
VBM	Valence band minimum
MOS	Metal-oxide-semiconductor
HI	Hysteresis index
STEM	Scanning transmission electron microscopy
FIB	Focused-ion beam

1 Introduction

The global energy mix is currently dominated by non-renewable energy sources, which account for ~81% of the total mix.[1] However, on the bright side, the contribution of renewable energy sources in the energy mix has been growing rapidly in recent years. Based on the International Energy Agency's report, the installed capacity of renewable energy is predicted to increase by 4600 gigawatts (GW) by 2030, with solar photovoltaics (PV) accounting for 80% of this increase.[2] Commercial solar cells are primarily based on the well-established silicon technology. Nevertheless, the exploration of new cost-effective and efficient solar cell materials remains an active research interest for the PV community. In the late 2000s, perovskite solar cells (PSCs) emerged as a new class of PV materials, with an efficiency of only 3.8%.[3] Now, almost two decades later, the world-record efficiency of PSCs have reached levels comparable to those of silicon-based solar cells.

This thesis focuses on the development of PSCs and aims to establish an understanding on how their performance is influenced by the properties of the charge transport layers (CTLs) employed within the device architecture, as well as by the interfaces that form between the different layers of the device stack. Before discussing the experimental work and the key findings of this thesis, this chapter first provides a systematic introduction to the fundamental concepts of semiconductor physics, the properties of perovskite material, and the principles of PSC operation.

1.1 Semiconductor Physics

The optoelectronic properties of a material are based on its respective band structure, which is derived from quantum mechanics. The energy-momentum ($E-k$) relationship that defines the band structure is derived by solving the one-electron Schrödinger equation as given below:

$$\left[\frac{-\hbar^2}{2m_0}\nabla^2 + V(r)\right]\psi(r) = E\psi(r)$$

Here, $\hbar$, m_0, and r correspond to the reduced Planck's constant, the mass of a stationary electron, and the position vector, respectively. $\psi(r)$ is the electron wave function described over space. $V(r)$ is the potential experienced by the electron in the periodic crystal lattice and E is the electron energy. The potential, $V(r)$, is considered periodic in nature due to the lattice periodicity of the crystal. The Kronig-Penney model is further used as a simplification tool to handle the complexity of a real crystal system by introducing a potential function as a one-dimensional array of periodic potential wells and barriers. To find the solutions of the Schrödinger equation in a crystal system, the Bloch theorem is utilized. According to the theorem, the electron wavefunction in a crystal can be described as a free-electron wavefunction modulated by a periodic function. **Figure 1.1(a)** illustrates the $E-k$ relationship, which is parabolic for an electron in free space (grey dashed line). In crystalline solids, the $E-k$ curve is modified (gold solid curve) due to the presence of the periodic potential, which alters the curvature and results in the formation of forbidden energy regions (energy gaps). The curvature of the $E-k$ dependence is important because it determines the electron effective mass (m^*), whereas the energy gaps limit the energies that electrons can acquire through interactions.

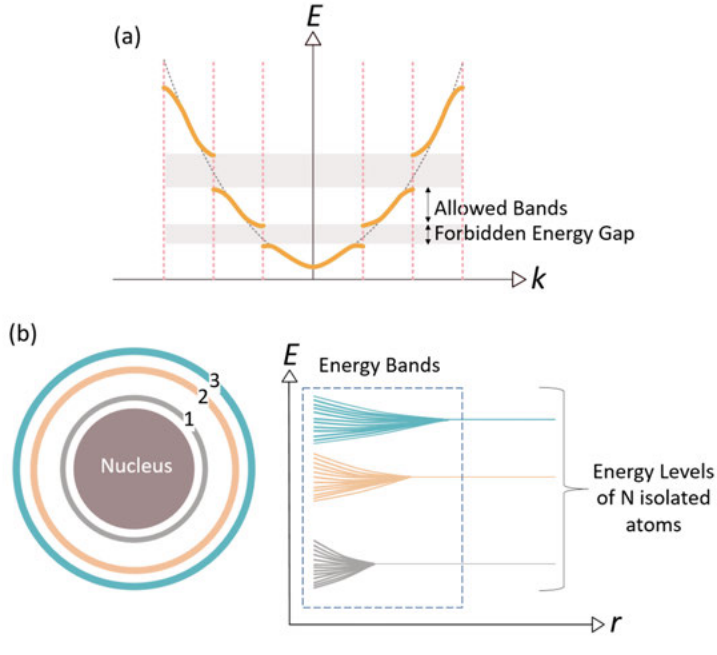

Figure 1.1. (a) $E-k$ relationship for electrons in free space (grey dashed line) and in a crystalline solid (orange solid curve). (b) An isolated atom with 3 energy levels and their splitting into allowed and forbidden bands when N isolated atoms are brought closer.

As shown in **Figure 1.1(b)**, an isolated atom has a series of quantized electronic energy levels, which tend to split into quasi-continuum energy bands when a large number (N) of atoms are tightly packed into a solid. This splitting occurs due to an overlap between the electron wave functions at small interatomic distances (r), leading to chemical bonding (or anti-bonding). Owing to the longest average distance from the nuclei, it is particularly the weakly bound valence electrons that take part in these interactions, whereas the tightly bound core energy levels remain largely unaffected. In a crystal structure, the total number of quantum states is conserved (unchanged compared to N isolated atoms), and based on the Pauli exclusion principle, no two electrons can occupy the same quantum state. As-obtained energy bands and the corresponding electron distribution determine the electronic properties of a material.

As shown in **Figure 1.2**, all crystalline materials can be categorized as metals, semiconductors, and insulators based on the forbidden energy gap between the highest occupied band (valence band) and the lowest unoccupied band (conduction band), referred to as band gap (E_G). In the case of metals, the highest occupied band is partially filled by electrons, meaning that the band gap is equal to zero. In both semiconductors and insulators, the valence band (VB) is completely filled at absolute 0 K. The difference between the two categories is, however, that the former generally has the E_G value below ~3 eV. The Fermi-energy (E_F) represents the energy of electrons present at the highest occupied level at 0 K, and the energy required to eject an electron from E_F to the vacuum level is termed as the work-function (ϕ). In metals, E_F is located within an energy band, thereby making metals good conductors, as electrons can easily transition to unoccupied states under an external electric field. On the other hand, E_F in semiconductors is located within the band gap. The work-function of a semiconductor is dependent on several factors (discussed later) and is therefore not fixed, which makes its quantification ambiguous. However, another closely related quantity, called the electron affinity (χ) is often used. It corresponds to the energy separation between the conduction band (CB) and the vacuum level, as illustrated in **Figure 1.2**.

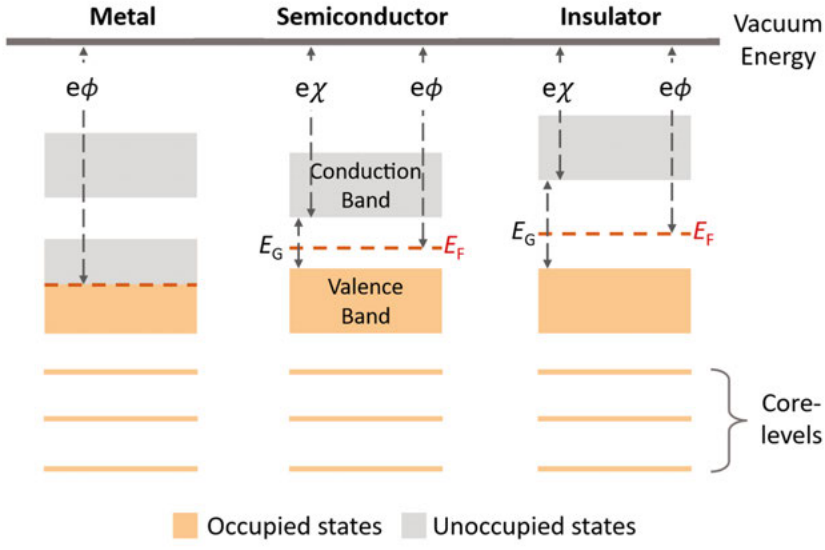

Figure 1.2. Schematic of the energy band diagrams of a metal, a semiconductor, and an insulator.

Semiconductors can be intrinsic or extrinsic in nature. The former class of semiconductors are pure, without the existence of impurities. In extrinsic semiconductors, donor or acceptor impurities are purposely introduced to tailor their properties. Donor atoms have a higher number of valence electrons compared to the atoms of the semiconductor, whereas acceptor atoms have a lower number of valence electrons. Elemental semiconductors with the conductivity dominated by donor impurities are termed "n-type", whereas those containing mostly acceptor impurities are called "p-type". In n-type semiconductors, donor atoms are positively charged and increase the concentration of free-electron charge carriers, making the position of E_F closer to the conduction band minimum. On the contrary, acceptor atoms become negatively charged and create holes in p-type semiconductors, thereby shifting E_F closer to the valence band maximum.

1.2 Perovskites

The perovskite crystal structure has been known since 1839, when it was first discovered in $CaTiO_3$. However, it was only in 2009 that the group of Miyasaka utilized a metal halide perovskite (MHP) as an absorber for the first time in a PV device, and attained a power conversion efficiency (PCE) of 3.8%.[3] Since then, MHPs have experienced an unprecedented growth in the

field of PV, demonstrating PCE values close to the theoretical limit. Such an outstanding progress is a consequence of their exceptional properties, including a sharp absorption onset and high absorption coefficients, long charge-carrier diffusion lengths, and high defect tolerance.[4–6]

1.2.1 Crystal Structure

All perovskites have an ABX_3 chemical formula, and MHPs employed in PV devices generally comprise a group 14 cation, such as Pb^{2+} or Sn^{2+}, at the B-site, while the X-site is occupied by a halide anion (I^-, Br^-, or Cl^-). The A-site is filled by an organic cation, such as formamidinium (FA^+) or methylammonium (MA^+), and/or a heavy inorganic alkali-metal cation such as Cs^+, which balances the charge in the structure.

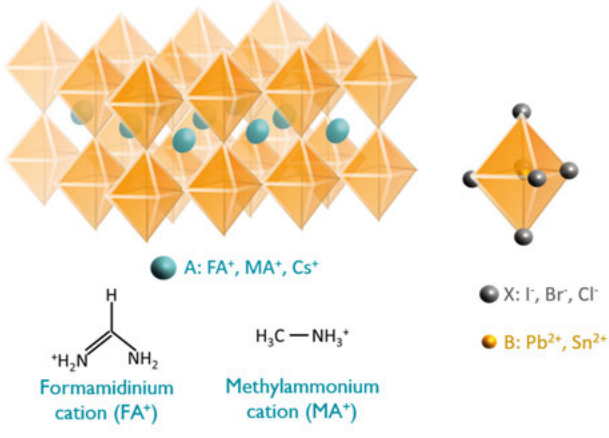

Figure 1.3. Crystal structure of metal halide perovskites.

The structure consists of BX_6^{4-} units that form octahedra, and the A-site cation lies in the formed cuboctahedra voids, as illustrated in **Figure 1.3**. The structural stability of a perovskite structure is governed by the ionic radii of the A-site and B-site cations, as well as the X-site anion, through the Goldschmidt tolerance factor (t), which is given by the following relation:[7,8]

$$t = \frac{r_A + r_X}{\sqrt{2}(r_B + r_X)}$$

where r_A, r_B, and r_X correspond to the ionic radii of the A, B, and X ions, respectively. The tolerance factor for halide perovskites lies between 0.81 and 1.11, with a stable cubic structure usually existing in the range of 0.89-1.00.[7,9] Compared to this narrow optimum, pure $FAPbI_3$ and $CsPbI_3$ have slightly

larger (>1.0) and smaller (<0.8) tolerance factors, respectively. Thereby, $FAPbI_3$ generally stabilizes in so-called δ-phase at room temperature, which has a hexagonal structure, whereas $CsPbI_3$ occurs in a non-perovskite orthorhombic structure.[10] In order to stabilize the perovskite phase, and to finetune its optoelectronic properties, both cation and anion alloying is readily performed. Specifically, the intermixing of Cs^+ and FA^+ is widely adopted to tune the tolerance factor to form the desired α-$(Cs,FA)PbI_3$ perovskite with improved stability, which exhibits a distorted-cubic structure with an octahedral tilt of ~2°.[10,11] Another well-known strategy to promote the α-phase formation involves the addition of methylammonium chloride (MACl) salt during synthesis of $FAPbI_3$. MA^+ and Cl^- ions from this salt have been suggested to induce volume shrinkage and strengthen the interaction of FA^+ and I^-, thereby stabilizing the intermediate phase and suppressing the formation of the δ-phase.[12,13]

1.2.2 Electronic Structure

MHPs are compound semiconductors with low bulk charge-carrier densities.[14] Interestingly, they offer a unique possibility for band gap tunability through alloying. The top of the VB in MHPs are formed via hybridization between the s-orbitals of the B-site metal and the p-orbitals of the halide, whereas the CB is composed of the p-orbitals of the B-site metal, hybridized with the s- and p-orbitals of the halide.[7,15] However, the A-site cation orbitals do not contribute to either band edge. For example, in the case of $MAPbI_3$, the top-most VB states consist of Pb 6s-I 5p σ-antibonding states, and the bottom-most CB states comprise Pb 6p-I 5s σ-antibonding states.[15]

The $APbX_3$ bandgap increases systematically with a decrease in the size of the halide element. This trend originates from a concurrent upward shift of the CB and downward shift of the VB going from $I^- \rightarrow Br^- \rightarrow Cl^-$. The effect on the CB is associated with an upward shift in Pb 6p orbitals owing to an increased electron confinement in the Pb-X bond, whereas the downward shift of the VB is explained by an increase in the electronegativity of the halide anion.[16]

Substituting Pb with Sn at the B-site also influences the bandgap. Both of the VB and CB positions move upward, with the shift being larger for the VB. Thus, the band gap value has generally been reported to decrease upon exchanging Pb with Sn, with a few exceptions explained by secondary effects such as lattice distortions.[16] In contrast, the effect of the A-site cation substitution is indirect in nature, as it does not contribute to either of the VB or CB edges. However, effects such as octahedral tilting and lattice expansion can

indirectly impact the B-X bonding.[16,17] The band gap and electron affinity values of the MHPs studied in this work, as reported previously in the literature, are tabulated below:

Perovskite	Bandgap (eV)	Electron affinity (eV)	References
$FAPbI_3$	1.5	4.74	[16]
$FAPbBr_3$	2.25	4.51	[16]
$FA_{0.83}Cs_{0.17}PbI_{3-x}Br_x$	1.56 (x=0)-2.07 (x=2.5)	3.95 (x=0), 4.09 (x=0.5), 4.02 (x=1), 4.15 (x=1.5), 4.09 (x=2), and 4.02 (x=2.5)	[18]

1.3 Solar Cells

The PV technology directly converts sunlight into electricity, harnessing energy from the Sun, which is an effectively inexhaustible resource. The solar spectrum outside the Earth's atmosphere is best approximated using a blackbody radiation spectrum at 5800 K with a total irradiance of 1366 W/m^2 distributed over the ultraviolet (UV), visible, and infrared (IR) regions. However, for terrestrial applications, the atmospheric path of sunlight is subjected to atmospheric scattering, and absorption must also be considered. This is done by using so-called air mass (AM) coefficient, defined as the secant of the angle of the sunlight path, as seen by an observer with respect to the zenith. Under standard test conditions (STC) for solar cells, the AM 1.5 Global spectrum is utilized, which has a total solar irradiance of 1000 W/m^2. Here, the term "global" is attributed to a combination of the direct and diffuse parts of the spectrum. In the following sections, the structure and operation concepts of solar cell devices, detailing the mechanism of conversion of sunlight into electricity, are discussed.

1.3.1 P-N junction

A p-n junction forms the basis of a solar cell and it is formed by bringing a p-type and an n-type semiconductor into contact, as shown in **Figure 1.4**. As a consequence of the charge-carrier concentration gradient between the two sides of the junction, free electrons flow toward the p-side, leaving behind positively charged immobile ions, while holes move in the opposite direction, leaving behind negatively charged ions. The flow of charge carriers due to the existence of charge-carrier concentration gradients results in a diffusion current. The remaining immobile charged ions create an electric field pointing

from the n- to p-type material, confined to the so-called space charge region (SCR) or depletion region that stretches into both n-type and p-type sides. This electric field generates a drift current in the opposite direction to the diffusion current. In equilibrium, the two currents balance out each other, and therefore, the overall current becomes zero, and a constant Fermi level gets established. Further, the width of the SCR and the built-in potential (V_{bi}) across the junction are governed by the carrier concentrations in the n-type and p-type semiconductors, with the SCR being wider on the more lightly doped side of the junction.

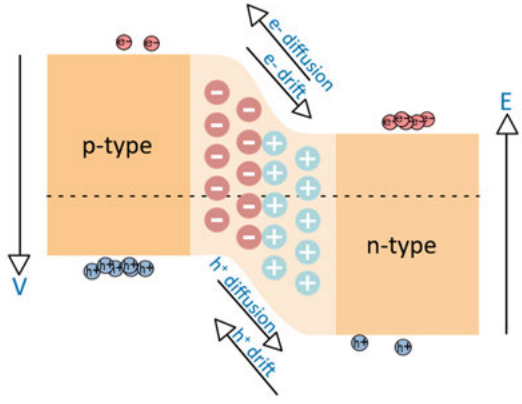

Figure 1.4. Illustration of a p-n junction formation.

Besides doping, external voltage bias also affects the SCR width and the potential drop across the junction. It can also result in a non-zero current as the balance between the diffusion and drift contributions is not maintained. When the p-type side is connected to a higher potential compared to the n-type side, the diffusion current increases due to an increased injection of minority charge carriers, i.e., the injection of electrons into the p-type side and vice-versa. Under this scenario, the applied bias acts in the opposite direction to V_{bi} and, thereby, reduces the SCR width. This case is termed forward bias. On the contrary, when the p-type semiconductor is kept at a lower potential compared to the n-type side, the overall potential drops across the junction and the SCR width increases. The total current through the device is mainly determined by the diffusion of the minority charge carriers toward the SCR region and is considerably smaller compared to the total current in the forward bias condition.

The total current density (J_{pn}) through a p-n junction with respect to the applied bias (V_{pn}) can be described by the so-called ideal diode equation:

$$J_{pn} = J_o\left(e^{\frac{V_{pn}}{k_bT}} - 1\right)$$

Here, J_o is a reverse saturation current density that is determined by the doping density and carrier diffusion lengths (i.e., the average distance that charge carriers can travel before recombining). k_b and T correspond to the Boltzmann constant and temperature, respectively.

1.3.2 Solar Cell Operation

A solar cell is a p-n junction optimized for harnessing solar energy, as shown in **Figure 1.5**. Its operation relies on consecutive processes that involve photon absorption and charge-carrier generation, and charge-carrier separation and extraction.

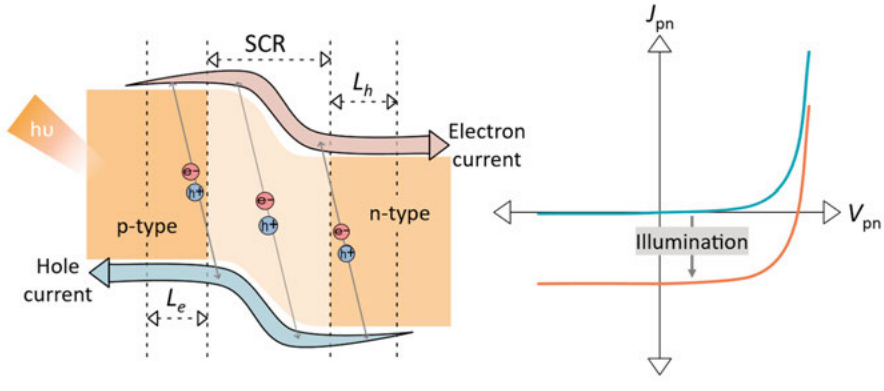

Figure 1.5. A p-n junction under illumination and the corresponding J-V characteristics. L_e and L_h are the electron and hole diffusion lengths, respectively.

Upon illumination, photons with energies greater than or equal to the band gap value get absorbed, and generate electron-hole pairs. The collection probability of the generated electron-hole pairs is unity within the SCR and decreases toward the quasi-neutral regions as a function of the minority charge-carrier diffusion lengths (L_e and L_h). The charge-carriers collected across the junction contribute to a flow of photocurrent (J_L) from the n-type side to the p-type side. Furthermore, continuous illumination causes the photogenerated charge-carriers to accumulate on opposite sides of the junction, with electrons accumulating on the n-type side and holes on the p-type side. As a consequence of this charge-carrier accumulation, a voltage (V_{pn}) develops across the junction in the forward direction, which leads to the flow of a forward current in the direction opposite to that of the photocurrent. Therefore, the overall current of a solar cell is described by the following equations:

$$J_{pn} = J_o\left(e^{\frac{V_{pn}}{k_bT}} - 1\right) - J_L$$

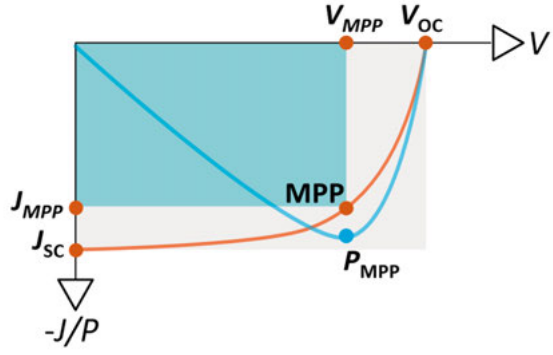

Figure 1.6. Figures-of-merit of a solar cell illustrated using a J-V curve.

As shown in **Figure 1.6**, the highest attainable current density through a solar cell is termed the short-circuit current density (J_{SC}) and is obtained when the voltage across the p-n junction is zero. Similarly, the highest voltage is obtained when the current flowing through the device is zero, i.e., when the forward current and photocurrent become equal, and is referred to as the open-circuit voltage (V_{OC}). The maximum power density (P_{MPP}) is obtained when the product of $V \times J$ is maximized. This condition is termed the maximum power point (MPP), and the corresponding voltage and current density are defined as V_{MPP} and J_{MPP}, respectively. Finally, the power conversion efficiency (PCE) of a solar cell is given by the following relation:

$$PCE = \frac{P_{MPP}}{P_{in}} = \frac{V_{OC} \times J_{SC} \times FF}{P_{in}}$$

Here, P_{in} is the input power density, which is determined by the total solar irradiance. As discussed in section 1.3, its value is 1000 W/m^2 under STC. The fill-factor (FF) is the ratio of the maximum attainable power at the MPP to the product of the V_{OC} and J_{SC}.

The J_{SC} of a high-efficiency solar cell depends primarily on the band gap value of the absorber material, with lower band gap absorbers resulting in higher values, as they can absorb photons over a broader spectral range. In addition to the absorption coefficient, the minority charge-carrier diffusion length is another important parameter that governs the collection probability and, consequently, the total J_{SC} value. Similarly, V_{OC} is also dependent on the band gap

value. However, in contrast to J_{SC}, wide band gap materials result in higher theoretical V_{OC} values due to the existence of a large energetic separation between photogenerated electrons and holes. The V_{OC} is additionally influenced by various recombination mechanisms, which are categorized as radiative, and non-radiative (Auger, and Shockley-Read-Hall). Radiative and Auger recombination are unavoidable, whereas Shockley-Read-Hall recombination can be minimized by controlling defects within the material.

The maximum attainable PCE for a given band gap value is defined by the well-known Shockley-Queisser (SQ) limit. According to this limit, the maximum PCE of a single junction solar cell is ~33%, which can be achieved using an absorber with a band gap value in the range of 1.3-1.4 eV.

1.3.3 Perovskite Solar Cell Structure

A standard PSC consists of multiple layers stacked together, as shown in **Figure 1.7**. The perovskite absorber layer is sandwiched between an electron transport layer (ETL) and a hole transport layer (HTL), which are typically n-type and p-type semiconductors, respectively. Due to the intrinsic nature of the perovskites, PSCs are typically fabricated in a p-i-n configuration rather than in the p-n configuration commonly employed in established PV technologies such as silicon (Si), cadmium telluride (CdTe), and copper indium gallium selenide (CIGS). Although the fundamental principles of solar cell operation remain the same, in an ideal p-i-n structure, nearly the entire absorber is depleted, and the collection probability is governed by the drift length instead of the diffusion length.

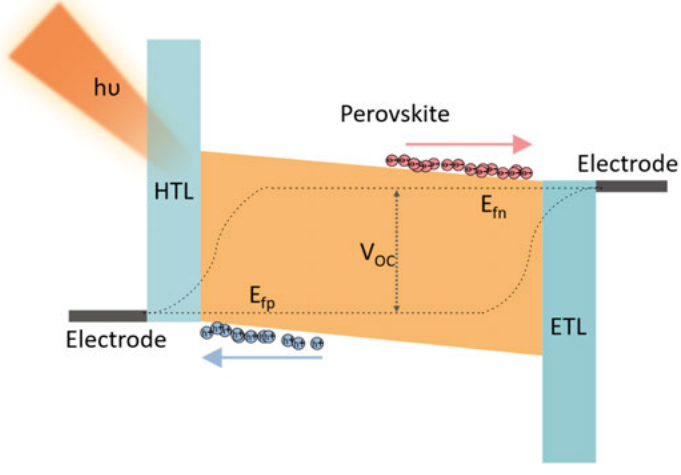

Figure 1.7. Schematic of band profile of a perovskite solar cell.

While the perovskite material serves as the active layer in this structure (**Figure 1.7**), the employed HTL and ETL are equally important for device performance. Their primary function is to provide charge-extraction selectivity by facilitating the transport of one type of charge carrier while blocking the other. The ETL should have its CB aligned with the CB of the perovskite, while simultaneously exhibiting sufficiently wide enough band gap to block hole transport. Similarly, the VB of the HTL should be aligned with the VB of the perovskite, and its electron affinity should be sufficiently lower than that of the absorber to block electron transport. An additional design consideration for the transport layer that acts as the window layer is that it should exhibit high transparency to sunlight, as well as sufficient conductivity to minimize resistive losses. Besides, it is also important that CTLs are chemically compatible with the perovskite material and that the employed deposition process does not adversely affect the underlying layers.

Perovskite Solar Cell Configurations

As shown in **Figure 1.8**, PSCs are commonly fabricated in either n-i-p or p-i-n device architectures, and the two architectures utilize different sets of ETLs and HTLs. The details on both architectures are provided below:

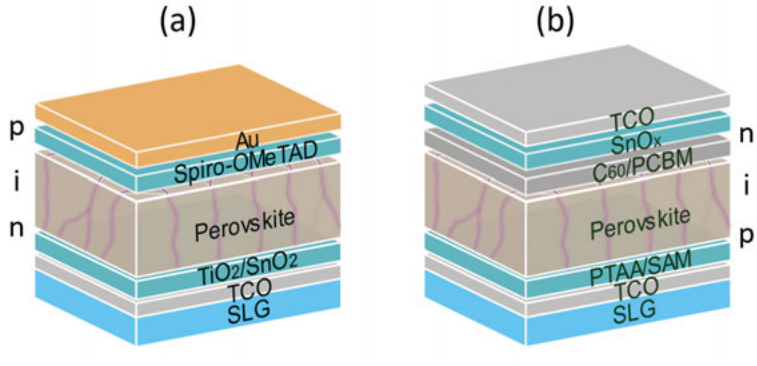

Figure 1.8. (a) n-i-p and (b) p-i-n PSC architectures.

n-i-p

First, a tin-oxide (SnO_2) or titanium dioxide (TiO_2) ETL is deposited on top of a transparent-conductive-oxide (TCO) coated soda-lime-glass (SLG). Following this, the perovskite layer, 2,2',7,7'-Tetrakis[N,N-di(4-methoxyphenyl)amino]-9,9'-spirobifluorene (spiro-OMeTAD)-based HTL and Au electrode are consequently deposited.[19–22] This structure is generally illuminated from the bottom TCO/ETL side. Illumination from the top spiro-OMeTAD side is non-ideal, as it contributes to a significant amount of parasitic absorption.

p-i-n

Here, the HTL is deposited prior to the perovskite deposition step on a TCO substrate. A wide range of HTLs are regularly utilized in p-i-n structures, including nickel oxide (NiO_x), poly[bis(4-phenyl)(2,4,6-trimethylphenyl)amine] (PTAA), poly(3,4-ethylenedioxythiophene) polystyrene sulfonate (PEDOT:PSS) and carbazole-based self-assembled monolayers (SAM). [23–27]. In contrast, the ETL comprises a combination of a fullerene (C_{60}) or a phenyl-C61-butyric acid methyl ester (PCBM) and a SnO_x layer.[21] Unlike n-i-p structures, p-i-n structures can be illuminated from either side because the commonly utilized ETLs and HTLs offer good transparency to solar spectrum. Thereby, p-i-n structures can be made semi-transparent and thus suitable for integration with other solar cell devices for tandem applications.

1.3.4 Tandem Solar Cells

In tandem or multi-junction solar cell structures, two or more solar cells comprising absorbers with different band gap values are stacked on top of each other. These structures employ a wide-band gap-based solar cell as the front cell and a narrow-band gap-based solar cell as the bottom sub-cell. High-energy photons are absorbed by the front cell, while low-energy photos are transmitted and subsequently absorbed by the bottom cell. Therefore, multi-junction solar cells offer a solution for overcoming the SQ limit of single-junction solar cells by mitigating the thermalization and generation losses. Sub-cells are either monolithically integrated to form a two-terminal (2T) configuration or mechanically stacked to form a 4-terminal (4T) configuration.

The band gap tunability of perovskites has made them a key driver of tandem solar cell research. PSCs are particularly well suited as front-cell absorbers in tandem architectures with silicon and CIGS solar cells.[28] Perovskite-silicon tandem solar cells have already exceeded the single-junction SQ limit, achieving PCEs of up to 35%.[29] Furthermore, all-perovskite tandem solar cells are advancing as cost-effective alternatives and have demonstrated efficiencies exceeding 29%.[30,31]

1.3.5 Ion Migration

Unlike traditional PV materials, such as silicon, perovskites are mixed electronic-ionic conductors, which can give rise to anomalous device behavior.[32–34] Ion migration is an intrinsic property of the perovskite lattice itself, and has been identified in both perovskite-type halides and oxides.[35–38] In MHPs, vacancy-mediated iodine migration along the octahedral edges has been reported

as the dominant migration pathway.[38] Ion migration further leads to several phenomena, including hysteresis in J-V characteristics, solar cell degradation, bulk phase segregation, ionic conduction, and light-soaking effects.[32] In PSCs, mobile ions are responsible for modulating the electric field across the solar cell, and consequently influence the device performance.[39] Significant research efforts are therefore focused on improving the understanding of ion migration and developing strategies to mitigate its detrimental effects, and consequently enhance the long-term stability of the PSCs. Van Reenen *et al.* demonstrated that hysteresis originates from the combined effects of mobile ions and interfacial charge traps.[34] Similarly, Calado *et al.* reported that hysteresis arises from the coupling between mobile ions and a high charge-carrier recombination density at the interfaces.[40] These findings suggest that controlling the defects at the perovskite-CTL interfaces can effectively mitigate hysteresis.

In addition to affecting the device operation, ion migration can induce chemical changes that accelerate perovskite degradation. This issue is particularly critical at interfaces, where the perovskite surface can react with the adjacent CTLs or metal electrode under external stressors such as illumination, or external bias. Numerous strategies have been proposed to mitigate ion migration and minimize its adverse effects. For example, compositional engineering through the incorporation of mixed-A-site and B-site ions has been shown to increase the activation energy for iodine migration, thereby slowing its migration down.[41–43] Moreover, large organic cations, such as phenylethyl ammonium cation (PEA^+), are widely employed at the perovskite/transport layer interface. These cations react with the perovskite surface to form a two-dimensional (2D) perovskite overlayer, which can minimize interfacial recombination, and restrict the migration of ions from the perovskite into the transport layer.[44,45]

2 Atomic Layer Deposition

ALD is a form of the chemical vapor deposition (CVD) technique that is based on self-terminating chemical reactions between gas-phase reactants and a solid surface. **Figure 2.1.** demonstrates a standard ALD process, comprising a solid substrate and reactants in the gas phase. An ALD cycle starts with the exposure of precursor molecules, which reacts with the sites present on the surface of the substrate until saturation occurs. Following this, all unreacted precursor molecules and by-products are purged from the ALD chamber. In the next step, a co-reactant is introduced into the chamber, which then reacts with the adsorbed precursor molecules until all are consumed. Subsequently, the co-reactant is purged, allowing the removal of residual co-reactant molecules and by-products. These four steps together form an ALD cycle, which can be repeated several times to obtain the desired film thickness. Owing to the self-limiting nature of the ALD technique, it results in pin-hole free and highly conformal thin films.

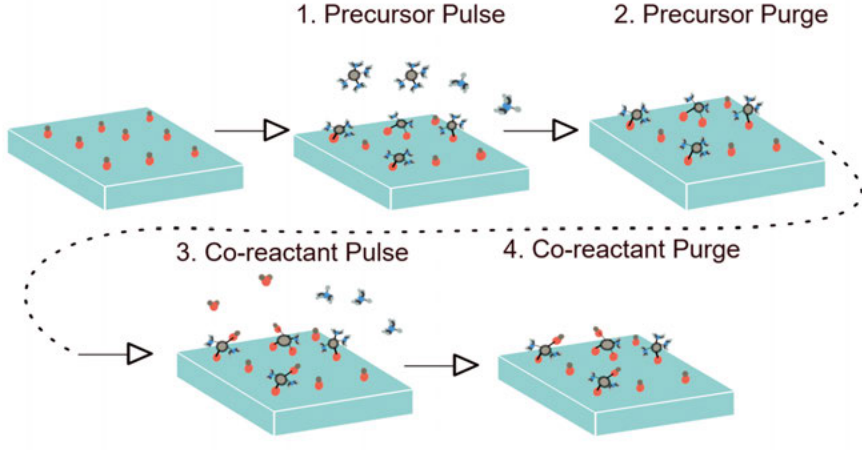

Figure 2.1. Schematic illustrating one cycle of an atomic layer deposition process.

2.1 Properties of Atomic Layer Deposition

An ALD process is developed by constructing saturation curves for the growth-per-cycle (GPC) value with respect to a reactant (precursor or co-reactant) pulse duration, as well as the corresponding purge times, as shown in **Figure 2.2(a)** and **(b)**, respectively. Ideally, the GPC value of a process saturates once the reactant doses or exposure times are sufficient to completely react with the surface. However, lower reactant doses or exposure times could lead to incomplete surface reactions, thus lowering the GPC value. Optimization of purge times facilitates the complete removal of unreacted species before introducing another reactant into the chamber. Excessively short purge times result in the presence of both reactants simultaneously in the gas phase, which can lead to film non-uniformity due to an undesired CVD contribution.

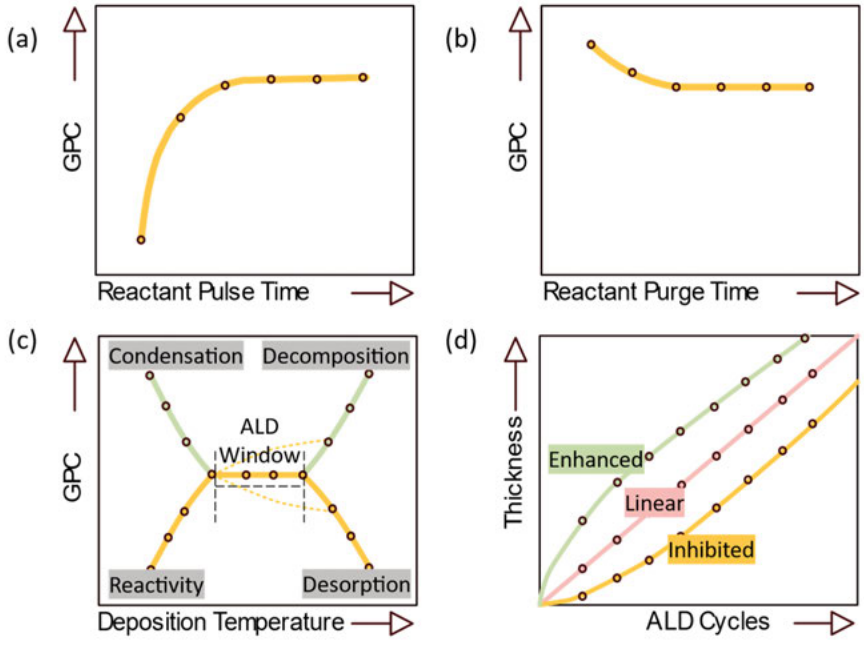

Figure 2.2. Fundamentals of atomic layer deposition. Saturation curves as a function of (a) pulse time and (b) purge time of a reactant (precursor or co-reactant). (c) Influence of deposition temperature on GPC. (d) Evolution of thickness as a function of the number of ALD cycles for different growth regimes.

Figure 2.2(c) demonstrates the impact of the employed deposition temperature on the GPC value for an ALD process. The temperature range within which the GPC value shows saturating behavior is referred to as the ALD window. Temperatures outside the ALD window often result in non-idealities,

as indicated in **Figure 2.2(c)**. An ALD process could display a sharp increase in the GPC value due to precursor decomposition at high deposition temperatures or precursor condensation at low deposition temperatures. Furthermore, the GPC value could also decrease significantly outside the ALD window, owing to the limited reactivity between the reactant and the surface at low temperatures, or due to the desorption of species from the surface at high deposition temperature. The GPC value, as well as the optical, electronic, and material properties, can vary significantly within the ALD window depending on the utilized deposition temperature. Therefore, deposition temperature is one of the most powerful tools for fine-tuning the properties of ALD films based on the targeted application.

At a given deposition temperature, the GPC value is mainly dictated by the number of available surface sites, as well as the steric hindrance experienced by the adsorbates. A combination of these factors often results in the growth of sub-monolayers during an ALD cycle. Besides, an ALD process experiences nucleation effects during the initial cycles, as shown in **Figure 2.2(d)**. Nucleation effects are primarily observed due to a difference in the reactivity of the reactants with the substrate surface and with the film that eventually forms. Nucleation effects could lead to growth inhibition if the substrate surface has a low number of reactive sites, or growth enhancement if the substrate surface has a high number of reactive sites. A linear increase in thickness is often associated with film-on-film growth, where the reactivity between the precursors and the surface does not vary as a function of ALD cycles. Nucleation behavior could influence several properties, including film crystallinity and defect-density at the interface and within the bulk of the grown film.

2.2 Atomic Layer Deposition in Perovskite Solar Cells

Owing to the versatile nature of the ALD technique, it has been widely utilized for the growth of various layers that serve different functions within a PSC structure. So far, ALD has been employed for the fabrication of charge transport layers (CTLs),[46–50] perovskite absorbers,[51] passivation layers,[52–56] and interconnection layers.[57–59] Given the temperature-sensitive and chemically reactive nature of perovskites, the ALD process and the utilized deposition temperature need to be carefully considered depending on the order in which different layers are deposited. Consequently, the growth of layers by ALD following the perovskite deposition within a PSC structure is often more challenging than depositing such layers prior to the perovskite coating. The

following sections provide a detailed discussion on the different ALD-based CTLs and passivation layers that have been incorporated into PSC structures.

2.2.1 Electron Transport Layers

ZnO, TiO_2 and SnO_2 are traditionally some of the most studied metal-oxide ETLs and have also found applications in the domain of perovskite PV. Early n-i-p PSCs originated from dye-synthesized solar cell architectures and therefore incorporated mesoporous TiO_2 as an ETL.[3,60] Here, the TiO_2 structure acted as a scaffold for the subsequent perovskite layer, enabling the formation of an efficient contact with it. However, the mesoporous structure alone was insufficient to block direct contact between the perovskite and the TCO, and, therefore, required an additional compact TiO_2 layer prior to its deposition on the TCO. ALD-grown TiO_2 was demonstrated to be a suitable compact layer that successfully prevented the direct contact between the perovskite and the TCO, thereby efficiently blocked undesired hole transport.[61–63] Even though these strategies significantly improved device performance, challenges concerning the existence of hysteresis and unstable power output remained.[64,65] Furthermore, the increased complexity of the PSC structure, as well as the utilization of mesoporous TiO_2, posed significant challenges to PSC scalability. In order to address these issues, Baena *et al*. demonstrated the incorporation of a SnO_2 layer grown by ALD in planar n-i-p structures, which resulted in an improved PSC performance with almost no hysteresis in the *J-V* measurements.[66] Such an improvement was ascribed to the existence of a deeper conduction band in SnO_2 compared with TiO_2, which facilitated barrier-free electron transport due to an improved conduction band alignment at the SnO_2/perovskite interface. Two years later, Hu and co-authors also demonstrated the importance of ALD process parameters for regulating the interfacial dipole moment between the SnO_x and the perovskite layer.[46] In their study, tetrakis(dimethylamino) tin (IV) (TDMASn) was utilized as the metal precursor, and the effects of water, ozone and oxygen plasma co-reactants were studied. The co-reactant was reported to significantly influence the electron extraction-barrier between the SnO_x layer and the formed interfacial PbI_2, with the ozone and water-based SnO_x layers resulting in the lowest and highest barriers, respectively. Furthermore, Lee *et al.* conducted a comparison of SnO_x layers grown using ALD with H_2O and H_2O_2 as co-reactants for n-i-p PSCs.[67] The films, grown using H_2O_2, were found to improve electron-extraction efficiency in comparison with those prepared using H_2O. It was suggested that H_2O_2-based SnO_x exhibits fewer oxygen vacancies due to the oxidizing nature of H_2O_2. Despite the implementation of various ALD-only strategies, the best-performing n-i-p PSCs to date employ spin-coated SnO_2 particles on top of SnO_x

grown via ALD.[67,68] However, considering scalability and large-scale production, utilization of multiple layers and the spin-coating technique remain unfavorable.

In contrast to the n-i-p PSC structure, the p-i-n structure employs ETLs on top of the perovskites. The choice of deposition parameters becomes significantly more crucial in this case, as perovskites are both reactive and thermally sensitive. Continuous efforts are being made by the research community to deposit ALD-grown ETLs directly on top of the perovskites and to investigate the effects of different ALD precursors and deposition temperatures on the underlying perovskite materials.

Hultqvist and co-authors investigated the deposition of ZnO and SnO_x directly on top of mixed $FAPbI_3$:$MAPbBr_3$ perovskites.[69] The study focused on disentangling the effects of different ALD parameters, such as deposition temperature, vacuum conditions, metal precursors, and the co-reactant H_2O. The crystallinity of the perovskite was found to remain intact in vacuum up to a deposition temperature of 120 °C. Simultaneously, prolonged H_2O co-reactant exposures did not alter the crystallinity of the perovskite. However, the choice of the metal-precursor was found critical for preserving the crystallinity of the underlying perovskite layer. Diethylzinc (DEZn) exposure during the intended ZnO ALD resulted in the decomposition of the underlying $FAPbI_3$:$MAPbBr_3$ perovskite, whereas TDMASn exposure during the ALD of SnO_x kept the absorber bulk intact (although the resulting solar cell performance was still poor). Later studies further explored the direct deposition of SnO_x on mixed halide and mixed A-site-cation perovskite compositions, revealing the formation of performance-limiting interfaces, whereas the bulk of the perovskite was confirmed to remain unharmed.[70,71]

Palmstrom *et al.* studied the growth of SnO_x using TDMASn precursor and H_2O co-reactant on $FA_{0.83}Cs_{0.17}Pb(I_{0.83}Br_{0.17})_3$.[70] They reported that a reaction occurs between TDMASn and the perovskite surface, which results in the removal of FA^+ cations, starting from a deposition temperature of 110 °C. Similarly, Hultqvist *et al.* utilized the triple-cation composition $Cs_{0.05}FA_{0.79}MA_{0.16}PbBr_{0.51}I_{2.49}$ and found the existence of a 2-5 nm thick interfacial layer following the ALD of SnO_x on top of the perovskite.[71] The interfacial layer was found to contain new chemical environments around Pb, N and Br using X-ray photoelectron spectroscopy (XPS), and was deemed unfavorable for the solar cell performance. Overall, the efficiency in these studies was shown to improve significantly following the deposition of a C_{60} or

PCBM electron extraction layer in between the perovskite and SnO_x layers. Despite the enhancement in PCE, utilization of fullerene-based layers is not favorable owing to their poor mechanical stability,[72] and fabrication costs. Besides, the perovskite/C_{60} interface is known to be a major source of non-radiative recombination in p-i-n PSCs.[73]

2.2.2 Hole Transport Layers

ALD has been widely employed for the growth and development of various HTLs, including NiO_x,[49,56,74] vanadium oxide (VO_x),[48,75] cuprous oxide,[76–78] and cobalt oxide.[79,80] Among these HTLs, only NiO_x and VO_x layers have been employed in PSCs, with the former being mainly employed in the p-i-n configuration prior to the deposition of perovskite layers. Here, the ALD of NiO_x was performed using bis(cyclopentadienyl)nickel ($NiCp_2$) or bis(ethylcyclopentadienyl)nickel ($Ni(MeCp)_2$) as the nickel precursors and oxygen plasma as the co-reactant. The resulting films additionally required a post-anneal step at 300-400 °C to obtain efficient PSC performance. The post-anneal step was reported crucial for improving the optical transmittance, perovskite wetting, and charge-carrier mobility, as well as helping in reducing the amount of hydroxyl groups and surface defects [49,56]. The NiO_x/perovskite interface has been identified to be defective in nature, acting as a non-radiative recombination center within the PSC. To minimize the direct contact between the NiO_x and perovskite layers, PTAA[81] and [2-(3,6-dimethoxy-9H-carbazol-9-yl)ethyl]phosphonic Acid (MeO-2PACz)[74] organic HTLs are commonly incorporated between them to improve the PSC performance.

Dutta *et al.* demonstrated the use of NiO_x in a tandem solar cell configuration grown using ALD by employing bis(N,N'-di-tert-butylacetamidinato)nickel ($Ni(^tBu\text{-}MeAMD)_2$) as the Ni-precursor and H_2O as the co-reactant at a deposition temperature of 150 °C.[82] Here, NiO_x was utilized within the PSC structure on top of indium-tin-oxide (ITO) prior to the deposition of [2-(9H-carbazol-9-yl)ethyl]phosphonic acid (2PACz). NiO_x/ITO demonstrated a higher percentage of surface -OH groups than ITO, which, consequently, provided a larger number of anchoring sites for the phosphonic groups present in 2PACz in comparison to ITO. Thereby, NiO_x improved the coverage of SAM and consequently improved the resulting V_{OC} value of the tandem device. Overall, tandem configurations could significantly benefit from the NiO_x-SAM bilayer strategy. NiO_x ALD can allow the formation of conformal layers on top of textured or rough surfaces, which would otherwise be difficult to obtain using other deposition techniques such as spin-coating or sputtering.

2.2.3 Passivation Layers

Passivation layers are commonly employed in PSCs between the perovskite and CTLs to minimize the concentration of deep defects at the interfaces by passivating the dangling bonds. The application of such a layer prior to perovskite deposition can also be beneficial for facilitating the formation of a high-quality absorber. Insulating wide-gap oxide materials, such as Al_2O_3 and SiO_2, are widely adopted for such purposes in the field of PV. Usually, ultra-thin layers are used, which still enable the transport of charge-carriers through the quantum-tunneling effect. In this regard, ALD is uniquely suited for depositing ultra-thin conformal layers, even when the surface roughness is high.

Early works predominantly studied the incorporation of Al_2O_3 via ALD in n-i-p structures on top of $MAPbI_3$ perovskite absorbers.[55,83] Wei *et al.* demonstrated the use of Al_2O_3, using trimethylaluminum (TMA) and H_2O as reactants, in an HTL-free structure by depositing it between $MAPbI_3$ and the Au contact, thereby leading to the formation of a metal-insulator-semiconductor structure.[55] This strategy was demonstrated to improve the photocurrent in the long-wavelength region as a consequence of enhanced charge collection due to the suppression of electron transfer between $MAPbI_3$ and Au. Kim and colleagues further studied the ALD of Al_2O_3 atop $MAPbI_{3-x}Cl_x$.[54] Initially, they investigated the separate effects of H_2O and O_3, that are commonly used as co-reactants alongside an Al precursor for the growth of Al_2O_3. O_3 exposure immediately resulted in a complete decomposition of the perovskite and formation of PbI_2. On the other hand, H_2O exposures also revealed the formation of PbI_2, but in this case the perovskite's crystallinity remained preserved. The utilization of a complete ALD cycle, consisting of TMA and H_2O exposure steps, was found to be even more damaging toward the perovskite. Therefore, a new Al_2O_3 ALD process based on aluminum triisopropoxide (AIP) and acetic acid (AA) precursors was developed, which allowed complete retention of the perovskite crystallinity, without perovskite decomposition into PbI_2. On the contrary, Koushik *et al.* observed successful and even beneficial effects of depositing Al_2O_3 using the TMA/H_2O ALD process on $MAPbI_{3-x}Cl_x$.[84] They reported an increase in the efficiency from 15% to 18% upon depositing 10 cycles of Al_2O_3 between $MAPbI_{3-x}Cl_x$ and the spiro-OMeTAD HTL. In addition, their Al_2O_3-passivated PSC was found to be more stable, preserving 60-70% of its efficiency after 70 days of storage in ambient humidity, considerably more than only 12% efficiency retained by the reference device.

Recently, Artuk *et. al.* reported the use of Al_2O_3 deposited using the TMA/H_2O ALD process to reduce non-radiative recombination at the

perovskite/C_{60} interface, achieving a PCE of 29.9% in a 2T perovskite/silicon tandem structure.[52] This result represented an absolute gain of 1% with respect to the reference device. The improvement in the PCE value was dependent on the stoichiometry of the utilized perovskites, where excess PbI_2 was claimed important for performance enhancement.

The studies report varying observations, indicating the need for more elaborate investigations in which the effect of perovskite composition and stoichiometry, together with the role of the ALD process parameters, including the choice of reactants, and their doses are systematically evaluated. A detailed understanding of the interfaces that form as a consequence of these factors is crucial for achieving further improvements in stability and ensuring reproducibility of PSCs.

3 Scope of the Thesis

This thesis focuses on investigating the ETL stack employed in p-i-n PSCs by studying the material properties of the individual layers, investigating the interfaces between these layers, and corroborating the findings with PSC performance. As discussed in Sections 1.3.3, 2.2.1, and 2.2.3, the ETL stack comprises multiple layers, including C_{60} and SnO_x. Additionally, a passivation layer is often employed between the perovskite and C_{60} layers to achieve the highest PCEs. **Figure 3.1** illustrates the typical PSC structure explored in this thesis and highlights the layers and interfaces investigated herein. The Roman numerals (I, II, III, and IV) indicate the papers in which each layer or interface is studied.

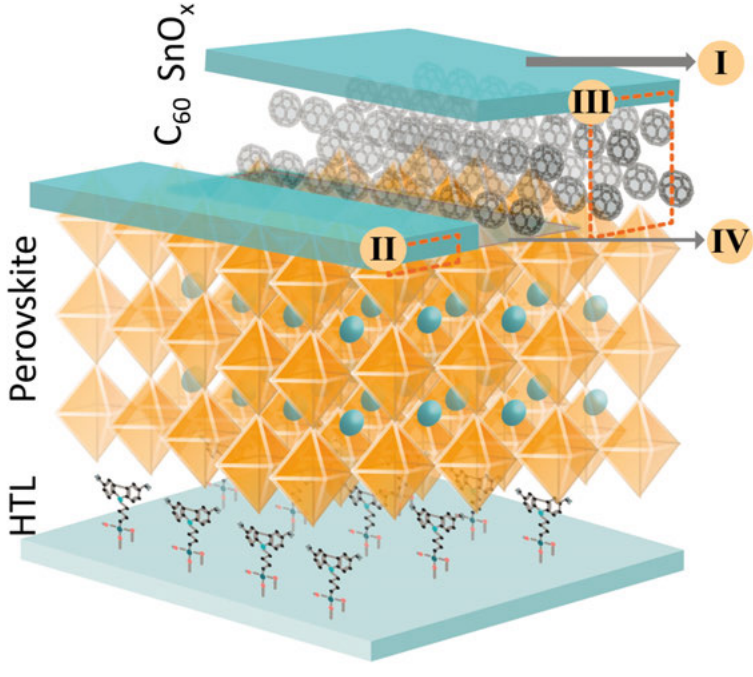

Figure 3.1. Illustration of different sub-projects comprising this thesis. The Roman numerals (I, II, III, and IV) refer to the indices of the papers where the corresponding sub-projects are published/investigated.

In **PAPER I**, the SnO_x ALD process was studied in depth, and **optimized** for its incorporation into PSCs. As discussed in Sections 1.3.3 and 2.2.1, the SnO_x layer grown using ALD is routinely employed in PSCs; however, a clear correlation between ALD process parameters, material properties, and PSC performance has not been fully established. Therefore, I investigated the impact of different ALD process parameters, including the co-reactant choice, co-reactant dose, and deposition temperature on the physical, chemical, optical, and electronic properties of SnO_x. Following this, the SnO_x layers were incorporated into PSCs to study the effects of the number of ALD cycles, co-reactant choice, and co-reactant dose on PSC performance, with the aim of achieving optimum performance and establishing a clear link between material properties of SnO_x and PSC performance.

In **PAPER II**, the efforts were dedicated to **reducing the complexity** of the ETL stack by eliminating the C_{60} layer and performing SnO_x ALD directly on top of different perovskite compositions. Previous studies, discussed in Section 2.2.1, mainly focused on the direct growth of SnO_x by ALD on mixed-A-site-cation (Cs^+, FA^+, and MA^+) and mixed-halide (I^- and Br^-) perovskites, which complicates the analysis and makes it difficult to pinpoint the exact interactions. In this paper, I studied the direct ALD of SnO_x on simple perovskites, including $FAPbI_3$ and $FAPbBr_3$, with the goal of clearly disentangling the role of the different ions present in perovskite toward the formation of the interface with SnO_x.

In **PAPER III**, I studied the ***in situ* growth** of SnO_x on top of perovskite/C_{60} structures using ambient-pressure XPS measurements to investigate whether the C_{60} layer is sufficient to shield the underlying perovskite surface from undesired reactions discussed in PAPER II. Furthermore, in **PAPER III**, the SnO_x ALD was performed on different perovskite/C_{60} structures, including $FAPbI_3/C_{60}$, $FAPbBr_3/C_{60}$, and $(Cs,FA)Pb(I,Br)_3/C_{60}$, to widen the scope of the study, and to understand the role of the perovskite composition in determining the evolution of SnO_x on top of the C_{60} layer.

Finally, in **PAPER IV**, I explored ALD-grown AlO_x as an interfacial layer between the perovskite and C_{60}. As detailed in Section 2.2.3, earlier works mainly investigated the interfacial chemistry between ALD-grown AlO_x and MA-containing perovskites. Since MA-free perovskites are more relevant for commercialization owing to their superior thermal stability, investigating the chemical interactions between ALD-grown AlO_x and $(Cs,FA)Pb(I,Br)_3$ surface is important. Thus, the effect of AlO_x ALD on $(Cs,FA)Pb(I,Br)_3$

perovskite was studied using XPS, and the findings were correlated with the PSC performance. Moreover, AlO_x nanoparticles were also employed instead of ALD-grown AlO_x to separate the impact of the AlO_x ALD precursors from that of the AlO_x material itself.

Overall, this thesis establishes a critical understanding of the ETL stack in p-i-n structures. It explains the impact of the SnO_x ALD process in PSCs, details the properties of the resulting interfaces, and successfully integrates the ALD-grown AlO_x into PSCs. The gathered knowledge is expected to contribute to further improvements in the PSC performance and stability using industry-relevant deposition methods.

4 Experimental Details

4.1 Solar Cell Fabrication

Figure 4.1 presents an overview of the entire process used for the fabrication of p-i-n PSCs investigated in this thesis, with the technical details provided below.

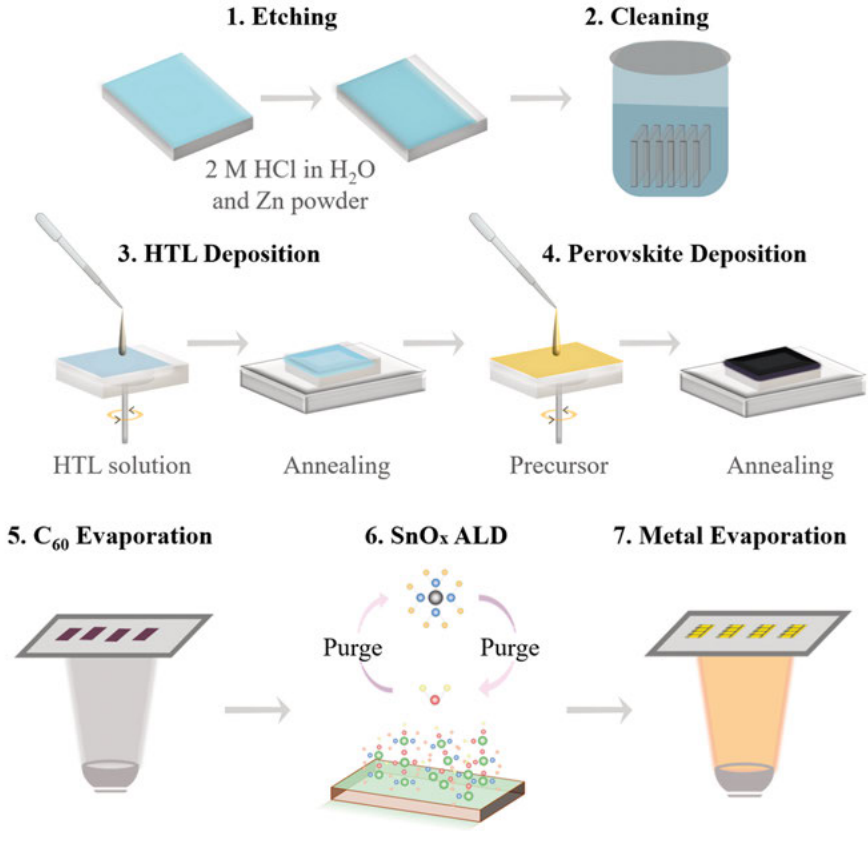

Figure 4.1. Typical sequence of steps involved in the p-i-n PSC fabrication.

4.1.1 Substrate Preparation

ITO or fluorine-doped tin oxide (FTO)-coated SLG substrates with dimensions of 1.4 cm × 2.4 cm were used. Initially, as illustrated in **Figure 4.1,** ~0.3 cm of the ITO/FTO layer was etched from one edge of each substrate using Zn powder and a 2 M HCl solution. The etched substrates were thoroughly cleaned by sequential ultrasonication for 30 minutes each in 1% hellmanex soap solution, deionized water, acetone, and ethanol. The cleaned substrates were then dried using an N_2 gun and treated in a UV-O_3 cleaner for 30 minutes.

4.1.2 HTL Deposition

The substrate preparation was followed by spin-coating of the HTL comprising a [4-(3,6-Dimethyl-9H-carbazol-9-yl)butyl]phosphonic acid (Me-4PACz) molecular layer. The HTL solution was prepared by mixing four parts of 0.4 mg/mL Me-4PACz solution in ethanol and one part of 0.4 mg/mL poly(9,9-bis(3'-(N,N-dimethyl)-N-ethylammoinium-propyl-2,7-fluorene)-alt-2,7-(9,9-dioctylfluorene))dibromide (PFN-Br) solution in methanol. Here, PFN-Br was used to enhance the wettability of the perovskite precursor solution during its spin-coating in the following step.

4.1.3 Perovskite Deposition

All perovskites reported in this thesis were synthesized using either solution-based or evaporation approaches. $FAPbI_3$ and $FAPbBr_3$ were synthesized using spin-coating method as follows:

1. $FAPbI_3$: The synthesis was performed by following the one-step deposition process. First, a 1.8 M $FAPbI_3$ precursor solution containing 829.8 mg of PbI_2, 309.5 mg of FAI, and 42.5 mg of MACl in 0.2 mL dimethyl sulfoxide (DMSO) and 0.8 mL dimethylformamide (DMF) was prepared in a N_2 filled glovebox. After complete dissolution of the salts, the solution was filtered using a 0.45 μm polytetrafluoroethylene (PTFE) filter. The solution was then dynamically spin-coated in air on the substrate at 6000 rpm for 50 s. During the spin-coating, diethyl ether was dispensed during a 15-25 s window from the start of the program. Finally, the deposited films were annealed at 150 °C for 10 minutes and crystalline $FAPbI_3$ films were obtained.
2. $FAPbBr_3$: The perovskite absorber layer was synthesized using the two-step method. In the first step, a 1.1 M $PbBr_2$ solution was prepared by stirring 403 mg of $PbBr_2$ in 0.1 mL DMSO and 0.9 mL DMF

overnight. The solution was subsequently filtered using a 0.45 µm PTFE filter, heated at 70 °C, and then spin-coated at 1500 rpm for 30s and 5000 rpm for 20s. The resulting $PbBr_2$ film was annealed at 70 °C for 1 min. In the second step, a 0.65 mg/mL FABr solution was prepared in methanol at ~1 hour prior to the deposition. The solution was then spin-coated on top of the $PbBr_2$ films at 2000 rpm for 30s. The prepared films were annealed at 150 °C for 25 min to obtain the FAPbBr$_3$ phase. All of the solutions were prepared in an N_2-filled glovebox, and the final annealing step was performed in air under a relative humidity of 30%.

4.1.4 ETL Deposition

After the perovskite deposition, the desired ETL was deposited. In this thesis, various ETLs and their combinations were investigated. Specifically, a single SnO_x layer or bilayers consisting of C_{60}/SnO_x or PCBM/SnO_x were employed. The specific ETL configurations used for each device will be described in the Results and Discussion section. For the deposition of the PCBM layer, a spin-coating process was carried out inside an N_2 filled glovebox. In particular, a 20 mg/mL PCBM solution in chlorobenzene was spin-coated onto the perovskite layer at 2000 rpm for 30 s. On the other hand, the C_{60} layer was thermally evaporated at a deposition rate of ~0.1 Å/s, targeting a thickness of 20 nm.

Atomic Layer Deposition of SnO_x

A microchemistry F120 reactor, illustrated in **Figure 4.2**, was utilized for ALD. As depicted, the system functions as a hot-wall cross-flow reactor with different zones set to temperatures T_1, T_2, T_3, T_4, and T_5, where T_5 is the desired deposition temperature. The setup accommodates two 5 cm × 5 cm substrates in the reaction chamber, and the pressure measured close to the exhaust is normally maintained at ~1 mbar. The precursors are supplied from the inlets at the front side of the system, which are connected to the precursor bottles. All of the unreacted species and reaction products get discarded through the exhaust line connected to an oil pump. For the SnO_x deposition process, TDMASn was employed as the Sn-precursor, deionized H_2O was used as the standard co-reactant, unless otherwise stated, and Ar or N_2 was used as the carrier gas. Experiments were also conducted using an H_2O_2 co-reactant by employing 30% (w/w) H_2O_2 solution in H_2O. The TDMASn bottle was heated to 40 °C using a water bath ~1 hour prior to the deposition, whereas co-reactants were held at room temperature. Normally, the samples mounted in the reactor were heated for 30 mins prior to the execution of the ALD program in order to let the temperatures stabilize. TDMASn precursor line was

additionally supplemented with an Ar or N_2 gas flow to facilitate precursor delivery to the chamber. During the SnO_x deposition, the pressure in the Sn-precursor bottle and the line was kept at ~30 mbar. The dose of precursors was controlled by adjusting the number of turns of the needle valves connected to the precursor bottles.

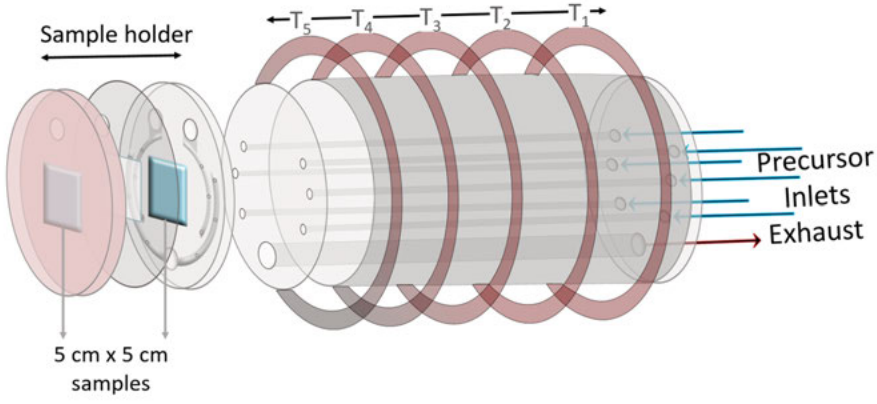

Figure 4.2. Illustration of a quartz block including the sample holder for the F120 ALD reactor.

Mixed $FA_{0.85}Cs_{0.15}PbI_{2.7}Br_{0.3}$ and $FA_{0.93}Cs_{0.07}PbI_3$ perovskite samples and solar cell structures investigated in **PAPER I**, and **PAPER III** were provided by the company First Solar ETC, where perovskite films were deposited using thermal-evaporation.

The samples and solar cell structures studied in **PAPER IV** were provided by Helmholtz-Zentrum Berlin für Materialien und Energie, Berlin (HZB). Here, a $Cs_{0.18}FA_{0.82}PbI_{2.7}Br_{0.3}$ perovskite composition with a band gap of 1.6 eV was synthesized using a solution processing approach.

4.2 Metal-Oxide-Semiconductor Fabrication

These structures were prepared to study the electronic properties of the SnO_x layers. Here, Al, SnO_x, and silicon serve as metal, oxide and semiconductor layers, respectively. N-type (100)-oriented silicon substrates were prepared by first cleaning them using the standard RCA process and then removing the native oxide by briefly dipping them into an HF solution. As-cleaned substrate was promptly loaded into the ALD reactor and SnO_x was grown at 100 °C. Following the ALD of SnO_x, 500 nm-thick Al contact pads of varying diameters were defined by evaporating it through a shadow mask at a deposition rate

of 5-30 Å/s. The top of the sample was then covered by spin-coating a layer of resist 1813 and annealing it at 115 °C for 2 minutes. This was done to allow the removal of any oxide layer from the back side of the sample without affecting the top side. The oxide layer was then etched away from the back side by using an HF dip. Afterwards, a 500 nm thick Al layer was deposited using evaporation at a rate of 5-30 Å/s on the freshly prepared back side of the sample. In the end, the resist coating was removed from the top side by using an acetone bath. The sample was sequentially immersed in the bath for 60 s, 10 s, and 10 s. Finally, the sample was kept in an ethanol bath for 90 s to remove any resist residues.

4.3 Material Characterization

4.3.1 Photoemission Spectroscopy

Photoemission spectroscopy or photo electron spectroscopy (PES) is based on Einstein's theory of the photoelectric effect. As illustrated in **Figure 4.3**, in this technique, X-rays of a suitable energy are impinged on the sample. During photon-material interaction, core-level electrons absorb the photons, and electron ejection events occur. The ejected electrons are collected by the analyzer, and their kinetic energy is determined. The kinetic energy is linked to the binding energy of the electrons, as well as to the incident photon energy by the following relation:

$$BE = h\upsilon - KE - \phi_{spec}$$

Here, KE and BE correspond to the kinetic and binding energies of the electrons, respectively. $h\upsilon$ is the energy of the photons and ϕ_{spec} is the work-function of the spectrometer. **Figure 4.3** demonstrates a typical electronic diagram of a material, where BE_1 and BE_2 represent the binding energy values of core-levels 1 and 2, respectively, and KE_1 and KE_2 correspond to their obtained kinetic energy values, which are measured with respect to the vacuum level of the analyzer ($E_{VAC,spec}$). The binding energy values of the core-levels are always calculated with respect to the Fermi level of the sample and are characteristic of the element.

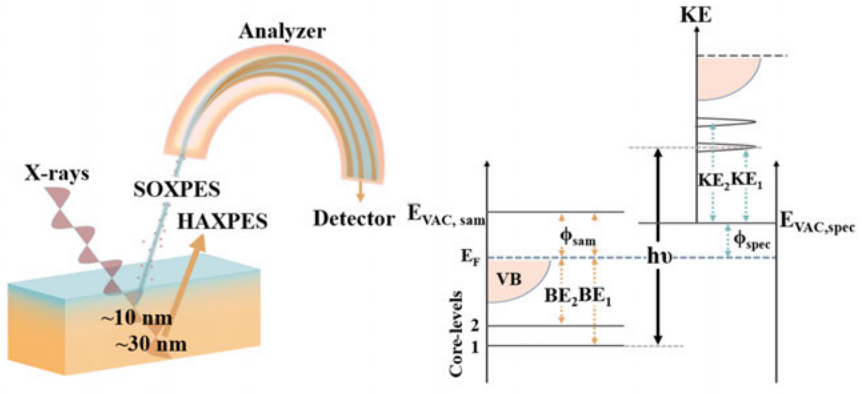

Figure 4.3. Principles of Photoemission Spectroscopy. ϕ_{sam} and ϕ_{spec} are the work functions of the sample and spectrometer. $E_{VAC,sam}$ and $E_{VAC,spec}$ are the vacuum level positions of the sample and spectrometer.

PES methods can be further classified according to the photon energy employed: soft X-ray photoelectron spectroscopy (SOXPES) for 100–1500 eV and hard X-ray photoelectron spectroscopy (HAXPES) for 1500–10000 eV. The probing depth in both PES techniques is dictated by the interplay of binding energy, photon energy and inelastic mean free path ($IMFP$). The probing depth is roughly estimated at $3 \times IMFP$, where $IMFP$ is the average distance that an electron can travel in a material without undergoing an inelastic scattering event. $IMFP$ is dependent on the electron's kinetic energy. Higher photon energies in HAXPES result in the emission of electrons with higher kinetic energies and, consequently, higher $IMFP$ values, leading to a greater probing depth within the material as compared with SOXPES.

In this Ph.D. thesis, different photoemission spectroscopy techniques were utilized to study the interfaces in PSCs, including SOXPES, HAXPES, and ambient-pressure X-ray photoelectron spectroscopy (AP-XPS). SOXPES measurements were performed on a PHI Quantera II scanning XPS microprobe setup comprising a monochromatized Al Kα source (1486.67 eV) having a beam diameter of 100 µm. The spectra were acquired in ultra-high vacuum conditions while maintaining a background pressure of 10^{-9} mbar. Survey spectra were collected using a pass energy of 224 eV and a step size of 0.8 eV, whereas these values were updated to 55 eV and 0.1 eV, respectively, for core-level scans.

AP-XPS measurements were performed in conjunction with the *in situ* ALD of SnO_x on perovskite structures at the SPECIES beamline of the MAX IV synchrotron facility. Details concerning the instrument can be found in Refs.[85,86]

Here, the XPS unit was connected to a flow reactor (ALD cell), where a constant pressure of 0.9 mbar was maintained during the operation using an argon flow of 0.5 sccm. The setup utilized a SPECS Phoibos 150 NAP analyzer and a time-of-flight mass spectrometer (MS) in the differential pump section between the analyzer and the ALD cell to track the ALD process.

AP-XPS measurements were conducted in real time during the ALD growth of SnO_x, using soft X-rays with energies of 850 eV, 400 eV, and 70 eV. To perform real-time measurements, an area ($\sim 1\ mm \times 1\ mm$) defined on the sample was raster-scanned, and core-level signals were recorded in parallel in snapshot mode. The pass energy, step size, and dwell time were set to 100 eV, 0.5 eV, and 0.1 s, respectively. High-resolution (HR) AP-XPS core-level scans were acquired in swept mode before and after the deposition of different number of ALD cycles. For survey scans, a pass energy of 100 eV, step size of 0.5 eV, and dwell time of 0.1 s were used, whereas these values were modified to 50 eV, 0.05 eV, and 0.1 s for the acquisition of the HR core-levels.

XPS core-levels were analyzed and fitted on the Igor Pro software using the XPST (X-ray Photoelectron Spectroscopy Tools) procedure. The background was subtracted with a Shirley function, and peaks were fitted using a pseudo-Voigt function. Photoionization cross-section values were obtained from databases by Yeh and Lindau[87] and Scofield.[88] $IMFP$ Values were calculated using TPP-2M formula[89] on the QUASES-IMFP-TPP2M software.

4.3.2 *In situ* Quartz Crystal Microbalance

Quartz crystal microbalance (QCM) was used to monitor the growth of SnO_x *in situ* during the ALD process. For this purpose, a dedicated ALD sample holder with a slot for the QCM crystal at the center was used. The back side of the crystal was connected to a QCM monitor and a computer. The QCM monitor reads the information on the change in the QCM frequency during the deposition. The data is then converted to mass change per unit area using Sauerbrey's equation, provided below.

$$\frac{\Delta m}{A} = -\frac{\sqrt{\rho_q \mu_q}}{2 f_0^2} \Delta f$$

where Δf and Δm correspond to the frequency change and the mass change values, respectively. The parameters A, ρ_q, μ_q and f_o refer to the active area of the crystal, density of quartz, shear modulus of quartz, and resonant

frequency of the QCM crystal. A typical QCM mass change curve for 20 ALD cycles of SnO_x is shown in **Figure 4.4**. Here, an ALD cycle consists of the sequence of TDMASn exposure: precursor purge: H_2O exposure: co-reactant purge, with their values set to 1s: 1s: 1s: 1s. As demonstrated in the figure, the mass on the QCM increases during the TDMASn exposure owing to the adsorption of precursor molecules on the surface. Whereas, during the H_2O exposure, the mass on the QCM decreases due to a ligand exchange, such that the heavier dimethylamine (DMA, $-N(CH)_3$) ligands are replaced with the lighter -OH groups. The two purging steps do not contribute to any changes in the mass but can be used to track the self-limiting behavior of the ALD process.

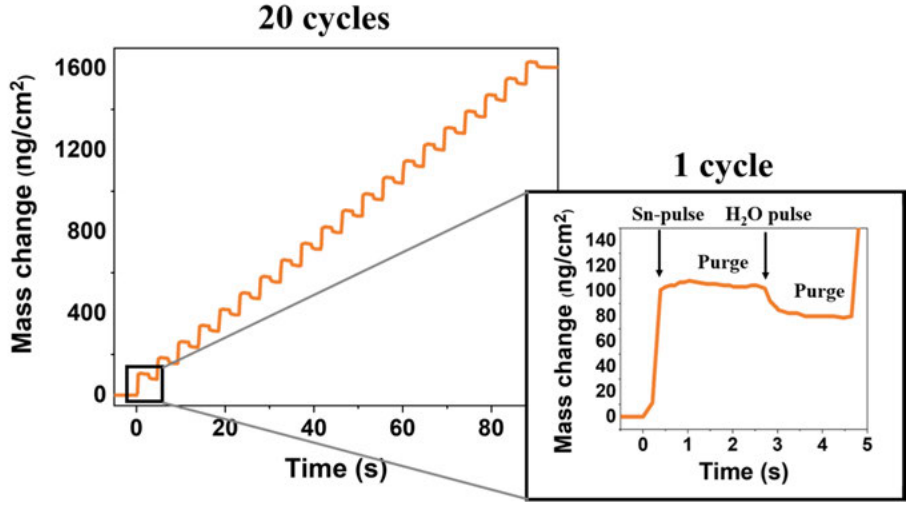

Figure 4.4. Sauerbrey mass change per unit area for 1 s: 1 s: 1s: 1s SnO_x ALD process at 150 °C.

4.3.3 X-ray Diffraction

The method is utilized to determine the crystal structure of a material and to provide information on the lattice parameters and phase compositions of the sample. It is based on the well-known Bragg's law, provided below.

$$n\lambda = 2d \sin\theta$$

where λ is the wavelength of utilized X-rays, n is the order of diffraction, d is the interplanar distance, and 2θ is the angle between the incident and the reflected beams. In this thesis, Malvern Panalytical Empyrean setup was used to investigate the crystal structure of the synthesized perovskite films. The setup employed a monochromatic Cu Kα X-ray source. Additionally, a slit of

size 1/8° was used at the beam entrance to regulate the spot size of the beam, and was followed by the placement of a focusing X-ray mirror on the primary side. A combination of a d-core 0.27° collimator and a PIXcel detector was used on the secondary side. All the measurements were performed in the grazing incidence mode with an incidence angle close to 1°. The combination of slit size and incidence angle resulted in a beam footprint of 10.8 mm on the sample.

Figure 4.5 presents a selected set of X-ray diffraction (XRD) patterns for the perovskite compositions synthesized and studied in this thesis. The obtained XRD patterns and the associated peaks are matched with the literature data[90–93] and pre-existing the databases. Besides the intended perovskite structures, some of the samples demonstrate the existence of a residual PbI_2 peak at 12.8°, matched with the data in the ICDD database (ICDD: 04-014-2519). Peaks from the underlying ITO structure (matched with ICDD: 04-009-7772) were also identified for the $FAPbBr_3$ sample.

Pure $FAPbI_3$ and $FAPbBr_3$ perovskites have a cubic crystal structure (on a macroscopic average scale) with lattice constant values of 6.36 Å[94] and 5.99 Å,[92] respectively. Mixed cation $FA_{0.93}Cs_{0.07}PbI_3$ perovskite shows a similar system as $FAPbI_3$, with the (100) reflection existing at the same 2θ value of 13.9°. The (100) reflection shifts toward higher 2θ values in the case of $FAPbBr_3$ (14.7°) and $FA_{0.85}Cs_{0.15}PbI_{2.7}Br_{0.3}$ (14.06°) due to a smaller size of Br causing lattice contraction.

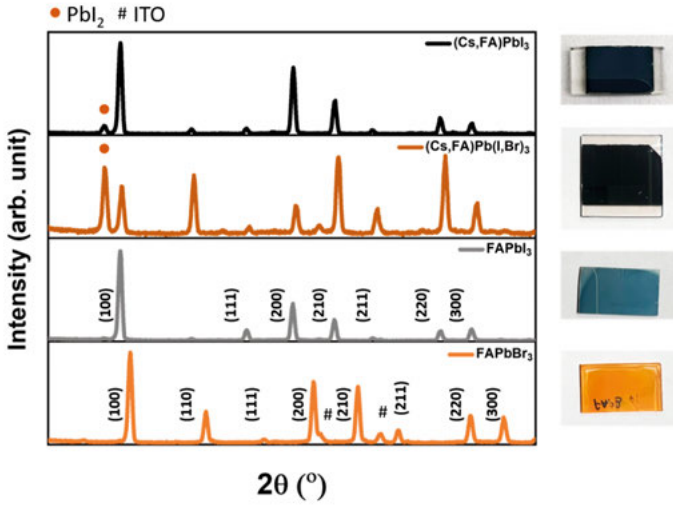

Figure 4.5. Measured X-ray diffraction patterns of $(Cs,FA)PbI_3$, $(Cs,FA)Pb(I,Br)_3$, $FAPbI_3$, and $FAPbBr_3$ (solid lines). The photographs on the right depict the corresponding perovskite films.

4.3.4 X-ray Reflectivity

The method provides information on physical properties such as density, thickness, and roughness of uniform thin-films. At extremely low incidence angles, the X-rays are totally reflected, and once the angle exceeds the critical angle, so-called Kiessig fringes are observed. Kiessig fringes form as a consequence of interference between the X-rays reflected at the top surface and at the film-substrate interface. The critical angle, oscillation frequency, and the slope of the curve are directly linked to the electron density, thickness, and roughness of the film. In this thesis, the MRD II setup was used, which comprised a Cu Kα X-ray source coupled with a beam slit of 1/32° on the primary side and a combination of a 0.09° parallel plate collimator and PW3011 detector on the secondary side. The PANalytical X'Pert Reflectivity software was used to simulate XRR curves and extract the physical parameters. A typical XRR pattern acquired on a SnO_x film is presented in **Figure 4.6**.

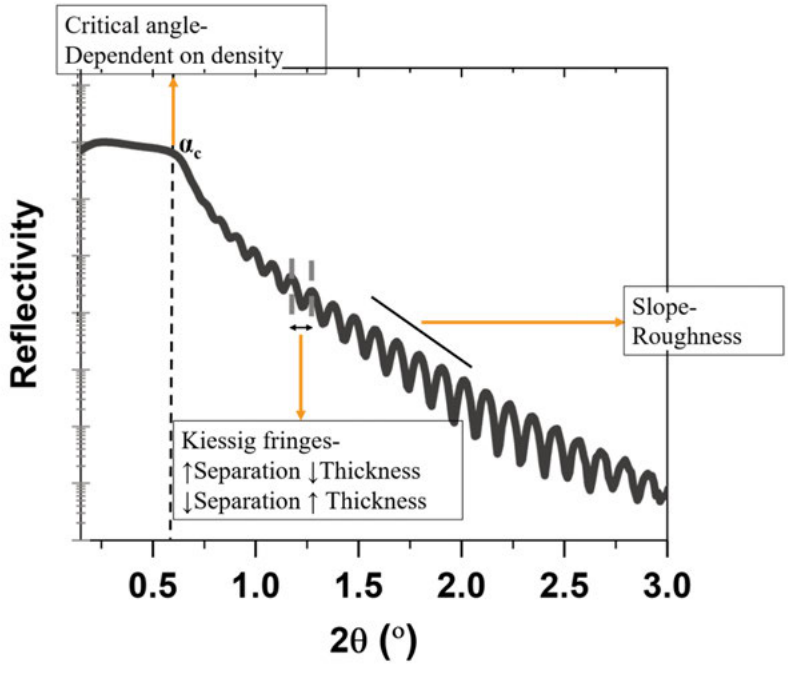

Figure 4.6. XRR pattern of a 76 nm thick SnO_x film grown by ALD at 150 °C on a quartz substrate.

4.3.5 Scanning Electron Microscopy

Scanning electron microscopy (SEM) images were acquired on Zeiss LEO 1550 or 1530 setups using an in-lens detector to check the morphology of the synthesized perovskite films. The micrographs of $(Cs,FA)PbI_3$, $(Cs,FA)Pb(I,Br)_3$, $FAPbI_3$, and $FAPbBr_3$ films are presented in **Figure 4.7**. Besides the exemplified top-view imaging, cross-sectional micrographs were also acquired when relevant. In order to minimize sample charging and degradation under the electron beam, the value of electron high tension (EHT) was kept at 4-5 kV, and a small aperture size of 10 µm diameter was chosen. In addition, aluminum tape was mounted on samples prior to the acquisition of micrographs to further avoid any charging.

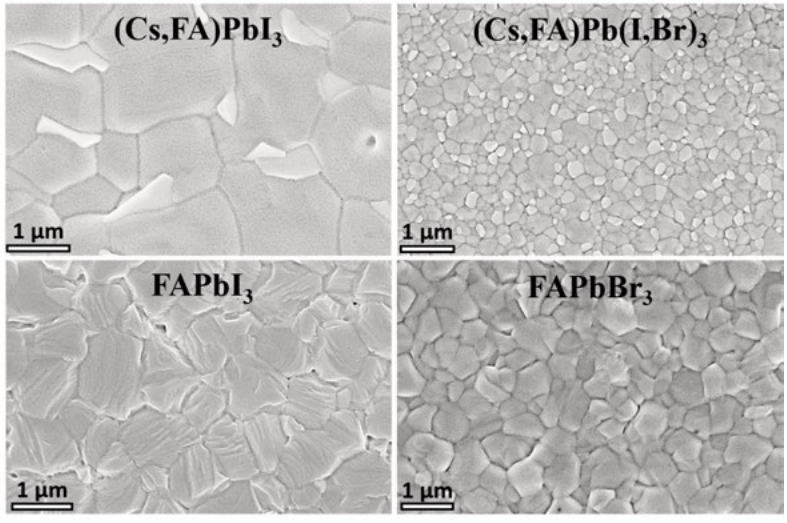

Figure 4.7. SEM micrographs of the typical $(Cs,FA)PbI_3$, $(Cs,FA)Pb(I,Br)_3$, $FAPbI_3$, and $FAPbBr_3$ films.

4.3.6 Optical Measurements

Photoluminescence (PL), optical transmittance (T), and reflectance (R) were routinely measured to confirm the formation of the targeted perovskite compositions with the desired properties. PL spectra were recorded on Cary Eclipse fluorescence spectrophotometer comprising a xenon lamp in conjunction with monochromator on the excitation side and a photomultiplier tube (PMT) detector on the emission side. The spectra were acquired in the wavelength range of 450-900 nm. Both excitation and emission slit widths were set to 5 nm. R and T measurements were conducted using the same PVE300 Bentham system consisting of a dual xenon and halogen light source coupled to a monochromator. R and T data were collected by mounting the sample on the front side (for transmittance) or the back side (for reflectance) of an integrating sphere connected to a Si/InGaAs detector at the bottom. All of the spectra were acquired in the wavelength range of 300-900 nm with a step size of 5 nm.

The obtained results were used to calculate the optical density (log(1/T)) as function of the wavelength. **Figure 4.8** presents the typical optical density and PL spectra of all five perovskite types investigated in this thesis. The estimated bandgap values based on the PL peak position are 1.53 eV for $(Cs,FA)PbI_3$, 1.60 eV for $(Cs,FA)Pb(I,Br)_3$, 1.54 eV for $FAPbI_3$, and 2.31 eV for $FAPbBr_3$. These values are in good agreement with those reported previously in the literature.[90,92,95,96]

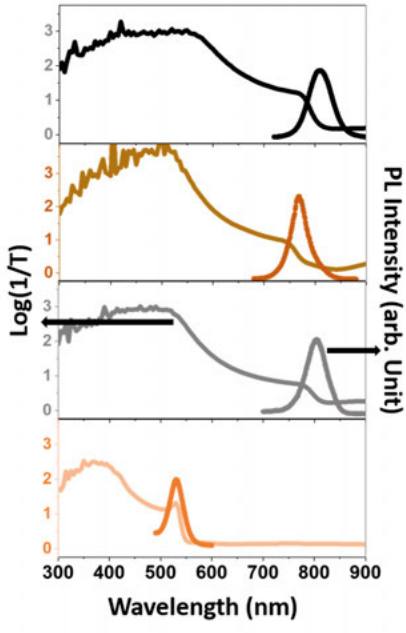

Figure 4.8. Optical density (log (1/T)) and PL spectra for the typical (Cs,FA)PbI_3, (Cs,FA)$Pb(I,Br)_3$, $FAPbI_3$ and $FAPbBr_3$ films on a TCO/HTL stack.

4.4 Device Characterization

4.4.1 J-V Measurements

J-V measurements were routinely conduced on fabricated solar cells to evaluate their performance. All J-V curves were recorded both in reverse and forward directions between -0.2 and 1.5 V. The values of voltage settle time and step size were set to 0.05 s and 0.02 V, respectively. Wave Laboratories SINUS-70 LED-based solar simulator was used to simulate the AM 1.5G spectrum, with an irradiance of 100 mW/cm^2. The illumination area was defined by using a shadow mask with a circular aperture of area 0.0688 cm^2.

The samples supplied by the company First Solar ETC were additionally measured in both reserve and forward directions from 0 to 1.2 V at a scan rate of 200 mV/s using 2450 Keithley source meter. Here, G2V Sunbrick class AAA LED-based solar simulator was used to produce AM 1.5G spectrum, after calibrating it with KG3 filtered silicon cell. The illumination area was set to 0.128 cm^2 by means of a shadow mask.

4.4.2 External Quantum Efficiency

This quantity is a measure of the extent to which a solar cell is capable of spectrally converting an incident photon flux into an external current. The external quantum efficiency (EQE) is given by the following relation.

$$EQE(\lambda) = \frac{\#electrons\ collected}{\#photons\ incident}$$

The short-circuit current density, J_{SC}, can be calculated by integrating the EQE spectra with the photon flux (Φ) using the equation provided below.

$$J_{SC} = q \int EQE(\lambda)\Phi(\lambda)d\lambda$$

The EQE spectra were acquired using a home-built setup comprising a xenon lamp coupled to a monochromator and a filter wheel. Prior to the data acquisition, the instrument was calibrated with a standard silicon cell of known EQE spectrum. The spectra were recorded in the range of 330-900 nm at a step size of 5 nm.

5 Results and Discussion

5.1 Tin oxide Properties and its Optimization for Incorporation in p-i-n PSCs

In **PAPER I**, the focus was placed on the optimization of the SnO_x ALD process. First, the role of co-reactants, H_2O and H_2O_2, in determining the properties of SnO_x at different deposition temperatures was investigated. The SnO_x grown using H_2O as the co-reactant is termed H_2O-SnO_x, while SnO_x grown using H_2O_2 as the co-reactant is referred to as H_2O_2-SnO_x. The physical and chemical properties of SnO_x were studied using QCM, XRR, XPS, resonant inelastic X-ray scattering (RIXS), spectroscopic ellipsometry (SE), and transmittance measurements. Afterwards, the influence of SnO_x layers grown using different process parameters was examined on the PSC performance.

5.1.1 Development of the ALD Process

The growth of SnO_x was studied *in situ* by depositing 40 cycles on a QCM crystal at deposition temperatures of 90 °C and 150 °C. The calculated Sauerbrey mass change values were used to construct saturation curves as a function of precursor pulse lengths and N_2 purge lengths, as shown in **Figure 5.1**. A lower GPC value was observed at 150 °C compared to 90 °C, with H_2O_2-SnO_x exhibiting higher GPC values at both temperatures compared to H_2O-SnO_x. The GPC value saturates shortly after a TDMASn exposure of 0.1 s at both deposition temperatures, whereas a gradual increase in GPC was observed with increasing co-reactant pulse length, particularly at a deposition temperature of 90 °C. Based on the QCM results, pulse lengths of 0.4 s for TDMASn and H_2O/H_2O_2 were deemed optimal, whereas purge times of 0.8 or 1.6 s were selected as the optimal. The SnO_x process with the sequence [TDMASn: purge: H_2O: purge] having values [0.4 s:1.6 s: 0.4 s:1.6 s] resulted in GPC values of 61.1 ± 1.4 ng/cm^2 at 90 °C and 51.2 ± 0.35 ng/cm^2 at 150 °C. When H_2O_2 was employed instead of H_2O, the GPC values increased to 70.8 ± 1.1 ng/cm^2 at 90 °C and 63.6 ± 3.2 ng/cm^2 at 150 °C.

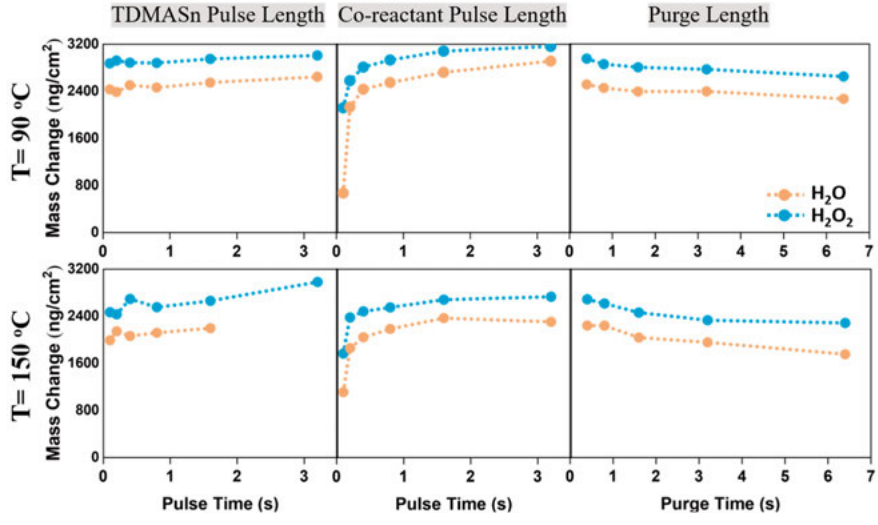

Figure 5.1. Saturation curves constructed using 40 ALD of SnO_x at 90 °C (top) and 150 °C (bottom) as a function of TDMASn and H_2O (orange)/H_2O_2 (blue) co-reactant pulse times and N_2 purge times. Adapted from PAPER I, Supporting Information.

5.1.2 Physical Properties

The optimized ALD recipe for SnO_x was employed to deposit thin-films to study their material properties as a function of deposition temperature. XRR measurements were conducted on SnO_x films (1000 ALD cycles) deposited on quartz substrates at 90 °C, 120 °C, 150 °C, and 180 °C. The density and thickness values from fitting the XRR data are provided in **Figure 5.2(a)**. The film density increased from 4.8 g/cm^3 to 5.7 g/cm^3 for H_2O-SnO_x and from 4.8 g/cm^3 to 5.9 g/cm^3 for H_2O_2-SnO_x as the deposition temperature increased from 90 °C to 180 °C. Simultaneously, the film thickness decreased with increasing deposition temperatures for both co-reactants.

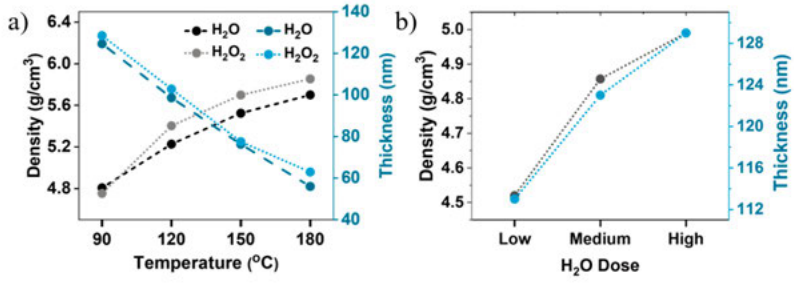

Figure 5.2. XRR density and thickness values obtained for 1000 cycles of SnO_x on quartz substrate grown using (a) H_2O and H_2O_2 at deposition temperatures of 90 °C, 120 °C, 150 °C, and 180 °C and (b) different doses of H_2O at 100 °C. Adapted from PAPER I.

Table 1. GPC values of SnO_x grown using H_2O and H_2O_2 at 90 °C, 120 °C, 150 °C, 180 °C

Deposition Temperature	GPC (Å/cycle)	
	H_2O	H_2O_2
90 °C	1.25	1.29
120 °C	0.99	1.03
150 °C	0.77	0.77
180 °C	0.56	0.63

H_2O_2-SnO_x films exhibited higher densities than H_2O-SnO_x films at all temperatures, except at 90 °C, where the values were comparable. Moreover, H_2O_2-SnO_x films exhibited higher film thicknesses compared to H_2O-SnO_x films. Thus, the XRR-derived thickness values of SnO_x films deposited using the two co-reactants were in good alignment with the GPC values obtained from the QCM measurements.

Since QCM measurements revealed a gradual increase in GPC value with increasing co-reactant dose, the effect of the H_2O dose on the properties of SnO_x was further investigated separately at a deposition temperature of 100 °C. SnO_x thin films were grown using low, medium and high H_2O doses, which corresponded to H_2O evaporations of 0.006 mg/cycle, 0.061 mg/cycle and 0.258 mg/cycle, respectively. The film density and thickness values obtained from XRR analysis are provided in **Figure 5.2(b)**. The film thickness increased with increasing H_2O dose, correlating with the gradual increase observed in mass with H_2O pulse time. Interestingly, the film density is also found to increase from 4.5 g/cm^3 to 5 g/cm^3 upon increasing the H_2O dose from low to high, thus indicating the existence of a correlation between H_2O dose and film properties.

5.1.3 Chemical Properties

XPS O 1s, Sn $3d_{5/2}$, N 1s and C 1s core-level spectra recorded on H_2O-SnO_x and H_2O_2-SnO_x films are provided in **Figure 5.3**. The SnO_x films were deposited on molybdenum-coated SLG to avoid sample charging during the XPS measurements. The O 1s spectra comprised two components, where the lower binding energy (530.99-531.32 eV) and higher binding energy (532.37-532.7 eV) peaks originated from the Sn-O and Sn-OH/carboxyl bonds present in the film.[97–99] The C 1s spectra supported the existence of carboxyl species in all of the films by exhibiting a peak at ~289.5 eV. The Sn-O and S-OH peaks in the O 1s spectra shifted together by 0.15 eV, 0.27 eV, and 0.33 eV toward

lower binding energies for H_2O-SnO_x films, and by 0.16 eV, 0.24 eV, and 0.27 eV toward lower binding energies for H_2O_2-SnO_x upon increasing the deposition temperature from 90 °C to 120 °C, 150 °C, and 180 °C, respectively.

The Sn $3d_{5/2}$ core-level spectra exhibited a single peak at 90 °C; however, an additional peak emerged upon increasing the deposition temperature, becoming particularly evident at 150 °C and 180 °C. The two components demonstrated a separation of 0.6 eV and were attributed to Sn^{4+} and Sn^{2+} states in the SnO_x matrix, as reported previously.[97,98] Similar to the O 1s spectra, the peaks in the Sn $3d_{5/2}$ core-level spectra shifted toward lower binding energies with an increase in the deposition temperature. The peaks shifted by 0.11 eV, 0.20 eV, and 0.22 eV for H_2O-SnO_x, and by 0.11 eV, 0.16 eV, and 0.18 eV for H_2O_2-SnO_x, when the deposition temperate was increased from 90 °C to 120 °C, 150 °C, and 180 °C, respectively. Based on the shifts observed in O 1s and Sn $3d_{5/2}$ core-level spectra, it was concluded that the separation between the Fermi level and the valence band minimum (VBM) decreases with increasing deposition temperature.

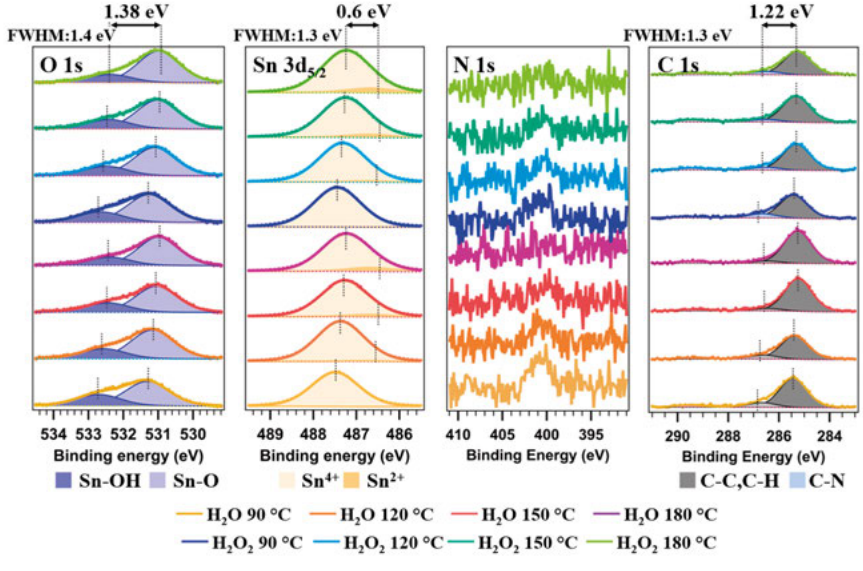

Figure 5.3. XPS O 1s, Sn $3d_{5/2}$, N 1s, and C 1s core-level spectra acquired on SnO_x films grown using H_2O and H_2O_2 at 90 °C, 120 °C, 150 °C, and 180 °C. Adapted from PAPER I, Supporting Information.

The N 1s and C 1s core-level spectra provided insights into the chemistry of the DMA (-$N(CH)_3$) ligand present in the Sn-precursor. The N 1s core-level spectra revealed the presence of nitrogen species linked to DMA in both H_2O-

SnO_x and H_2O_2-SnO_x films, the signal of which decreased with increasing deposition temperature and almost vanished at 180 °C. The C 1s core-level spectra consisted of C-C/C-H and C-N components and also exhibited a minor contribution from carboxyl groups.[100] C-C/C-H peak likely originated from adventitious carbon. The C-N component in the C 1s core-level spectra correlated with the peak in the N 1s spectra and decreased with increasing deposition temperature. Thus, the N 1s and C 1s spectra indicated the presence of ligand impurities, particularly at low temperatures, regardless of the co-reactant used.

Figure 5.4(a) represents the ratio between the integrated areas of the Sn-OH and Sn-O peaks from the O 1s core-level spectra. The results indicated that the concentration of Sn-OH bonds decreases with increasing deposition temperature, with H_2O_2-SnO_x exhibiting a lower concentration of Sn-OH groups than H_2O-SnO_x at all deposition temperatures. The elemental concentration ratios of O/Sn, shown in **Figure 5.4(b)**, were calculated using the total integrated peak areas of the O 1s and Sn $3d_{5/2}$ core-levels. The Scofield photoionization cross-sections[88] of the O 1s and Sn $3d_{5/2}$ core levels, as well as their *IMFP* values, were included in these calculations. The O/Sn ratio decreased from 1.66 to 1.33 for H_2O-SnO_x films, and from 1.52 to 1.35 for H_2O_2-SnO_x films when the temperature was increased from 90 °C to 180 °C. The observed decrease in the two ratios is potentially connected to a reduction in the concentration of hydroxy groups during the H_2O/H_2O_2 exposure with increasing deposition temperature.[101,102]. Simultaneously, the emergence of Sn^{2+} at higher deposition temperatures indicated the existence of SnO within the SnO_x matrix, which would additionally reduce the corresponding O/Sn ratio.

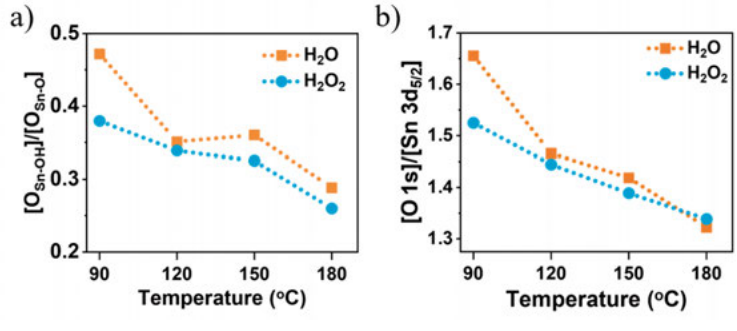

Figure 5.4. Elemental concentration ratio between (a) Sn-OH and Sn-O components and (b) O and Sn. Adapted from PAPER I.

The effect of H_2O dose on the composition of SnO_x films prepared at 100 °C was also investigated. **Figure 5.5** presents the RIXS N K-edge maps acquired from SnO_x films grown using low, medium and high H_2O doses. The method is bulk-sensitive and allows probing of the entire 100-130 nm thickness of the SnO_x films, while simultaneously minimizing the effects of surface contamination. This nitrogen signal can be correlated with the concentration of DMA ligand impurities present in the SnO_x films. The maps indicated a clear decrease in the nitrogen signal with increasing H_2O dose, thereby suggesting that higher H_2O doses enable more efficient removal of ligand impurities.

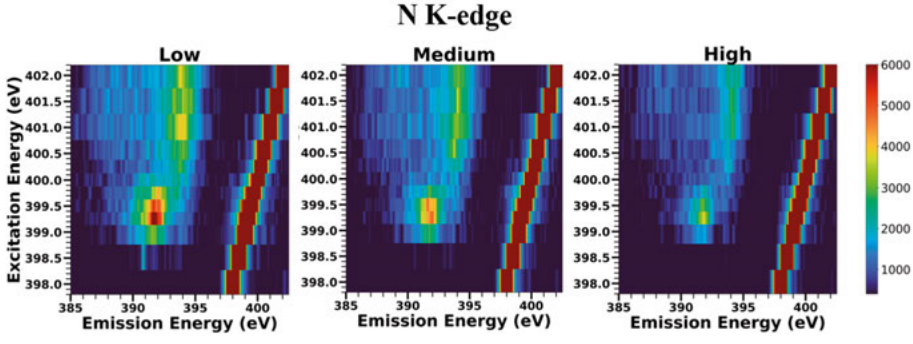

Figure 5.5. RIXS N K-edge maps acquired on SnO_x films grown using low, medium, and high dose of H_2O at 100 °C. Adapted from PAPER I.

Upon combining the results obtained from different characterization methods, it was inferred that higher deposition temperatures allow the formation of denser films with lower concentrations of ligand impurities and Sn-OH species. The reduction in ligand impurities is connected to improved removal of the ligand by-product (H-DMA) at higher deposition temperatures. Besides, the decreased content of hydroxyl groups at higher temperatures reduces the number of reactive surface sites available for the precursor molecule to bind to during its exposure. Consequently, the GPC values were found to decrease with increasing deposition temperature. The higher GPC values and film densities observed for H_2O_2-SnO_x are potentially linked to the formation of a mixture of hydroxyl and oxygen species during H_2O_2 exposure, thereby enabling more efficient ligand removal and generating more surface sites for the Sn-precursor.

5.1.4 Optical Properties

The transmittance spectra of H_2O-SnO_x and H_2O_2-SnO_x films (1000 cycles) grown on quartz substrates at different deposition temperatures are provided in **Figure 5.6**. Additionally, the optical band gap values were obtained using

SE, with the absorption coefficient fitted using the Tauc method. The transmittance of the SnO_x films was found to decrease with increasing deposition temperature. The band gap values decreased significantly when the temperature was increased from 90 °C to 120 °C, whereas they were found to be comparable upon further increasing the temperature from 120 °C to 180 °C. Therefore, the choice of deposition temperature and process parameters influences the optical properties more significantly at low deposition temperatures (90-120 °C).

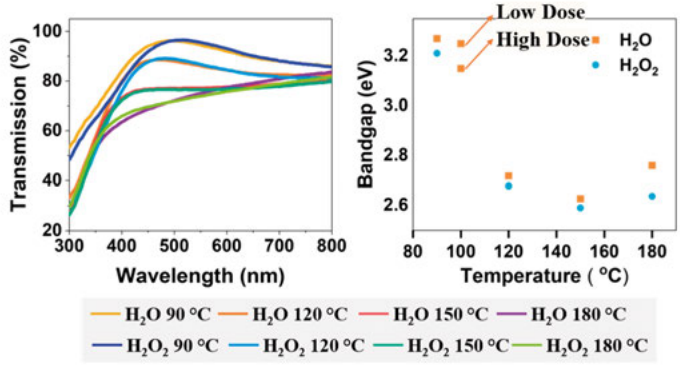

Figure 5.6. Transmittance and optical band gap of SnO_x films grown using H_2O and H_2O_2 at 90 °C, 120 °C, 150 °C, and 180 °C. Adapted from PAPER I, Supporting Information.

5.1.5 Electronic Properties

Si/SnO_x/Al MOS structures were fabricated to understand the influence of the co-reactant choice and dose on the defect density and electron affinity of the SnO_x films. Schottky emission analysis was conducted on SnO_x films grown using low and high doses of H_2O, as well as using a high dose of H_2O_2, as shown in **Figure 5.7(a)**. The extracted electron affinity values are 3.7 eV, 3.8 eV, and 3.9 eV for low H_2O dose-SnO_x, high H_2O dose-SnO_x, and high H_2O_2 dose-SnO_x, respectively. The C-V curves acquired from MOS structures are presented in **Figure 5.7(b)**. The results indicated the presence of a hysteresis in the low H_2O dose-SnO_x sample, which was completely absent in the other two cases. The presence of hysteresis indicated the existence of trapped oxide charges in the low H_2O dose-SnO_x film, with an approximate concentration of 1×10^{11} cm^{-2}.

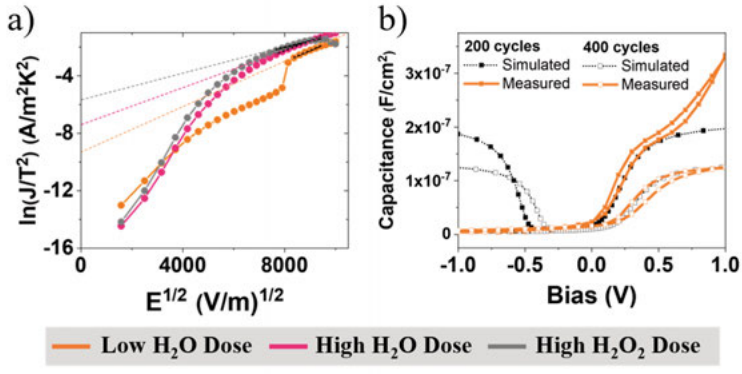

Figure 5.7. (a) Schottky emission characteristics of MOS devices containing SnO_x prepared using low H_2O dose, high H_2O dose and high H_2O_2 dose. (b) Measured and simulated C-V characteristics of MOS structures containing ~20 nm and ~40 nm thick low H_2O dose-SnO_x layers. Adapted from PAPER I.

5.1.6 Solar Cell Performance

In the next step, SnO_x films were incorporated into p-i-n PSC structures with the stack sequence ITO/PTAA/Perovskite/C_{60}/SnO_x/IZO/Ag. In these PSC structures, evaporated (Cs,FA)Pb(I,Br)$_3$ and (Cs,FA)PbI_3 perovskite compositions were utilized. SnO_x was grown on top of the C_{60} layer at a deposition temperature of 100 °C. A low deposition temperature of 100 °C was chosen owing to the higher transparency of SnO_x at this temperature (as discussed in Section 5.1.4), as well as the limited temperature tolerance of the underlying perovskite layer. The effect of the number of ALD cycles, H_2O dose, and co-reactant choice on PSC performance are systematically discussed below.

Effect of ALD Cycles

80, 130, 180, and 230 cycles of SnO_x were incorporated into (Cs,FA)Pb(I,Br)$_3$ PSCs to find the optimal number of cycles for the PSC performance. The measured J-V characteristics of the best-performing cell of each variation are shown in **Figure 5.8(a)**, with the PCE statistics acquired from a total of 16 cells represented as box plots in **Figure 5.8(b)**. Additionally, the parameters extracted from reverse-scanned J-V characteristics are listed in **Table 2** as mean values with their standard deviations. The performance of the best-performing cells was only marginally influenced by the number of ALD cycles, with PSC comprising 80 cycles of SnO_x resulting in the worst performance, primarily due to a low *FF* value. However, the number of ALD cycles demonstrated a stronger impact on performance distribution. As listed in **Table 2**, PSCs incorporating 80 cycles of SnO_x demonstrated lower mean values of

V_{OC}, J_{SC}, and *FF* compared to other PSCs. PSCs incorporating 130 and 180 ALD cycles of SnO_x exhibited similar performance metrics and statistics; however, the mean V_{OC} and *FF* were found to decrease upon further increasing the number of ALD cycles to 230.

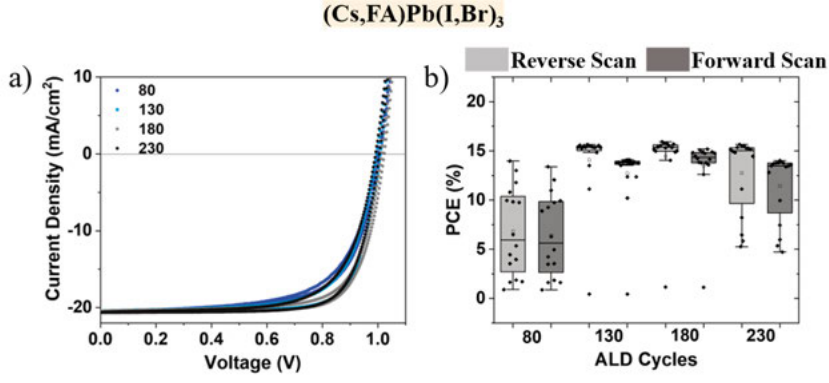

Figure 5.8. (a) J-V characteristics and (b) PCE box plots comparing the influence of ALD cycles on the performance of $(Cs,FA)Pb(I,Br)_3$ PSCs. Adapted from PAPER I, Supporting Information.

Table 2. Performance parameters of $(Cs,FA)Pb(I,Br)_3$ PSCs comprising 80, 130, 150, and 180 cycles of SnO_x.

ALD Cycles	V_{OC} (V)	J_{SC} (mA/cm^2)	*FF*	*PCE*
80	0.72 ± 0.28	20.00 ± 0.50	0.42 ± 0.15	6.81 ± 4.45
130	0.94 ± 0.23	20.40 ± 0.52	0.70 ± 0.13	14.98 ± 1.19
180	0.96 ± 0.19	20.41 ± 0.27	0.71 ± 0.13	15.32 ± 0.48
230	0.92 ± 0.15	20.55 ± 0.14	0.66 ± 0.13	12.75 ± 3.95

80 ALD cycles result in a ~9 nm thick layer of SnO_x (estimated from the GPC value of film-on-film growth), which could be insufficient to protect the underlying layers from sputtering damage during the subsequent deposition of IZO on top of the SnO_x. Consequently, partially damaged perovskite or C_{60} layers could adversely affect the device performance and cause heterogeneities across the surface of the samples. The range between 130 and 180 ALD cycles was considered acceptable for the SnO_x incorporation into PSCs. The reduced *FF* values observed in PSCs containing 230 cycles of SnO_x might be linked to an increased series resistance arising from the increased thickness of the SnO_x layer. Finally, 180 ALD cycles were chosen as optimal, as they

resulted in the best performance, with the lowest standard deviations and hysteresis values among all samples.

Effect of H_2O Dose

Following the thickness optimization, the influence of H_2O dose utilized during the ALD of SnO_x was evaluated on the PSC performance. J-V characteristics and *EQE* spectra of the best-performing cells incorporating low-, medium-, and high H_2O dose-SnO_x are presented in **Figure 5.9(a)** and **(b)**, respectively. The distribution of PCE and hysteresis index (HI) values across 16 cells is shown in **Figure 5.9(c)** and **(d)**. Furthermore, the performance parameters extracted from the reverse-scanned J-V characteristics are provided in **Table 3**. The highest PCE values were obtained for PSCs incorporating high H_2O dose-SnO_x, followed by PSCs utilizing medium H_2O dose-SnO_x, and low H_2O dose-SnO_x. Simultaneously, the HI value was found to decrease systematically with increasing H_2O dose.

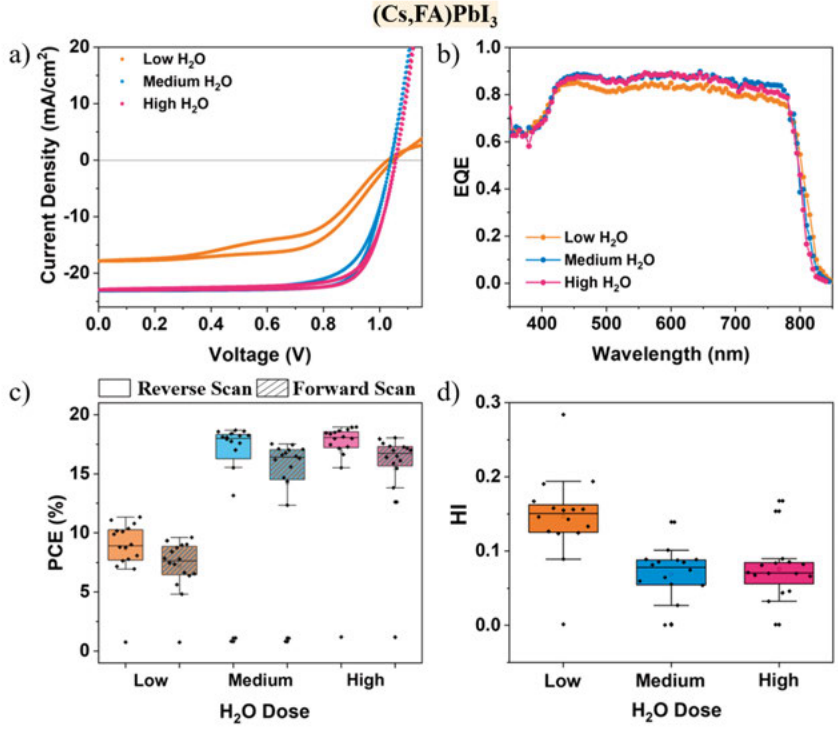

Figure 5.9. (a) J-V characteristics, (b) PCE box plots, (c) EQE spectra, and (d) hysteresis index (HI) comparing $(Cs,FA)PbI_3$ PSCs comprising SnO_x grown using low, medium and high doses of H_2O at 100 °C. Adapted from PAPER I.

Table 3. Performance parameters of $(Cs,FA)PbI_3$ PSCs comprising SnO_x grown using low, medium and high dose of H_2O at 100 °C.

H_2O Dose	V_{OC} (V)	J_{SC} (mA/cm^2)	*FF*	*PCE* (%)
Low	1.01 ± 0.03	18.29 ± 2.52	0.50 ± 0.07	9.14 ± 1.45
Medium	1.03 ± 0.04	22.89 ± 0.19	0.74 ± 0.04	17.56 ± 1.51
High	1.05 ± 0.01	22.78 ± 0.20	0.75 ± 0.04	17.91 ± 0.96

PSCs containing low H_2O dose-SnO_x exhibited s-shaped J-V characteristics, with significantly lower J_{SC} and *FF* values compared to PSCs incorporating medium and high H_2O dose-SnO_x, while the V_{OC} values remained comparable. Such characteristics originate due to the presence of a transport barrier between adjacent layers, i.e., between C_{60} and SnO_x in this case. SnO_x films grown using a low H_2O dose have a lower electron affinity value compared to those grown with high a H_2O dose (shown in Section 5.1.5). Consequently, high H_2O dose-SnO_x might facilitate smoother charge-carrier transport, whereas a barrier might exist at the C_{60}/SnO_x interface when a low H_2O dose is utilized. Furthermore, SnO_x grown using a low H_2O dose exhibited charge traps (discussed in Section 5.1.5), which could potentially trap charge carriers and hinder their transport.

Effect of H_2O_2 Dose

Since the H_2O_2 co-reactant resulted in SnO_x films with higher density and higher electron affinity values compared to H_2O-SnO_x, the next step focused on evaluating the effect of SnO_x films grown using H_2O_2 on the device performance. The J-V characteristics of $(Cs,FA)PbI_3$ and $(Cs,FA)Pb(I,Br)_3$ PSCs incorporating SnO_x grown using different co-reactants and their doses are presented in **Figure 5.10(a)** and **(c)**, with the corresponding boxplots shown in **Figure 5.10(b)** and **(d)**. The incorporation of H_2O_2-SnO_x layers in $(Cs,FA)PbI_3$ PSCs resulted in a decrease in the V_{OC} value compared to PSCs incorporating H_2O-SnO_x layers. However, $(Cs,FA)Pb(I,Br)_3$ PSCs demonstrated comparable PCE values for H_2O_2-SnO_x and H_2O-SnO_x based devices. SnO_x films grown using low doses of each co-reactant resulted in worse performance compared to those grown using high doses of the respective co-reactant.

To further understand the impact of H_2O_2 on the performance of $(Cs,FA)PbI_3$ PSC, a SnO_x layer was grown using a combination of H_2O and H_2O_2, where the first 10 cycles were grown using H_2O and the remaining 170 cycles were

grown using H_2O_2. The V_{OC} value showed a clear improvement upon introducing 10 cycles of H_2O-SnO_x prior to H_2O_2-SnO_x. Based on these findings, it can be hypothesized that H_2O_2 might react adversely with the underlying structure, and consequently cause non-radiative recombination, thereby reducing the V_{OC} value.

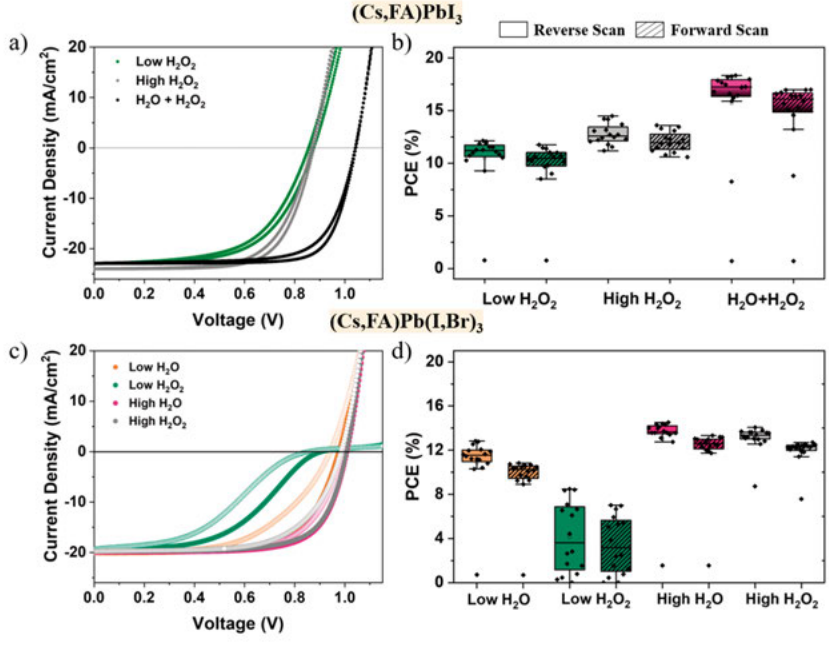

Figure 5.10. (a), (c) J-V characteristics and (b), (d) PCE box plots comparing the effect of H_2O and H_2O_2 co-reactants used during the growth of SnO_x on the performance of $(Cs,FA)Pb(I)_3$ and $(Cs,FA)Pb(I,Br)_3$ PSCs, respectively. Adapted from PAPER I.

5.2 Electron Transport Layer Interfaces in p-i-n PSCs

In **PAPER II** and **PAPER III**, the interfaces that SnO_x forms with the underlying stack within p-i-n PSCs were investigated using XPS methods. In particular, **PAPER II** was focused on studying whether the incorporation of C_{60} layer can be avoided by depositing SnO_x directly on top of perovskites, as the use of C_{60} is non-optimal because of the reasons discussed in Section 2.2.1.

5.2.1 ALD of Tin Oxide on Perovskite

In **PAPER II**, focus was placed on studying the interfaces between SnO_x and simple perovskite compositions comprising one A-site cation, one B-site cation, and one X-site anion, in order to disentangle and isolate the role of different elements present in the perovskite during the interface formation. In this paper, the ALD of SnO_x was performed using the TDMASn precursor and H_2O co-reactant at a deposition temperature of 90 °C directly on top of $FAPbI_3$ and $FAPbBr_3$, and the formed interfaces were studied using XPS.

Effect of X-site Halide

Figure 5.11 compares the XPS Pb $4f_{5/2}$, I $3d_{5/2}$, Br 3d, and Sn $3d_{5/2}$ core-level spectra acquired on $FAPbI_3$, and $FAPbBr_3$ before and after the growth of 1, 2, 5, 10, 20, and 30 cycles of SnO_x. Thus, a total of 7 samples (1 bare perovskite and 6 perovskite/SnO_x) were used for each perovskite composition. The samples were probed using an Al Kα X-ray source, which resulted in a probing depth ($\sim 3 \times IMFP$ through the SnO_x) of 11.6 nm for Pb $4f_{5/2}$, 8.3 nm for I $3d_{5/2}$, 12 nm for Br $3d_{5/2}$, and 9.2 nm for Sn $3d_{5/2}$ core-levels. As the number of ALD cycles deposited on top of the perovskite increased, the signal from SnO_x-related core-levels increased, whereas the signal from the perovskite underlayer decreased.

The Pb $4f_{5/2}$ core-level spectra of $FAPbI_3$ demonstrated the emergence of a new state after the deposition of SnO_x, ~0.6 eV toward higher binding energy with respect to the Pb-I contribution from the $FAPbI_3$ lattice at 143.45 eV. This contribution was linked to PbI_2 formation, as previous studies have reported its existence at a similar binding energy value relative to the main perovskite peak.[103,104] In contrast, the Pb $4f_{5/2}$ spectra of the $FAPbBr_3$ perovskite only demonstrated an attenuation in intensity, without any changes in spectral shape after the SnO_x ALD. Furthermore, no changes were observed in the spectral features of the I $3d_{5/2}$ core-level spectra after the growth of SnO_x on top of the $FAPbI_3$ perovskite. However, a new contribution was found in the Br 3d core-level spectra after SnO_x ALD atop the $FAPbBr_3$ perovskite.

Expectedly, the intensity of the Sn $3d_{5/2}$ core-level spectra was found to increase with the number of ALD cycles for both $FAPbI_3/SnO_x$ and $FAPbBr_3/SnO_x$ stacks. However, the Sn $3d_{5/2}$ core-level spectra of the $FAPbBr_3/SnO_x$ stacks revealed the presence of an additional peak, shifted by 0.57 eV toward the higher binding energy with respect to the main SnO_x peak.

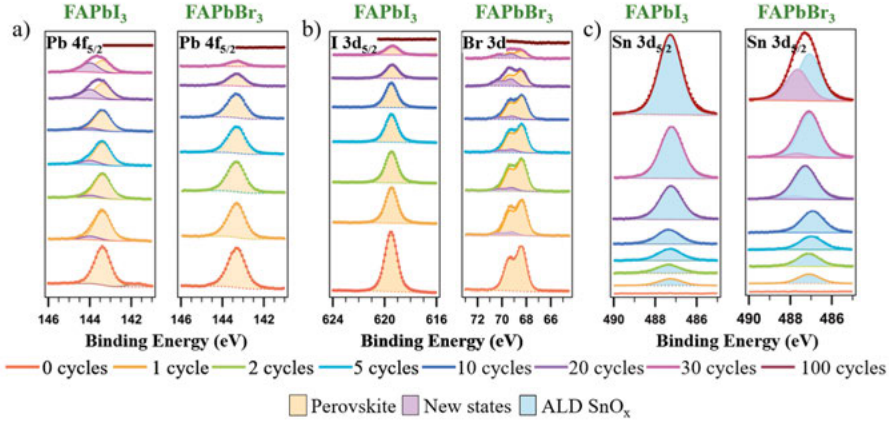

Figure 5.11. XPS (a) Pb $4f_{5/2}$, (b) I $3d_{5/2}$ and Br 3d, and (c) Sn $3d_{5/2}$ core-level spectra obtained on $FAPbI_3$ and $FAPbBr_3$ before and after the ALD of SnO_x using an Al Kα (1486.6 eV) X-ray source. Adapted from PAPER II.

The elemental concentration ratios of I/Pb and Sn/Pb for the $FAPbI_3/SnO_x$ samples, and Br/Pb and Sn/Pb for the $FAPbBr_3/SnO_x$ samples, as a function of ALD cycles, are presented in **Figure 5.12**. All ratios were calculated using the integrated areas of the respective core-level peaks while accounting for the corresponding Scofield photoionization cross-section and $IMFP$ values. The I/Pb ratio had a value of 2.6 prior to the deposition of SnO_x on top of $FAPbI_3$. The ratio decreased to 1.7-1.9 after the growth of 1-10 ALD cycles and dropped below 1 after the growth of 20 or 30 cycles. In the case of $FAPbBr_3$, the Br/Pb ratio had a value of 2.7 before SnO_x deposition, remained between 2.6 and 2.7 after the growth of 1-10 ALD cycles, and became more than 3 after the growth of 20 or 30 ALD cycles. Furthermore, the calculated Sn/Pb ratios were higher for the $FAPbBr_3/SnO_x$ samples than for the $FAPbI_3/SnO_x$ after the growth of 10, 20, or 30 ALD cycles. This indicated greater attenuation of the signal originating from the underlying perovskite layer in the $FAPbBr_3/SnO_x$ samples than in the $FAPbI_3/SnO_x$ samples.

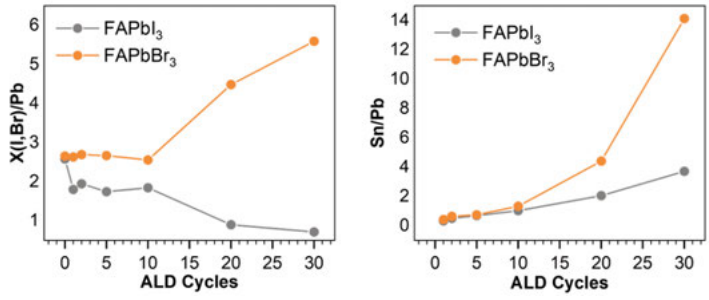

Figure 5.12. Elemental concentration ratios of (a) I/Pb and Br/Pb and (b) Sn/Pb for $FAPbI_3$ and $FAPbBr_3$ before and after the growth of SnO_x. Adapted from PAPER II, Supporting Information.

The influence of SnO_x ALD on $FAPbI_3$ and $FAPbBr_3$ was further evaluated using XRD measurements. XRD patterns acquired from freshly prepared bare perovskite samples and the samples containing 100 ALD cycles of SnO_x on top are presented in **Figure 5.13(a)**, with the regions of interest enlarged in **Figure 5.13(b)-(d)**. Bare perovskite samples exhibited the desired crystal structure, with reflections appearing at the expected 2θ positions, as discussed in Section 4.3.3. The reflections did not exhibit any change in peak width for the perovskite/SnO_x samples, which was found to be ~0.35° in all cases. However, the intensity of the reflections was found to decrease slightly for perovskite samples containing the SnO_x layer on top, possibly due to a minor decrease in the contribution of the underlying perovskite layers to the diffraction volume. A greater reduction in the peak intensity was witnessed for $FAPbBr_3/SnO_x$ compared to $FAPbI_3/SnO_x$. Furthermore, a new peak at ~12.6° emerged in the case of $FAPbI_3/SnO_x$, which was attributed to PbI_2. Overall, the perovskite bulk remained preserved after the growth of SnO_x for both perovskites, with a minor PbI_2 formation observed in the case of $FAPbI_3$.

XRD patterns and photographs of aged samples are provided in **Figure 5.13(e)** and **(f)**, respectively. No significant changes were observed in either the XRD pattern or the appearance of the bare $FAPbI_3$ sample, whereas $FAPbI_3/SnO_x$ exhibited a significantly modified XRD pattern and appearance. The intensity of the main (100) reflection at 13.9° (α-$FAPbI_3$ phase) decreased, and an additional peak at ~11.8° emerged. This new peak was linked to the formation of the δ-$FAPbI_3$ phase,[90,105] which has a wide bandgap and is undesirable for the solar cell performance. On the other hand, the aged $FAPbBr_3$ and $FAPbBr_3/SnO_x$ samples did not demonstrate any changes in their respective XRD patterns compared to the fresh ones.

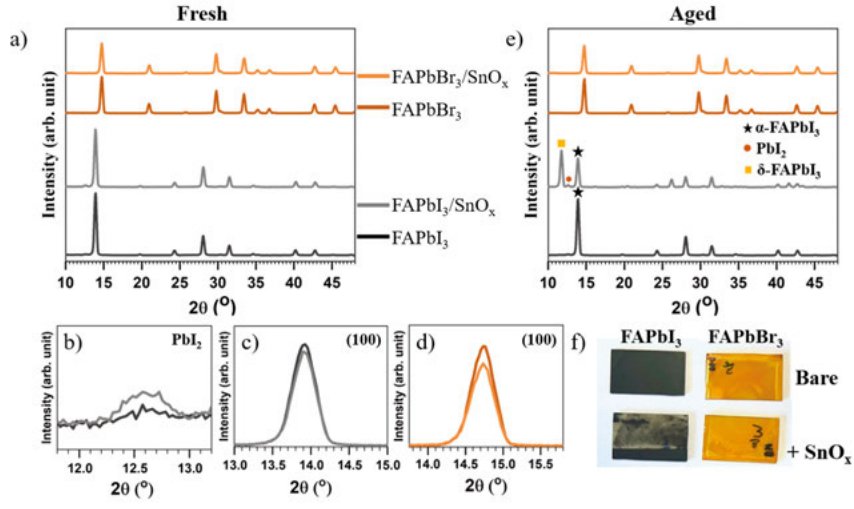

Figure 5.13. XRD pattern obtained on (a)-(d) fresh and (e) aged $FAPbI_3$ and $FAPbBr_3$ samples before and after the growth of 100 cycles of SnO_x. (f) Effect of aging on bare and SnO_x coated $FAPbI_3$ and $FAPbBr_3$ samples. Adapted from PAPER II.

The emergence of an additional peak in the XPS Pb $4f_{5/2}$ spectra, the change in the I/Pb elemental concentration ratio to ~2, and a new XRD reflection at 12.6° confirmed the formation of PbI_2 in the $FAPbI_3/SnO_x$ samples. Besides, α-$FAPbI_3$ was found to partially convert to the unwanted δ-$FAPbI_3$ phase in the $FAPbI_3/SnO_x$ samples as a function of time. This phase conversion was hypothesized to occur as a consequence of increased defects, which have previously been reported to reduce the activation barrier for the transition from the α-$FAPbI_3$ phase to the δ-$FAPbI_3$ phase.[106]

On the contrary, $FAPbBr_3/SnO_x$ demonstrated changes in the Br 3d and Sn 3d core-level spectra, with no differences observed in the Pb $4f_{5/2}$ core-level spectra or the XRD pattern relative to the bare $FAPbBr_3$ sample. The changes observed in the Br 3d and Sn 3d core-level spectra were linked to the formation of Sn-Br bonds. Simultaneously, the increase in the Br/Pb ratio with the number of ALD cycles highlighted the tendency of Br^- ions to migrate into the SnO_x matrix. Moreover, the $FAPbBr_3$ sample exhibited greater attenuation of the XPS Pb $4f_{5/2}$ core-level peak intensity than the $FAPbI_3$ sample after the ALD of SnO_x for the same number of cycles. This might be an effect of the new chemical environment at the $FAPbBr_3/SnO_x$ interface, which could attenuate the signal more strongly than the chemical environment formed at the $FAPbI_3/SnO_x$ interface. Besides, it could also be linked to a greater resulting thickness for the same number of cycles in the case of $FAPbBr_3/SnO_x$.

Effect of A-site Cation

XPS C 1s and N 1s core-level spectra acquired using an Al Kα X-ray source on $FAPbI_3$ and $FAPbBr_3$ before and after the growth of different number of SnO_x ALD cycles are presented in **Figure 5.14**. The C 1s spectra of $FAPbI_3$ and $FAPbBr_3$ exhibited peaks at ~288.3 eV and ~288.0 eV, respectively, corresponding to the carbon environment in FA^+. Simultaneously, both samples showed the presence of adventitious carbon (C-C/C-H) at ~284.8 eV. As the number of ALD cycles increased, the FA^+ peak decreased, and completely disappeared for perovskite samples containing 100 cycles of SnO_x on top. Perovskites containing 100 cycles of SnO_x on top comprised peaks linked to the SnO_x bulk, which included the DMA peak and a minor carboxyl peak, in addition to the adventitious carbon peak (as discussed in Section 5.1.3). C 1s core-level spectra of samples comprising 1, 2, 5, 10, 20, and 30 cycles of SnO_x on top exhibited a combination of peaks from the perovskite and SnO_x bulk, without the existence of any addition contributions.

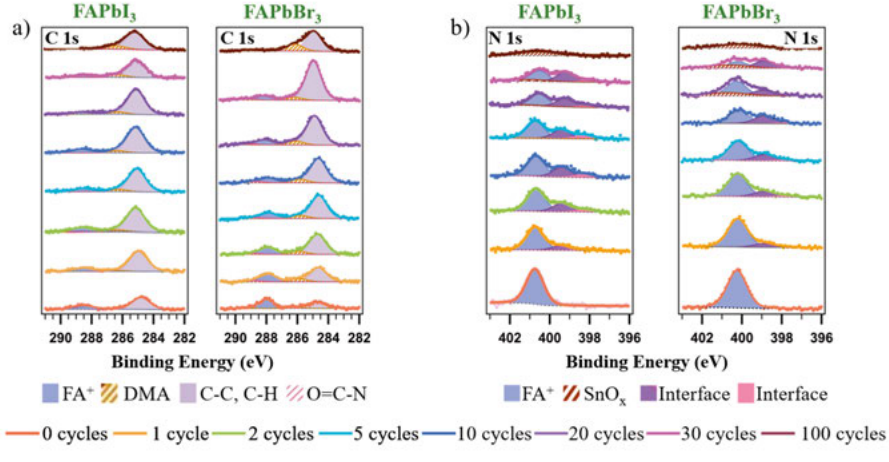

Figure 5.14. XPS (a) C 1s, and (b) N 1s core-level spectra obtained on $FAPbI_3$ and $FAPbBr_3$ before and after the growth of ALD SnO_x using Al Kα (1486.6 eV). Adapted from PAPER II.

The N 1s core-level spectra of FAPbI3 and $FAPbBr_3$ comprised a peak corresponding to the nitrogen present in the FA^+ cation at 400.8 eV and 400.3 eV, respectively. In contrast to the C 1s spectra, the N 1s spectra demonstrated the emergence of two new components shifted by 1.3 eV (indicated in purple) and 2.5 eV (indicated in pink) toward lower binding energy with respect to the main FA^+ peak for samples containing SnO_x on top. The two interfacial contributions were attributed to the deprotonated FA^+ cation and the formation of triazine ring and HCN, based on previous studies.[107,108] In the case of

perovskite samples comprising 100 cycles of SnO_x on top, a broad peak linked to residual DMA impurities in the films was detected, as discussed in Section 5.1.3.

The evolution of the concentration of different components present in the N 1s spectra with the number of ALD cycles is shown in **Figure 5.15**. Here, the peak area of each component was normalized to the total peak area of all components. As the number of ALD cycles increased, the FA^+ contribution decreased, while the additional interfacial components increased. The second interfacial component, linked to the formation of triazine rings and HCN, was found to be lower in the case of $FAPbBr_3/SnO_x$ than in $FAPbI_3/SnO_x$.

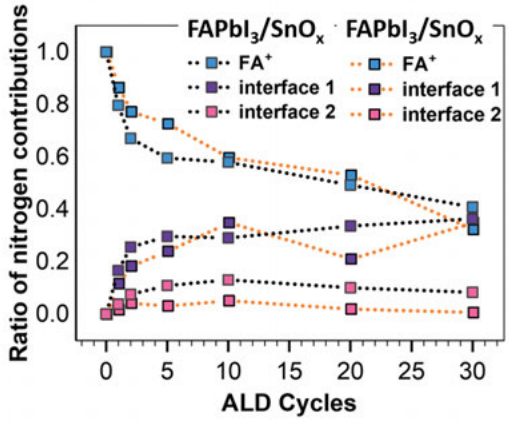

Figure 5.15. Relative ratios of different components present in the N 1s core-level spectra of $FAPbI_3$ (black dashed line) and $FAPbBr_3$ (orange dashed line) as a function of the number of ALD cycles. Adapted from PAPER II, Supporting Information.

5.2.2 ALD of Tin Oxide on Perovskite/C_{60}

In **PAPER III**, *in situ* growth of SnO_x was conducted on $FAPbI_3/C_{60}$, $(Cs,FA)Pb(I,Br)_3/C_{60}$, and $FAPbBr_3/C_{60}$ structures to investigate whether an in between C_{60} layer was sufficient to stop the undesired reactions between the SnO_x and perovskite surface. The conformality of C_{60} on top of different perovskites was evaluated using a combination of SEM and scanning transmission electron microscopy (STEM) imaging, and AP-XPS measurements. Then, the SnO_x ALD was performed at a deposition temperature of 100 °C on different perovskite/C_{60} stacks and the interface was studied using AP-XPS at MAX IV as described in Section 4.3.1.

C_{60} Conformality on Perovskite

The survey spectra of bare $FAPbI_3$, $(Cs,FA)Pb(I,Br)_3$, and $FAPbBr_3$ consisted of core-level peaks originating from all the relevant elements present in the perovskite, as labelled in **Figure 5.16(a)-(c)**. All of the core-level peaks originating from the perovskite disappeared after the deposition of the C_{60} layer on top. The survey spectra of the perovskite/C_{60} stacks showed the C 1s core-level peak linked to the carbon environment in C_{60}, along with an additional Ar 2p core-level peak associated with the argon gas present around the sample. A minor O 1s core-level signal was also identified, possibly associated with a slight surface oxidation.

Furthermore, STEM micrographs were captured on all three structures, i.e., $FAPbI_3/C_{60}$, $(Cs,FA)Pb(I,Br)_3/C_{60}$, and $FAPbBr_3/C_{60s}$, which are provided in **Figure 5.16(d)-(f)**. The STEM samples additionally received 180 cycles of SnO_x and ITO on top, as they would for the complete PSC stack. The estimated thickness of C_{60} was ~22 nm on top of $FAPbI_3$ and $FAPbBr_3$, and ~13 nm on top of $(Cs,FA)Pb(I,Br)_3$. To investigate a larger area of the perovskite/C_{60} structures, a combination of focused ion beam (FIB) and SEM was utilized. Cross-sectional slices having thicknesses of 20-40 nm were prepared from the perovskite/C_{60} structures using FIB, and an SEM micrograph was acquired for each slice. A total of 146 slices were prepared for $FAPbI_3/C_{60}$, 575 slices for $(Cs,FA)Pb(I,Br)_3/C_{60}$, and 321 slices for $FAPbBr_3/C_{60}$ structures. Selected micrographs are presented in **Figure 5.17**, which indicated the presence of defects, particularly at the large surface steps. The total area probed using FIB-SEM measurements and the calculated defect density at the perovskite/C_{60} interfaces are given in **Table 4**. The defect density correlated with the surface roughness of the underlying perovskite layer. Regions with thinner C_{60} coverage, or openings, were formed as a consequence of the directional nature of the C_{60} evaporation process, which fails to cover regions where

shadowing effects occur. No openings were found to exist at the $(Cs,FA)Pb(I,Br)_3/C_{60}$ interface, where the perovskite layer was deposited by evaporation.

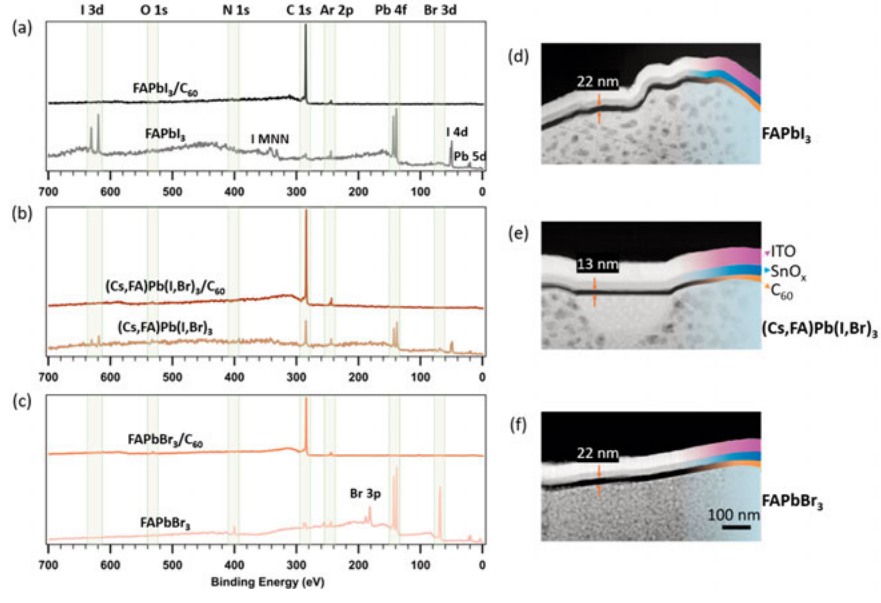

Figure 5.16. AP-XPS survey spectra acquired on (a) $FAPbI_3$ and $FAPbI_3/C_{60}$, (b) $(Cs,FA)Pb(I,Br)_3$ and $(Cs,FA)Pb(I,Br)_3/C_{60}$, and (c) $FAPbBr_3$ and $FAPbBr_3/C_{60}$ using a photon energy of 850 eV at a temperature of 100 °C. STEM micrographs acquired on (a) $FAPbI_3/C_{60}$, (b) $(Cs,FA)Pb(I,Br)_3/C_{60}$, and (c)$FAPbBr_3/C_{60}$ structures, which additionally contain 180 cycles of SnO_x and ITO on top. Adapted from PAPER III.

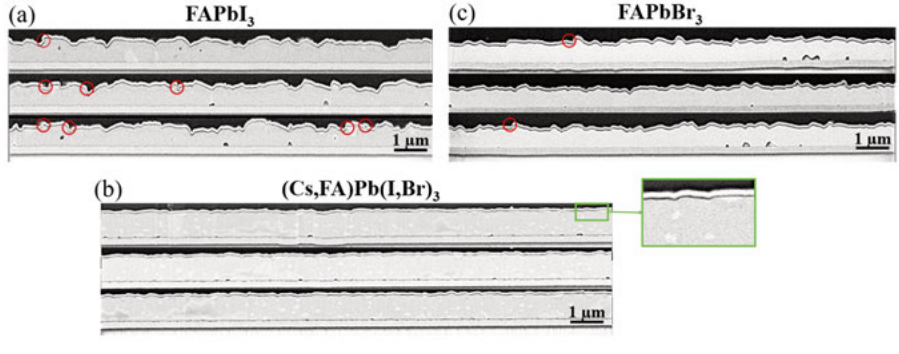

Figure 5.17. Selected SEM micrographs of (a) $FAPbI_3/C_{60}$, (b) $(Cs,FA)Pb(I,Br)_3/C_{60}$, and (c) $FAPbBr_3/C_{60}$ cross-sections prepared using FIB. Structures additionally contain 180 cycles of SnO_x and ITO on top. Red circles highlight the defects present at the perovskite/C_{60} interface. Adapted from PAPER III, Supporting information.

Table 4. Total sample area probed using FIB-SEM and the estimated defect density at the $FAPbI_3/C_{60}$, $(Cs,FA)Pb(I,Br)_3/C_{60}$, and $FAPbBr_3/C_{60}$ interfaces

Structure	Area probed (μm^2)	Defect Density ($\mu m / \mu m^2$)
$FAPbI_3/C_{60}$	38	0.170
$(Cs,FA)Pb(I,Br)_3/C_{60}$	148	N/A
$FAPbBr_3/C_{60}$	175	0.064

Real-Time Cycle-by-Cycle Tracking

During the ALD process of SnO_x, a time-of-flight mass spectrometer (ToF-MS) was used in parallel to track the delivery of the H_2O co-reactant and TDMASn precursor into the ALD cell. The results are provided in **Figure 5.18(a)**. Species with mass-to-charge ratio (m/z) of 21-23 and 36-44 were assigned to argon, 17-19 to H_2O, and 45 or above to HDMA and TDMASn-related products. During the ALD process, the core-level spectra of all the relevant elements (C 1s, Sn 3d, I 3d, Br 3d, and Pb 4f) were acquired at intervals of ~3-4 s to immediately assess the effect of the precursors on the underlying structures. Subsequently, 2D core-level maps were constructed as a function of time during the ALD process, enabling cycle-by-cycle tracking and real-time monitoring of the surface chemistry. The 2D maps acquired on $FAPbI_3/C_{60}$ and $FAPbBr_3/C_{60}$ are presented in **Figure 5.18(b)-(c)** and include Sn 3d and C 1s maps, as well as the corresponding halide maps for each perovskite. The maps were constructed for the first cycle, and subsequent 3, and 5 ALD cycles.

Prior to the Sn-precursor exposure, a clear signal originating from the C_{60} in C 1s map could be observed. As soon as the first TDMASn dose reached the sample, a signal began to emerge in the Sn 3d map. As the number of cycles increased, the Sn 3d signal increased, accompanied by a simultaneous decrease in the C 1s signal. It is also noteworthy that no changes could be observed after the first H_2O exposure in either of the two samples. When comparing the halide 2D-maps, the dynamics differed significantly between the two perovskites during the ALD process. No signal could be detected in the I 3d 2D-map, whereas a signal in the Br 3d 2D-map emerged after the first TDMASn exposure and increased as the number of ALD cycles increased. Thus, the results indicated that the composition of the perovskite plays a critical role in determining ion migration during the SnO_x growth.

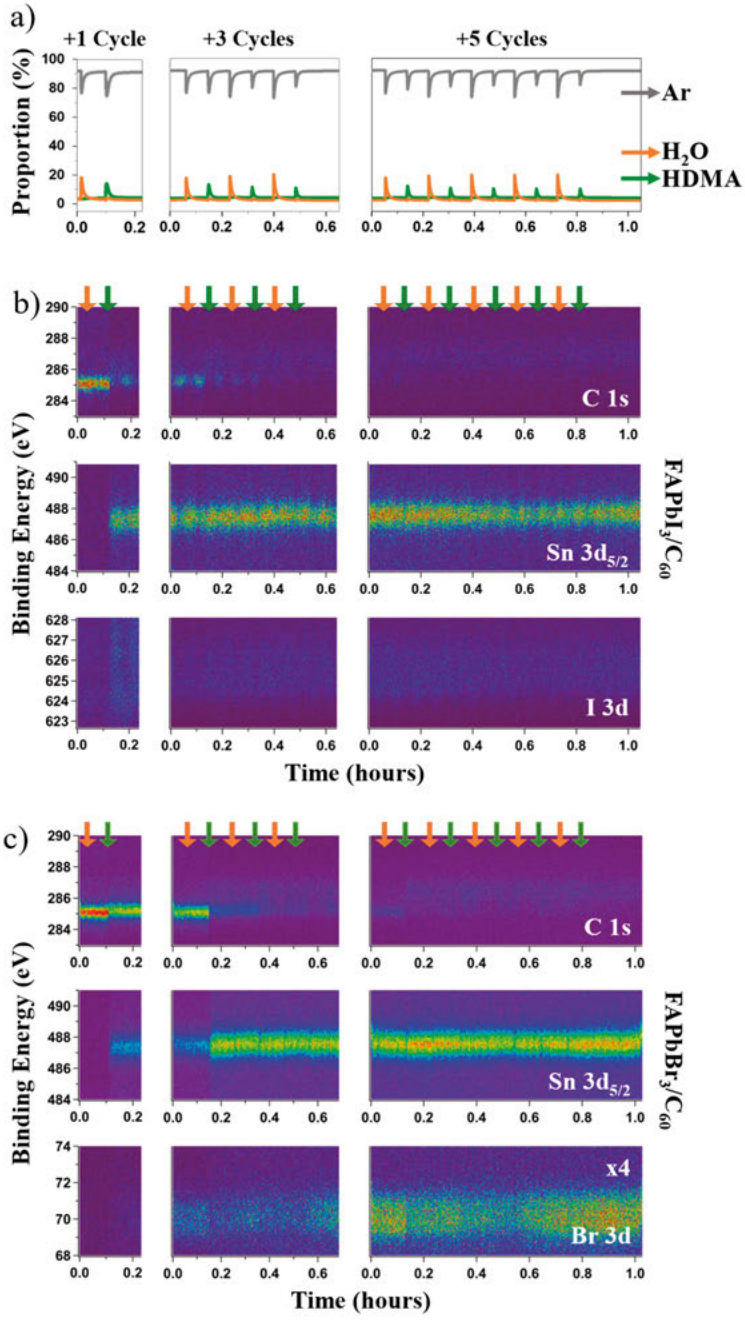

Figure 5.18. (a) Time-of-flight mass spectrometer results demonstrating Ar, H_2O, and HDMA signals obtained during the SnO_x ALD on perovskite/C_{60} structures. (b) 2D-maps of C 1s, Sn $3d_{5/2}$ and I 3d for $FAPbI_3/C_{60}$, and (c) C 1s, Sn $3d_{5/2}$, and Br 3d for (c) $FAPbBr_3/C_{60}$ acquired during the SnO_x ALD. Adapted from PAPER III.

Interface Evolution

HR-AP-XPS spectra of the C 1s, and Sn $3d_{5/2}$ core-levels, shown in **Figure 5.19**, were acquired outside the raster-scanned area after each set of live measurements discussed above. These core-levels were recorded specifically to resolve the fine details of the spectra, which was not possible with the spectra collected in the snapshot mode during the live measurements due to their limited signal-to-noise ratio and resolution. Here, (Cs,FA)$Pb(I,Br)_3/C_{60}$ structure was also analyzed in addition to the $FAPbI_3/C_{60}$ and $FAPbBr_3/C_{60}$ structures. The C 1s core-level spectra of the perovskite/C_{60} structures consisted of the main C_{60} peak at 285.1 eV, linked to the sp^2-hybridized carbon, along with additional shake-up peaks at 289.9 eV and 291.1 eV.[109,110] The two additional peaks observed at 286.9 eV and 288.7 eV were attributed to O-C_{60} contributions.[111]

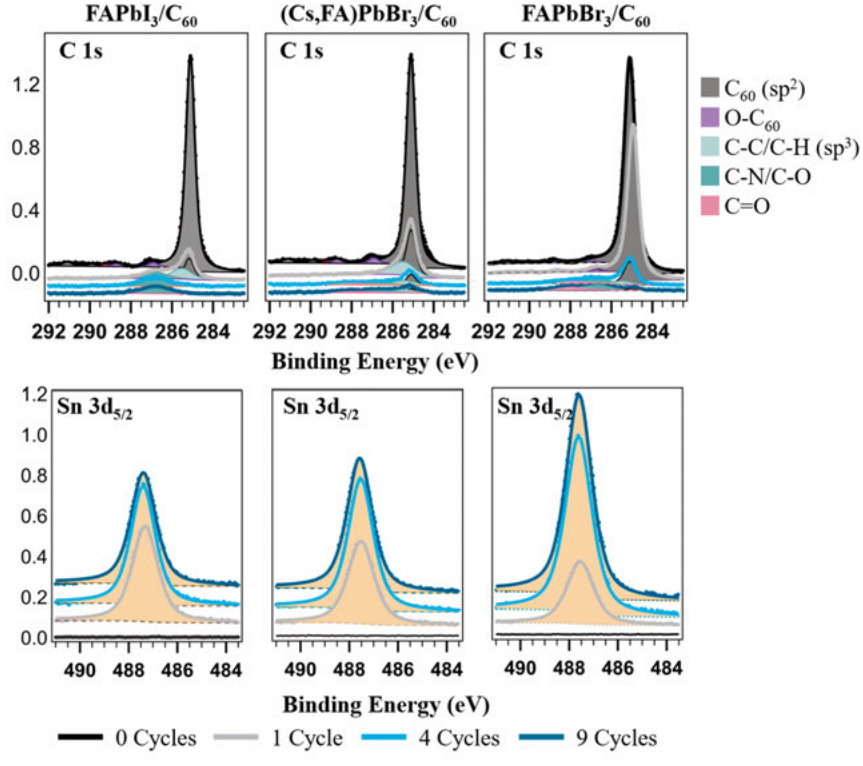

Figure 5.19. The C 1s and Sn $3d_{5/2}$ core-level spectra recorded on $FAPbI_3/C_{60}$, (Cs,FA)$Pb(I,Br)_3/C_{60}$, and $FAPbBr_3/C_{60}$ structures using 850 eV photon energy before and after the growth of 1, 4 and 9 ALD cycles. Adapted from PAPER III.

The intensity of the C_{60} peak and its associated features in the C 1s core-level spectra attenuated significantly after the first ALD cycle in all three structures, with the highest attenuation observed in $FAPbI_3/C_{60}$, followed by $(Cs,FA)Pb(I,Br)_3/C_{60}$ and $FAPbBr_3/C_{60}$. As the number of ALD cycles increased, the components in the C 1s spectra evolved. The intensity of main C_{60} peak decreased, and another peak at 285.46 eV, (shifted by 0.36 eV with respect to the C_{60} peak) linked to sp^3-hybridized carbon, emerged. Further increase in the number of ALD cycles resulted in the emergence of another peak at 286.75 eV (shifted by 1.65 eV with respect to the C_{60} peak). This contribution was assigned to C-N/C-O bonds, which originates from the residual DMA ligands in the film (as discussed in Section 5.1.3).[100] The C_{60} peak could no longer be detected in the $FAPbI_3/C_{60}$ structure after a total of 4 ALD cycles, whereas it remained detectable in the $(Cs,FA)Pb(I,Br)_3/C_{60}$ and $FAPbBr_3/C_{60}$ structures. Finally, the deposition of 9 ALD cycles of SnO_x resulted in only a minor signal from the C_{60} in all of the studied structures, indicating that the SnO_x thickness became comparable to the probing depth of the C 1s core-level through the SnO_x matrix at 850 eV, i.e., ~6.2 nm.

Simultaneously, core-level signals from the underlying perovskites were also investigated, as shown in **Figure 5.20**, to understand the influence of the perovskite elements on interface formation with the C_{60} during the SnO_x growth. Prior to the growth of SnO_x, no major signals could be detected from the underlying perovskite for the perovskite/C_{60} structures. A minor signal was observed in the Pb 4f core-level spectrum of $FAPbI_3/C_{60}$ and the Br 3d core-level spectrum of $FAPbBr_3/C_{60}$. This was likely linked to the presence of defects and thinner C_{60} regions at the $FAPbI_3/C_{60}$ and $FAPbBr_3/C_{60}$ interfaces, which possibly made core-levels with lower binding energies (i.e., ejected electrons with higher kinetic energies) detectable.

After the growth of SnO_x, no signal could be detected in the I 3d and Pb 4f core-level spectra of $FAPbI_3/C_{60}$. The broad feature present in the Pb 4f spectra was attributed to the Sn 4s signal, as its peak falls in the same binding energy region. In contrast, the $(Cs,FA)Pb(I,Br)_3/C_{60}$ and $FAPbBr_3/C_{60}$ structures revealed signals in their respective halide core-level spectra after the ALD of SnO_x, whereas no signals emerged in their Pb 4f core-level spectra. The signal in the I 3d core-level spectra of $(Cs,FA)Pb(I,Br)_3/C_{60}$ increased after the first ALD cycle and saturated soon thereafter. On the other hand, the intensity of the Br 3d core-level peak increased with the number of ALD cycles.

Based on the findings from Section 5.2.1, where the SnO_x ALD was performed directly on top of $FAPbI_3$ and $FAPbBr_3$, it was inferred that Sn-Br bonds might form during the TDMASn exposure. This could be facilitated by a reaction between the perovskite and TDMASn-related products through the defective regions present at $(Cs,FA)Pb(I,Br)_3/C_{60}$ and $FAPbBr_3/C_{60}$ interfaces or through the bulk of C_{60}. Furthermore, the results from the direct deposition of SnO_x on $FAPbI_3$ and $FAPbBr_3$ indicated the likelihood of Br^- migration into the SnO_x matrix, but not I^- migration. This could explain the observed increase in the intensity of the Br 3d peak during the initial stages of SnO_x growth on $(Cs,FA)Pb(I,Br)_3/C_{60}$ and $FAPbBr_3/C_{60}$.

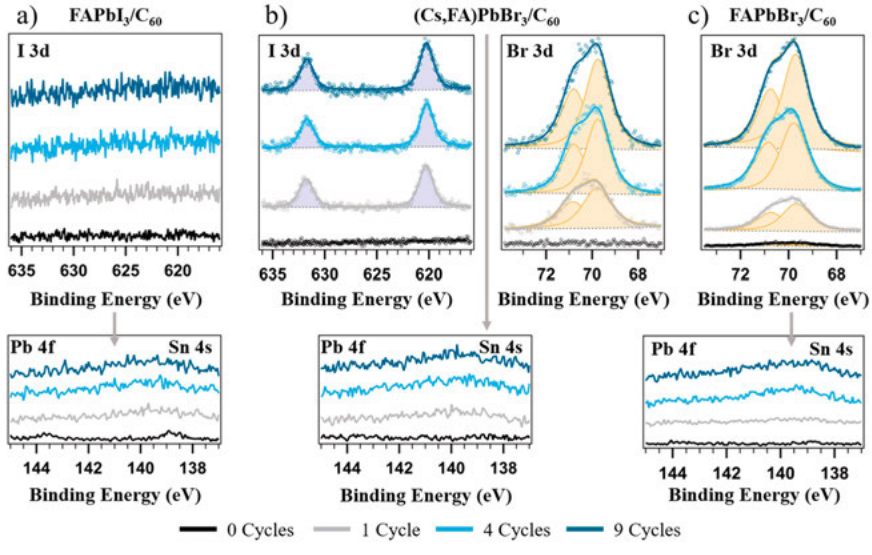

Figure 5.20. (a) I 3d and Pb 4f core-level spectra recorded on $FAPbI_3/C_{60}$, (b) I 3d, Br 3d, and Pb 4f core-level spectra recorded on $(Cs,FA)Pb(I,Br)_3/C_{60}$, and (c) Br 3d and Pb 4f core-level spectra recorded on $FAPbBr_3/C_{60}$ using 850 eV photon energy before and after the growth of 1, 4 and 9 ALD cycles. Adapted from PAPER III.

The elemental concentration ratios of (I, Br)/ Sn, and O/Sn, are shown in **Figure 5.21**. The I/Sn ratio was 0 before and after the growth of SnO_x for $FAPbI_3/C_{60}$ structure, as no I 3d signal was witnessed. In contrast, the I/Sn ratio reached 0.2 after the first ALD cycle and decreased to ~0.12 after a total of 4 and 9 ALD cycles for the $(Cs,FA)Pb(I,Br)_3/C_{60}$ structure. The Br/Sn was found to be ~0.21-0.27 for $(Cs,FA)Pb(I,Br)_3/C_{60}$, and ~0.52-0.60 for $FAPbBr_3/C_{60}$ after the growth of 1, 4, and 9 ALD cycles.

The O/Sn ratio was found to be 2.0-2.2 for $FAPI_3/C_{60}$ following the deposition of 1, 4, and 9 ALD cycles, whereas the value was lower, at ~1.57-1.62, in the

case of (Cs,FA)Pb(I,Br)$_3$/C_{60} and $FAPbBr_3$/C_{60} structures, with the exception of a higher value for $FAPbBr_3$/C_{60} after the first ALD cycle. This higher value observed in the case of $FAPbBr_3$/C_{60} after the first ALD cycle might be connected to a higher oxygen content present on the surface of $FAPbBr_3$/C_{60}. The lower O/Sn ratios observed for (Cs,FA)Pb(I,Br)$_3$/C_{60} and $FAPbBr_3$/C_{60} structures after the ALD of 4, and 9 ALD cycles might be linked to the halide migration dynamics observed in these structures. The formation of Sn-Br bonds could limit the available sites for ligand exchange during the H_2O co-reactant exposure, thereby hindering the growth of SnO_x and influencing its stoichiometry.

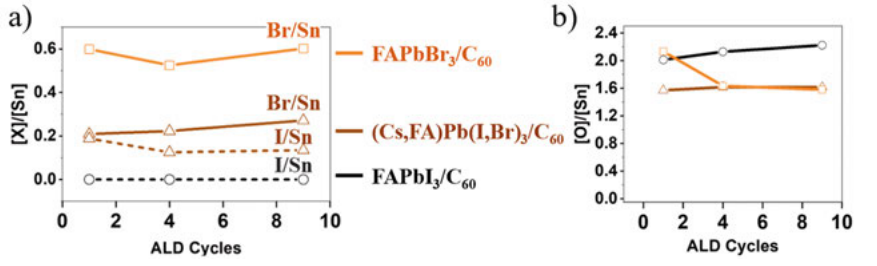

Figure 5.21. Elemental concentration ratio of (a) halide (X)/Sn, and (b) O/Sn calculated using the integrated areas of I 3d, Br 3d, Sn 3d and O 1s core-level peaks measured on $FAPbI_3$/C_{60}, (Cs,FA)Pb(I,Br)$_3$/C_{60}, $FAPbBr_3$/C_{60} using 850 eV photon energy before and after the growth of 1, 4 and 9 ALD cycles. Adapted from PAPER III.

2D Perovskite Incorporation

As discussed in Section 1.3.5, the use of a 2D perovskite on top of a 3D bulk perovskite offers a promising strategy for mitigating ion migration in PSCs. Phenethylammonium bromide (PEABr) was deposited on top of the $FAPbBr_3$ perovskite to facilitate the formation of the 2D-$(PEA)_2PbBr_4$ perovskite[112] and to investigate its impact on the bromine migration discussed above. The Sn $3d_{5/2}$, C 1s, and Br 3d core-level spectra acquired for the $FAPbBr_3$/C_{60}, and $FAPbBr_3$/$(PEA)_2PbBr_4$/C_{60} structures before and after the growth of 1 and 4 ALD cycles of SnO_x are provided in **Figure 5.22**. The Sn $3d_{5/2}$, and Br 3d core-level spectra are scaled by a factor of 10 for better visibility.

Prior to the SnO_x ALD, only the C_{60} peak was observed in the C 1s spectra. After the first ALD cycle, clear signals emerged in the Sn $3d_{5/2}$ and Br 3d core-level spectra in line with the above-mentioned observations. The Sn $3d_{5/2}$ core-level signal increased and the C 1s core-level signal attenuated more strongly for the $FAPbBr_3$/$(PEA)_2PbBr_4$/C_{60} structure than for $FAPbBr_3$/C_{60}, while the Br 3d core-level signals remained comparable. Finally, after a total of 4 ALD

cycles, the Sn $3d_{5/2}$ and C 1s core-level signals became comparable for the $FAPbBr_3/C_{60}$, and $FAPbBr_3/(PEA)_2PbBr_4/C_{60}$ structures, as the SnO_x thickness likely approaches the probing depth. However, the corresponding Br 3d core-level signal was lower for the $FAPbBr_3/(PEA)_2PbBr_4/C_{60}$ structure.

The $FAPbBr_3/C_{60}$ structure exhibited a Br/Sn elemental concentration ratio of 0.60-0.52, which decreased significantly to 0.37-0.35 upon the incorporation of the 2D-$(PEA)_2PbBr_4$ perovskite between $FAPbBr_3$ and C_{60}, thereby indicating successful mitigation of bromine migration during the ALD of SnO_x. The incorporation of such a treatment could offer a potential solution to improving the performance and stability of wide-band gap p-i-n PSCs that employ Br-rich perovskite absorbers and require ALD-grown SnO_x.

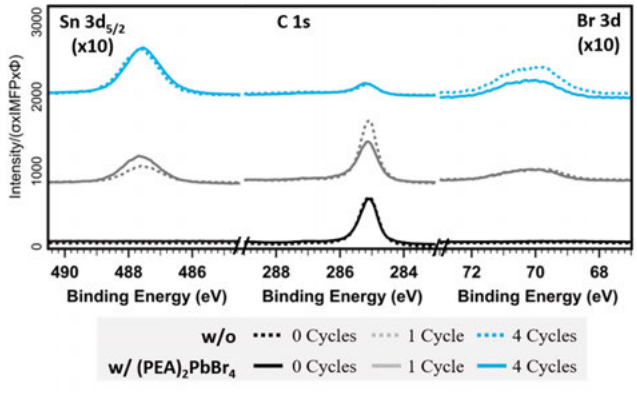

Figure 5.22. Sn $3d_{5/2}$, C 1s, and Br 3d core-level spectra recorded on $FAPbBr_3/C_{60}$, and $FAPbBr_3/(PEA)_2PbBr_4/C_{60}$ using 850 eV photon energy before and after the growth of 1, and 4 ALD cycles. Adapted from PAPER III.

5.3 Passivation Layer by ALD in p-i-n PSCs

As discussed in Section 2.2.3, ALD has been widely utilized for the growth of passivation layers, particularly AlO_x, in PSCs. Most of these studies were focused on studying the chemical interaction between ALD-grown AlO_x and MA-perovskites. Therefore, in **PAPER IV**, the interfacial chemistry between MA-free, $Cs_{0.18}FA_{0.82}PbI_{2.7}Br_{0.3}$ perovskite and AlO_x grown by ALD (ALD AlO_x) was investigated using XPS. Simultaneously, the influence of ALD AlO_x on the performance of p-i-n PSCs was evaluated and correlated to the interfacial chemistry. In parallel, AlO_x nanoparticle (NP) treatment was also employed instead of ALD AlO_x treatment to clearly distinguish the effect of ALD precursors from that of the AlO_x material itself on the PSC performance.

5.3.1 Interfacial Chemistry

The samples were surface treated using a combination of propane-1,3-diammonium iodide ($PDAI_2$) and the two types of AlO_x mentioned above. XPS Cs $3d_{5/2}$, I $3d_{5/2}$, Pb 4f, Br 3d, N 1s, C 1s, Al 2p, and O 1s core-level spectra recorded using an Al Kα X-ray source on bare and surface-treated perovskite samples are provided in **Figure 5.23**. The presence of AlO_x on the perovskite surface was confirmed using their respective Al 2p, and O 1s core-level peaks. O 1s core-level spectra of AlO_x-treated perovskite exhibited two peaks linked to Al-O and Al-OH contributions, as previously reported.[113] The Al 2p and Cs 4d core-level peaks have similar binding energies, which resulted in the emergence of a convoluted signal in the Al 2p core-level scan. The Al 2p contribution was deconvoluted by using the fitting parameters for Cs 4d obtained from the bare sample, with the remaining contribution assigned to the Al 2p peak.

The Cs $3d_{5/2}$, I $3d_{5/2}$, and Pb 4f core-level spectra of $PDAI_2$+ALD AlO_x-, and $PDAI_2$+AlO_x NP-treated samples demonstrated spectral features and peak widths similar to those of the bare perovskite. In contrast, the Br 3d and N 1s core-level spectra of the $PDAI_2$+ALD AlO_x-treated perovskite comprised additional peaks compared to the bare and $PDAI_2$+AlO_x NP-treated perovskite samples. Notably, the $PDAI_2$+AlO_x NP-treated perovskite sample did not show variation in its Br 3d and N 1s core-level spectra compared to the bare perovskite. The Br 3d core-level spectrum of the perovskite/$PDAI_2$+ALD AlO_x exhibited an additional peak at a binding energy 0.55 eV higher than that of the main Pb-Br peak originating from the perovskite lattice. Additionally, two new peaks were found to emerge in the N 1s core-level spectrum of the perovskite/$PDAI_2$+ALD AlO_x sample, which were shifted by 1.55 eV and 1.33 eV toward higher and lower binding energies, respectively, relative to the main

FA^+ peak. The former contribution was attributed to protonated nitrogen species, whereas the latter was assigned to the deprotonation of the FA^+ cation.[114,115]

The C 1s core-level spectra exhibited an FA^+ peak at 288.15 eV, 288.25 eV, and 288.33 eV in the case of bare, $PDAI_2$+ALD AlO_x-treated, and $PDAI_2$+AlO_x-treated perovskite samples, respectively. All of the samples additionally exhibited an adventitious carbon (C-C/C-H) peak in the C 1s spectra. The C-C/C-H peak exhibited a higher intensity for the perovskite/$PDAI_2$+ALD AlO_x sample than for the other two samples, possibly due to residual ligand species ($-CH_3$) remaining at the surface. Furthermore, the C 1s core-level spectrum of the perovskite/$PDAI_2$+ALD AlO_x comprised an additional peak at 286.7 eV, which is commonly associated with C-N/C-O bonds.[100]

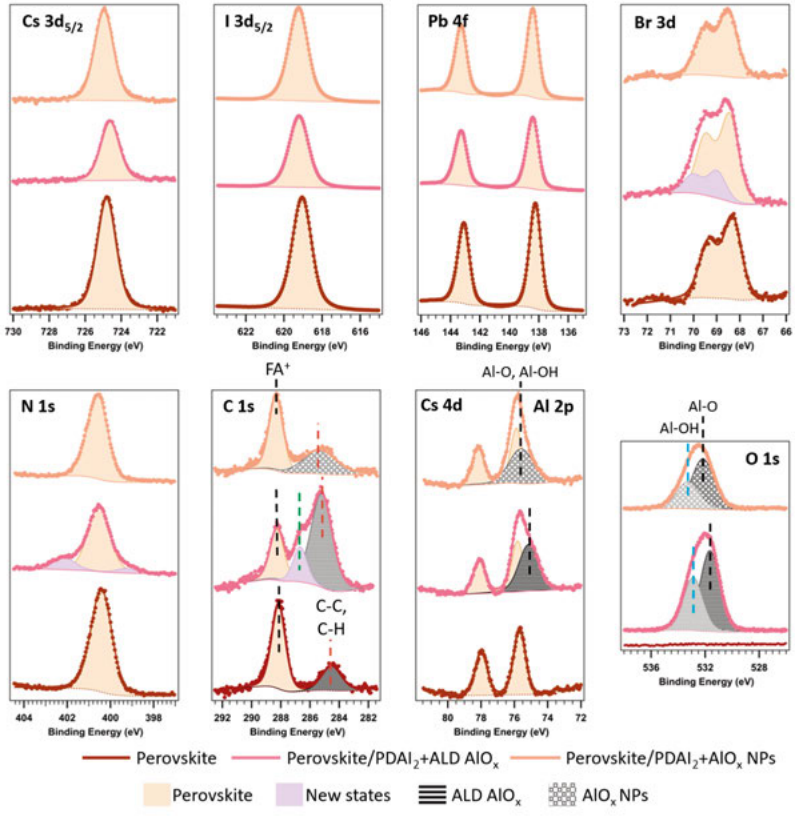

Figure 5.23. XPS Cs $3d_{5/2}$, I $3d_{5/2}$, Pb 4f, Br 3d, N 1s, C 1s, Al 2p, and O 1s core-level spectra recorded using Al Kα X-ray source for perovskite, perovskite/$PDAI_2$+ALD AlO_x, and perovskite/$PDAI_2$+AlO_x NP samples.

The elemental concentration ratios of I/Pb, Br/Pb, Cs/Pb, N/Pb, and O/Al for bare, $PDAI_2$+ALD AlO_x-treated, $PDAI_2$+AlO_x NP-treated perovskite samples are provided in **Figure 5.24(a)**. The bare and $PDAI_2$+AlO_x NP-treated perovskite samples demonstrated similar elemental concentration ratios, whereas the $PDAI_2$+ALD AlO_x-treated perovskite sample exhibited somewhat different ratios, where the I/Pb, and Cs/Pb ratios decreased and the N/Pb and Br/Pb ratios increased. Furthermore, the elemental concentrations of the Pb $4f_{7/2}$, Cs $3d_{5/2}$, I $3d_{5/2}$, N 1s, and Br $3d_{5/2}$ core-level peaks for all three samples, normalized with respect to those of the bare perovskite sample, are presented in **Figure 5.24(b)**. All core-level peaks originating from the underlying perovskite witnessed an attenuation of ~25% upon the application of the $PDAI_2$+AlO_x NP treatment on top. In contrast, different core-level peaks exhibited varying degrees of attenuation or enhancement in their respective intensities in the case of $PDAI_2$+ALD AlO_x treatment. The intensity of the Br $3d_{5/2}$ core-level peak increased, whereas the intensities of the Pb $4f_{7/2}$, I $3d_{5/2}$, Cs $3d_{5/2}$, N 1s core-level peaks attenuated by different amounts.

Overall, the changes observed in the Br 3d, N 1s, and C 1s core-level spectra, as well as in the elemental concentrations of the $PDAI_2$+ALD AlO_x-treated perovskite sample were attributed to a chemical reaction between the perovskite surface and the TMA precursor. Based on these findings, the reactions illustrated in **Figure 5.24(c)** were proposed. The TMA precursor was linked to cause the deprotonation of FA^+ upon interacting with the perovskite surface, while simultaneously resulting in the elimination of CH_4 by-products. The changes in bromine environment and its accumulation close to the surface was explained by the likelihood of Al-Br bond formation.

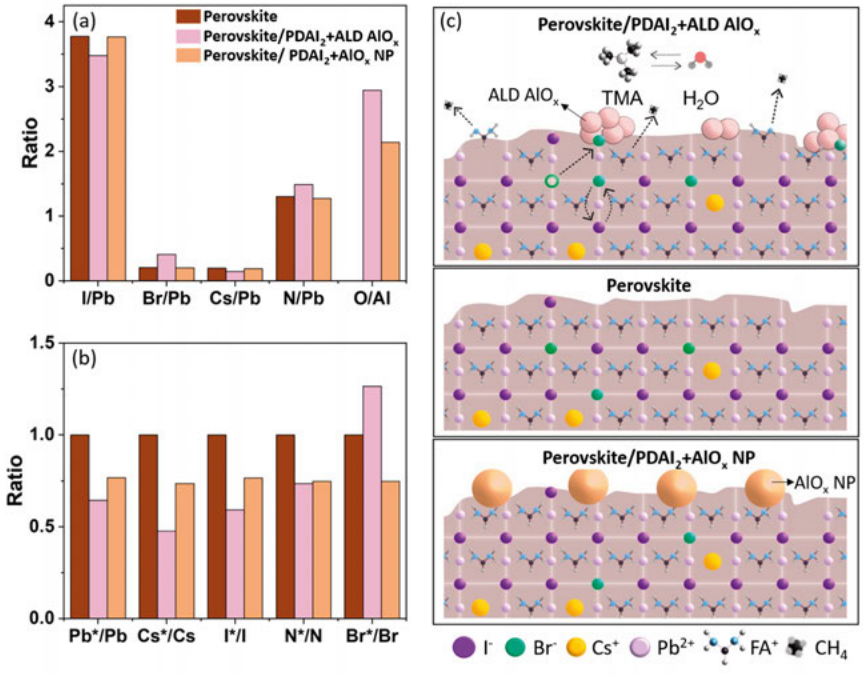

Figure 5.24. (a) Elemental concentration ratios of I/Pb, Br/Pb, Cs/Pb, N/Pb, and O/Al for perovskite, perovskite/$PDAI_2$+ALD AlO_x, and perovskite/$PDAI_2$+AlO_x NP samples. (b) Normalized elemental concentrations of Pb $4f_{7/2}$, Cs $3d_{5/2}$, I $3d_{5/2}$, N 1s, and Br $3d_{5/2}$ core-level peaks for perovskite, perovskite/$PDAI_2$+ALD AlO_x, and perovskite/$PDAI_2$+AlO_x NP samples with respect to those of bare perovskite sample. (c) Illustration of perovskite, and interfaces that form after $PDAI_2$+ALD AlO_x, and $PDAI_2$+AlO_x NP treatments.

5.3.2 Solar Cell Analysis

The p-i-n structure shown in **Figure 5.25(a)** was employed to investigate the impact of interfacial treatments on the solar cell performance. The PSCs that did not employ any interfacial treatment are referred to as the "control". J-V characteristics and box plots of PCE, V_{OC}, and *FF* for the control PSC, as well as for the PSCs incorporating $PDAI_2$, $PDAI_2$+ALD AlO_x, and $PDAI_2$+AlO_x NP treatments between the perovskite and C_{60} are provided in **Figure 5.25**. The V_{OC} and *FF* values were significantly influenced by the employed interfacial treatment. The highest V_{OC} was obtained for the $PDAI_2$+AlO_x NP-treated PSC, followed by $PDAI_2$-treated PSC, $PDAI_2$+ALD AlO_x-treated PSC, and control PSC. $PDAI_2$+ALD AlO_x-treated PSCs exhibited lower *FF* values, irrespective of the utilized thickness, whereas remaining PSCs demonstrated comparable *FF* values. Overall, the $PDAI_2$-treated, and $PDAI_2$+AlO_x

NP-treated PSCs demonstrated comparable PCE values of ~22.94% and ~23.12%, respectively. In contrast, $PDAI_2$+ALD AlO_x-treated PSC displayed a slightly lower PCE. However, both $PDAI_2$+ALD AlO_x-treated, and $PDAI_2$+AlO_x NP-treated PSCs display considerable improvements in the maximum power point (MPP) stability, as shown in **Figure 5.25(f)**. The PCE value of the $PDAI_2$-treated PSC dropped by 6% relative to its initial value during its early operation, whereas the $PDAI_2$+AlO_x NP-treated PSC retained its initial PCE, and the $PDAI_2$+ALD AlO_x-treated PSC witnessed a decrease of only 1% relative to its initial value.

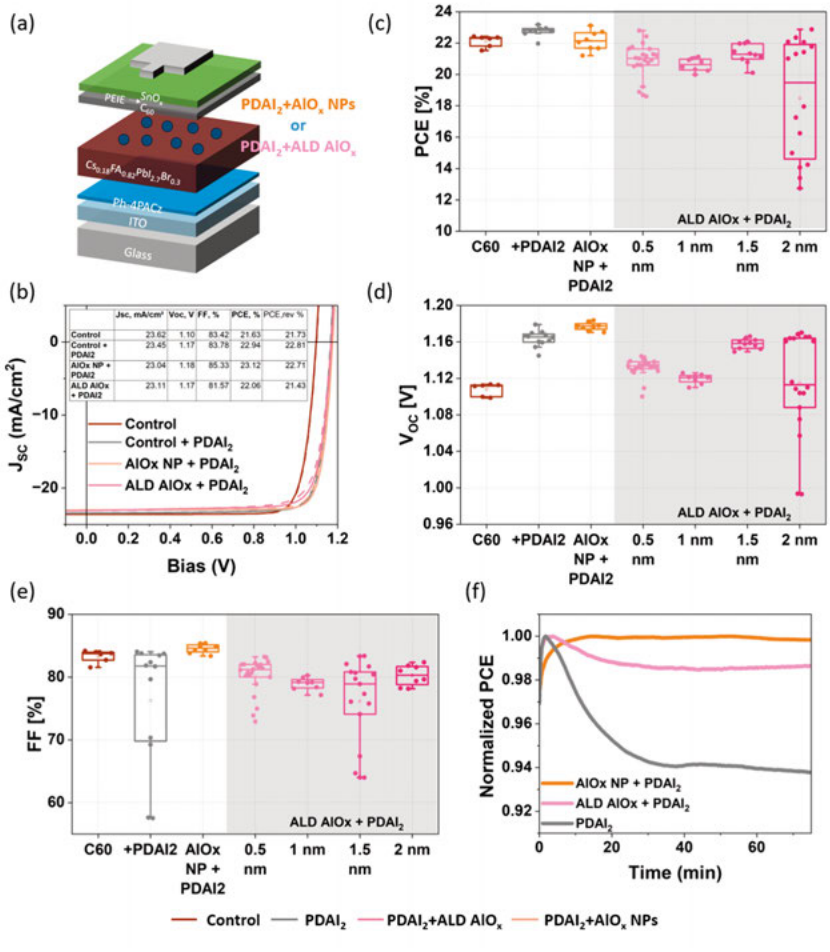

Figure 5.25. (a) Illustration of the employed PSC stack and the corresponding (b) J-V characteristics, and box plots representing (c) PCE (d) V_{OC}, and (e) *FF* distribution. (f) Short-term maximum power point (MPP) tracking on $PDAI_2$, $PDAI_2$+ALD AlO_x, and $PDAI_2$+AlO_x NP-treated PSCs.

Since the direct contact between perovskite and C_{60} is linked to the creation of deep traps,[73] the incorporation of interfacial treatments between perovskite and C_{60} could be beneficial for minimizing the non-radiative recombination and consequently improving the V_{OC} within the p-i-n PSC. XPS measurements revealed that the application of $PDAI_2$+AlO_x NP treatment causes attenuation of the core-level signals originating from the underlying perovskite without inducing any chemical alterations. The $PDAI_2$+AlO_x NP treatment could effectively limit the electronic wavefunction overlap between the perovskite and C_{60}, and consequently improve V_{OC}, as observed in the PSC analysis. In contrast, the $PDAI_2$+ALD AlO_x treatment could also limit the direct contact between the perovskite and C_{60}; however, it comes at the cost of chemical alterations, including the formation of Al-Br species and deprotonation of the FA^+ cation. Therefore, $PDAI_2$+ALD AlO_x-treated PSC might worsen the *FF* value.

6 Conclusion and Outlook

Metal halide perovskite solar cells are highly efficient and are on their way to commercialization. The major challenges currently include limited stability and scalability while maintaining high performance. This thesis work focuses on the development of p-i-n solar cell structures, owing to their relevance for 2-terminal tandem structures and the possibility of depositing all layers using industry-relevant techniques. In particular, the electron transport layer (ETL) side of the structure is investigated and developed. The ETL part of the stack is relatively complicated and requires multiple layers to achieve the desired performance, making it crucial to study each layer separately as well as the interfaces that form between these layers. The best-performing p-i-n perovskite solar cells (PSCs) consist of a combination of C_{60} and SnO_x, deposited using evaporation and atomic layer deposition (ALD) techniques, respectively.

In **PAPER I**, the effect of varying the ALD process parameters used for SnO_x growth on the performance of PSCs was investigated. The results highlighted the importance of the co-reactant doses on both the material properties and the PSC performance. In an ideal ALD process, once the saturation region has been identified, precursor and co-reactant doses should not influence the thin-film properties. However, the SnO_x properties were found to vary significantly as a function of the co-reactant dose at the employed deposition temperature of 100 °C. Higher doses of the H_2O co-reactant resulted in higher growth per cycle (GPC) values, where the obtained SnO_x films exhibited higher film density values and a lower concentration of residual ligand impurities from the Sn-precursor. Simultaneously, the SnO_x layer grown using a high H_2O dose enabled a maximum power conversion efficiency (PCE) of 18.95% when incorporated into PSCs employing evaporated perovskite absorbers, whereas the PCE decreased significantly to 11.3% when SnO_x grown using a low H_2O dose was used. This effect has been hypothesized to be linked to the high concentration of charge traps present in the SnO_x layer grown using a low H_2O dose, as well as to its slightly lower electron affinity value. Both of which hinder the transport of generated charge carriers and negatively affect the short-circuit current (J_{SC}) and fill factor (FF) values. The established correlation

between the co-reactant dose, material properties, and device performance will act as a guide for the scientific community to develop and optimize the SnO_x ALD process for its incorporation into p-i-n PSCs.

In **PAPER II**, the influence of the direct deposition of SnO_x on $FAPbI_3$ and $FAPbBr_3$ was investigated using X-ray photoelectron spectroscopy (XPS), as the elimination of an intermediate C_{60} layer could provide a simpler and more cost-effective solution. ALD is preferred as it enables better conformality even on very rough surfaces in comparison to the evaporation technique. However, the XPS results revealed the existence of unwanted interfacial reactions between the Sn-precursor, tetrakis(dimethylamido)tin (TDMASn), and the perovskite surface, while the perovskite bulk remained unaffected. The results indicated the existence of two different decomposition pathways, with the formation of PbI_2 in the case of $FAPbI_3$ and the formation of Sn-Br bonds for $FAPbBr_3$. Furthermore, the FA^+ cation underwent deprotonation and degradation, leading to the formation of triazine rings and HCN species. The resulting interface was found to introduce an electron transport barrier in both $FAPbI_3$ and $FAPbBr_3$ PSCs, thus leading to poor device performance. The paper clearly disentangled the impact of different halide ions (I^- and Br^-), as well as the FA^+ cation toward the interface formation between the perovskite and SnO_x layers. The results further highlighted the importance of minimizing contact between $FAPbI_3$ and the TDMASn precursor, as such contact led to $FAPbI_3$ decomposition and the formation of the undesired δ-phase.

In **PAPER III**, the *in situ* growth of SnO_x was performed on $FAPbI_3/C_{60}$, $(Cs,FA)Pb(I,Br)_3/C_{60}$, and $FAPbBr_3/C_{60}$ structures to evaluate if an intermediate C_{60} layer could sufficiently protect the underling perovskite surface from the above-mentioned reactions. Ambient-pressure XPS results indicated the occurrence of composition-dependent halide migration through the C_{60} layer into the SnO_x matrix during the ALD process, triggered by exposure to the TDMASn precursor. No migration was observed in iodine-only $FAPbI_3/C_{60}$, whereas both Br-containing perovskites demonstrated halide migration during the SnO_x ALD. The halide migration was hypothesized to be linked to reactions between Sn-precursor-related products and the perovskite surface through defects, thinner C_{60} regions, or the C_{60} bulk. Furthermore, the SnO_x was found to exhibit different thicknesses and stoichiometries for the same number of ALD cycles on top of different perovskite/C_{60} structures. This effect could to be linked to varying halide migration dynamics, leading to the formation of Sn-Br bonds and the consequent blocking of surface sites for ligand exchange during subsequent H_2O exposures. Importantly, the identified

bromine migration occurring during the ALD process could be mitigated by incorporating the 2D-$(PEA)_2PbBr_4$ perovskite between the $FAPbBr_3$ and C_{60} layers. Thus, the results indicated the importance of developing targeted interfacial strategies for PSCs employing Br-rich perovskite absorbers to suppress bromine migration during the SnO_x ALD.

As the final strategy, in **PAPER IV**, aluminum oxide (AlO_x) grown by ALD was incorporated between the $(Cs,FA)Pb(I,Br)_3$ perovskite and C_{60} as an interfacial layer. The interaction between the Al-precursor, trimethylaluminum (TMA), and the perovskite surface was investigated using XPS. Concurrently, AlO_x nanoparticle (NP) treatment was studied as an alternative to ALD-grown AlO_x to distinguish the effects of the ALD process from those of the AlO_x material itself. The XPS results indicated the formation of new nitrogen, carbon, and bromine chemical environments following the ALD of AlO_x on the $(Cs,FA)Pb(I,Br)_3$ surface, whereas no chemical changes relative to the bare sample were detected following the application of AlO_x NP treatment. The changes observed after the AlO_x ALD on $(Cs,FA)Pb(I,Br)_3$ were consistent with some of the changes previously observed for SnO_x ALD on perovskite, including the deprotonation of the FA^+ cation. Furthermore, the modifications observed for bromine were hypothesized to be associated with Al-Br bond formation resulting from an interaction between TMA and the perovskite surface. Finally, PSCs incorporating either ALD-grown AlO_x or AlO_x NP treatments, together with propane-1,3-diammonium iodide ($PDAI_2$), were characterized. The treatments significantly influenced the resulting V_{OC} and *FF* values of the PSCs. PSCs treated with ALD-grown AlO_x exhibited V_{OC} values similar to those of the reference PSCs, whereas AlO_x NP-treated PSCs exhibited a slightly higher V_{OC} value. However, the PSCs treated with ALD-grown AlO_x demonstrated lower *FF* values, while all other PSCs showed similar values. The lower *FF* was hypothesized to be a consequence of the surface alterations revealed by XPS following the AlO_x ALD on $(Cs,FA)Pb(I,Br)_3$. Importantly, both AlO_x treatments improved the maximum power point stability. PSCs treated with AlO_x retained their power conversion efficiencies (PCEs) during the early operation, with only a 1% decrease relative to the initial PCE for the PSC treated with ALD-grown AlO_x, and no loss for the AlO_x NP-treated PSC. In contrast, the reference PSC suffered a substantial 6% decrease relative to the initial PCE.

The thesis systematically developed and optimized the SnO_x ALD process for PSCs and identified the non-idealities originating from the reactive nature of the Sn-precursor. In addition, PSCs were found to be more stable when an

additional AlO_x interfacial treatment was employed between the perovskite and C_{60} layers. To achieve high performance and stability, the ETL stack requires multiple processing steps, thereby increasing the complexity of the fabrication process. Therefore, further development of PSCs requires C_{60}-free ETLs that can protect the underlying perovskite during the ALD of SnO_x, while also eliminating the need for interfacial treatments at the perovskite/C_{60} interface to improve device performance and stability. This could enable cost-effective fabrication, reduce stack complexity, and simplify the fabrication process. Recent work has demonstrated a high efficiency (>25%) even with the C_{60} layer eliminated from the PSC stack. This was achieved by modifying the SnO_x ALD process by tuning the ratio of TDMASn to H_2O doses, together with the use of a suitable spin-coated organic passivation layer prior to the SnO_x ALD.[116] In the future, C_{60}-free interlayers should be developed using industry-relevant techniques, such as ALD or evaporation, that not only passivate the perovskite surface, but also provide functional groups that facilitate the binding of SnO_x ALD precursors and enable the formation of a dense film.

7 Acknowledgments

This Ph.D. journey has been an extraordinary rollercoaster filled with unforgettable adventures that will always remain close to my heart. To all the people who have been part of this journey, Thank You.

I am deeply grateful to my supervisor, Dr. Tobias Törndahl, for his support, kindness, and for always creating a calm and fun environment. I cannot truly express how grateful I am for having this PhD opportunity. It has been a true honor and a pleasure to work with you. You were always there to listen, whether I came to you with a scientific question, or a concern, and you created an environment where I always felt comfortable speaking openly. I especially appreciate how open you were to new ideas and how you always encouraged me to explore and implement them. Thank you for the trust, and encouragement throughout these years.

To Prof. Marika Edoff, thank you for your inspiration, your genuine care, for welcoming me into the Solar Cell Technology division, and for always helping me through difficult situations.

My heartfelt thanks to Dr. Adam Hultqvist for his constant help in the lab, his interest and passion for the work, and for daily long chats before going home. I do not know how I would have survived if you weren't around from the very beginning of the PhD. You always made sure that I felt comfortable and welcomed in the division. It also meant a lot to me that you were there with me at the conferences. We shared so many wonderful and fun moments during those trips.

I am equally grateful to Dr. Natalia Martin for her vibrant positivity, for introducing me to synchrotron beamtimes, and for teaching me everything about XPS. I find you inspiring in so many ways, and I truly wish you all the best in life because you genuinely deserve it. I am also so grateful that you made all the beamtimes possible. They were not only full of valuable learning experiences but also so much fun. I really enjoyed the time spent working, having dinners, and discussion with you, Tobias, Adam, and Melike.

I sincerely thank Dr. Maart van Druenen from First Solar ETC for her proactive support in providing samples, as well as Dr. Fredrik Larsson and Dr. Erik Wallin for their collaboration on projects. Without you, this Ph.D. work would not have been possible. I also thank Prof. Gerrit Boschloo and Prof. Erik Johansson for welcoming me into their group in physical chemistry and for making me feel included. Special thanks to Dr. Lars Korte, Dr. Philipp Tockhorn, Dr. Bor Li, Dr. Suresh Maniyarasu, and Christian Reinhardt, who were a wonderful team at HZB, always helping with samples, and instruments, encouraging scientific discussions, and making sure I felt integrated. Prof. Håkan Rensmo, you are a great person, always inspiring and pushing people to do their best. Many thanks for teaching me XPS and for great collaboration throughout the Ph.D.

It was an absolute pleasure to work with the project and diploma students Simon Nilsson, Andréa Nordmark, Peter Mårtensson, and Ingrid Svensson during my PhD projects. Thank you all for your interest, enthusiasm, and support throughout.

I am also thankful to the whole MSL team, especially Dr. Olivier Donzel-Gargand for his willingness to always help with TEM measurements and move projects forward. My gratitude also goes to Amit Patel for his training and assistance with the SEM and XPS setups.

To my dear friends, Dr. Ann Maria James, Dr. Sapna Mudgal, Dr. Trupthi Chonamada, Dr. Shipra Prakash, Dr. Rajdeep Kaur, Dr. Vishakha Singh, Dr. Ramesh Kumar, and Dr. Garima Aggarwal, thank you for keeping me sane, motivated, and supported throughout this journey. You were home away from home: endless talks, banter, celebrating festivals, exploring Uppsala, and doing crazy things together. You will always be close to my heart. Dr. Kostiantyn Sopiha, you have kept all of us entertained by always embracing crazy conversations, and I have truly enjoyed talking and laughing with you. Special thanks to Dr. Rahul Mahavir Varma, Mustafa Aboulsaad, and Dr. Corrado Comparotto for always cheering me up and for their collaborative spirit during projects and courses. To all solar cell technology members, Elizaveta Yakovleva Bengtson, Dr. Ilknur Bayrak Pehlivan, Dr. Paramesh Chandra, Dr. Carl Hägglund, Sanna Jarl, Dr. Jan Keller, Klara Kiselman, Hugo Kvanta, Prof. Jörgen Olsson, Prof. Charlotte Platzer Björkman, Dr. Jonathan Staaf Scragg, Prof. Lars Stolt, and Dr. Uwe Zimmermann, thank you for creating such a warm and welcoming environment. I am also grateful to have met amazing colleagues at physical chemistry, who eventually became friends, Dr.

Hanmandlu Chintam, Svea Marie Stepping, Dr. Bowen Yang, Pranava Pakala, Fiona Treber, Dario Innocenzi, Dr. Priyabrata Sadhukhan, and Dr. Ashok Kumar Kaliamurthy.

Finally, my deepest love and gratitude to my family. To my mother, my pillar of strength: thank you for being by my side every single day through every situation, bridging any physical distance with your presence. To my father: thank you for your constant support, encouragement, and keen interest in my work. To my brother, Akash: you are a true inspiration, and I would not be where I am today without your love and guidance, always showing me the way forward.

Lastly, I am profoundly grateful to my boyfriend, Asad, who has virtually completed this Ph.D. alongside me. Thank you for continuous encouragement, endless patience, and for always standing by my side. I could not have done this without you.

8 Popular Science Summary

Today, electricity production still relies heavily on non-renewable energy sources. These resources are finite, and their use contributes to greenhouse gas emissions, which drive climate change. Fortunately, we have access to an abundant, clean, and free source of energy: the Sun. Solar cells capture sunlight and convert it into electricity. To make solar energy a truly sustainable solution, the solar cells must be affordable, accessible worldwide, manufacturable using simple processes, and result in minimal CO_2 emissions during their production.

This PhD research focuses on the development of an emerging solar cell technology called perovskites. Perovskites are often described as a "miracle material" because they have achieved remarkably high-power conversion efficiencies in just two decades of research, approaching those of established commercial solar technologies. Unlike traditional silicon solar cells, perovskite solar cells are lightweight, flexible, and can be manufactured using simple, and low-temperature processes.

However, high efficiency alone is not enough. Solar cells must also be stable, durable, and scalable for industrial production. These remain the challenges to some extent for perovskite solar cells and highlight the need for a deeper understanding of the factors that limit long-term performance.

A solar cell can be imagined as a sandwich made up of several layers that must work together efficiently. The perovskite layer forms the heart of the device and is responsible for absorbing sunlight. Surrounding transport layers help extract and deliver electrical charges, allowing the solar cell to generate power. In this work, an industry-relevant technique called Atomic Layer Deposition (ALD) was used to create extremely uniform and conformal transport and passivation layers.

In particular, the deposition of tin oxide (SnO_x) using ALD can be chemically aggressive toward the underlying perovskite owing to the reactive nature of reactants used in the ALD process. In this thesis, simple perovskite systems

were examined to highlight the specific chemical reactions that occur between the reactants used during the ALD process of SnO_x and different ions present in the perovskite. The interactions led to the formation of barriers at the interface between the two materials. These barriers trap electrical charges that would otherwise contribute to power generation, thereby reducing device performance. Introducing an additional layer of C_{60}, a material commonly used in perovskite solar cells, prevents the formation of these barriers. However, it also creates new challenges. This research showed that the C_{60} interlayer can reduce the formation of undesirable chemical species to some extent, but it does not completely eliminate degradation processes. When SnO_x was deposited on top C_{60}, halide ions started to migrate from the underlying perovskite layer into the SnO_x layer through the C_{60} layer present in between, with the extent of migration determined by the composition of the perovskite.

In addition, aluminum oxide (AlO_x) grown using ALD was also explored as an in-between layer perovskite and C_{60} layers with the aim of improving device performance and stability. The metal-organic precursor, used during the ALD for AlO_x process, caused changes on the perovskite surface which lowered the performance slightly. However, importantly, devices incorporating AlO_x exhibited more stable performance than those without it, which is a crucial consideration for commercialization.

Although ALD is attractive for industrial applications and well suited for the growth of ultra-thin, conformal layers, the reactivity of the precursors can introduce additional challenges toward the device performance. Overall, this work highlights both the opportunities and challenges associated with integrating ALD-grown metal oxide layers into perovskite solar cells.

9 Populärvetenskaplig sammanfattning

Idag är elproduktionen fortfarande starkt beroende av icke-förnybara energikällor. Dessa resurser är ändliga och deras användning bidrar till utsläpp av växthusgaser som leder till klimatförändringar på jorden. Lyckligtvis har vi tillgång till en oändlig energikälla som är fossilfri och gratis: solen. Solceller fångar upp solljus och omvandlar det till elektricitet. För att solenergi ska vara en verkligt hållbar lösning måste solcellerna vara kostnadseffektiva, tillgängliga över hela världen, kunna tillverkas med enkla processer och ge upphov till minimala CO_2-utsläpp under deras produktion.

Denna avhandling fokuserar på utvecklingen av en framväxande solcellsteknik baserad på perovskitmaterial. Perovskiter beskrivs ofta som ett "mirakelmaterial" eftersom de på bara två decenniers forskning uppnått anmärkningsvärt höga verkningsgrader för omvandling av solljus till elektricitet, jämförbart med dem hos etablerade kommersiella solcellstekniker. Till skillnad från traditionella kiselsolceller är perovskitsolceller lätta, flexibla och kan tillverkas med enkla processer vid låga temperaturer.

Hög verkningsgrad är dock inte tillräckligt. Solceller måste också vara stabila, hållbara och tillverkningen möjlig att skala upp för industriell produktion. Långtidsstabilietet är fortfarande en av de största utmaningarna för perovskitsolceller och understryker behovet av en djupare förståelse av de faktorer som begränsar deras långsiktiga prestanda.

En solcell består av flera lager som måste samverka effektivt för hög verkningsgrad. Perovskitskiktet utgör hjärtat i strukturen och ansvarar för absorptionen av solljus. Omgivande transport- och passiveringsskikt hjälper till att extrahera och transportera elektriska laddningar, vilket gör det möjligt för solcellen att generera elektricitet. I detta arbete användes en industriellt relevant metod, kallad atomlagerdeponering (Atomic Layer Deposition, ALD), för att skapa extremt homogena och konforma transport- och passiveringsskikt.

Särskilt beläggning av tennoxid (SnO_x) med hjälp av ALD visarsig vara kemiskt reaktiv mot det underliggande perovskitskiktet vilket leder till att

barriärer bildas vid gränsytan mellan de två materialen. Dessa barriärer kan fånga elektriska laddningar som annars skulle ha bidragit till solcellernas elproduktion och därmed försämras solcellernas prestanda. Införandet av ett extra lager av C_{60}, ett material som ofta används i perovskitsolceller, förhindrar bildandet av dessa barriärer. Detta skapar dock nya utmaningar. Forskningen visar att C_{60}-mellanskiktet till viss del kan minska antalet oönskade kemiska reaktioner, men att det inte helt eliminerar dessa. Deponeringen av SnO_x visar sig också omedelbart utlösa diffusion av halidjoner från perovskiten in i SnO_x-skiktet, där omfattningen av denna process bestäms av perovskitens sammansättning.

Dessutom undersöktes aluminiumoxid (AlO_x) framställd med hjälp av ALD som en behandling av ytan mellan perovskit- och C_{60}-skikten med syftet att förbättra solcellernas prestanda och stabilitet. De prekursorer som används i ALD-processen för AlO_x modifierar ytan på grund av sin höga reaktivitet så att ett gränsskikt som påverkar solcellernas prestanda negativt bildas. Trots att ALD är en mycket attraktiv metod för industriella tillämpningar och väl lämpad för att framställa tunna och konforma skikt, är det viktigt att prekursorernas reaktivitet kontrolleras och deras kemiska reaktioner förstås.

Sammanfattningsvis belyser detta arbete både möjligheterna och utmaningarna med att integrera metalloxidskikt framställda med ALD i perovskitsolceller.

10 References

(1) *World*. IEA. https://www.iea.org/world/energy-mix (accessed 2026-08-12)

(2) *Renewables 2025 – Analysis*. IEA. https://www.iea.org/reports/renewables-2025 (accessed 2026-05-30)

(3) Kojima, A.; Teshima, K.; Shirai, Y.; Miyasaka, T. Organometal Halide Perovskites as Visible-Light Sensitizers for Photovoltaic Cells. *J. Am. Chem. Soc.* **2009**, *131* (17), 6050–6051. https://doi.org/10.1021/ja809598r

(4) De Wolf, S.; Holovsky, J.; Moon, S.-J.; Löper, P.; Niesen, B.; Ledinsky, M.; Haug, F.-J.; Yum, J.-H.; Ballif, C. Organometallic Halide Perovskites: Sharp Optical Absorption Edge and Its Relation to Photovoltaic Performance. *J. Phys. Chem. Lett.* **2014**, *5* (6), 1035–1039. https://doi.org/10.1021/jz500279b

(5) Steirer, K. X.; Schulz, P.; Teeter, G.; Stevanovic, V.; Yang, M.; Zhu, K.; Berry, J. J. Defect Tolerance in Methylammonium Lead Triiodide Perovskite. *ACS Energy Lett.* **2016**, *1* (2), 360–366. https://doi.org/10.1021/acsenergylett.6b00196

(6) Kang, J.; Wang, L.-W. High Defect Tolerance in Lead Halide Perovskite CsPbBr3. *J. Phys. Chem. Lett.* **2017**, *8* (2), 489–493. https://doi.org/10.1021/acs.jpclett.6b02800

(7) Schmidt-Mende, L.; Dyakonov, V.; Olthof, S.; Ünlü, F.; Lê, K. M. T.; Mathur, S.; Karabanov, A. D.; Lupascu, D. C.; Herz, L. M.; Hinderhofer, A.; Schreiber, F.; Chernikov, A.; Egger, D. A.; Shargaieva, O.; Cocchi, C.; Unger, E.; Saliba, M.; Byranvand, M. M.; Kroll, M.; Nehm, F.; Leo, K.; Redinger, A.; Höcker, J.; Kirchartz, T.; Warby, J.; Gutierrez-Partida, E.; Neher, D.; Stolterfoht, M.; Würfel, U.; Unmüssig, M.; Herterich, J.; Baretzky, C.; Mohanraj, J.; Thelakkat, M.; Maheu, C.; Jaegermann, W.; Mayer, T.; Rieger, J.; Fauster, T.; Niesner, D.; Yang, F.; Albrecht, S.; Riedl, T.; Fakharuddin, A.; Vasilopoulou, M.; Vaynzof, Y.; Moia, D.; Maier, J.; Franckevičius, M.; Gulbinas, V.; Kerner, R. A.; Zhao, L.; Rand, B. P.; Glück, N.; Bein, T.; Matteocci, F.; Castriotta, L. A.; Di Carlo, A.; Scheffler, M.; Draxl, C. Roadmap on Organic–Inorganic Hybrid Perovskite Semiconductors and Devices. *APL Mater.* **2021**, *9* (10), 109202. https://doi.org/10.1063/5.0047616

(8) Goldschmidt, V. M. Die Gesetze der Krystallochemie. *Naturwissenschaften* **1926**, *14* (21), 477–485. https://doi.org/10.1007/BF01507527

(9) Johnsson, M.; Lemmens, P. Perovskites and Thin Films—Crystallography and Chemistry. *J. Phys.: Condens. Matter* **2008**, *20* (26), 264001. https://doi.org/10.1088/0953-8984/20/26/264001

(10) Li, Z.; Yang, M.; Park, J.-S.; Wei, S.-H.; Berry, J. J.; Zhu, K. Stabilizing Perovskite Structures by Tuning Tolerance Factor: Formation of Formamidinium and Cesium Lead Iodide Solid-State Alloys. *Chem. Mater.* **2016**, *28* (1), 284–292. https://doi.org/10.1021/acs.chemmater.5b04107

(11) Doherty, T. A. S.; Nagane, S.; Kubicki, D. J.; Jung, Y.-K.; Johnstone, D. N.; Iqbal, A. N.; Guo, D.; Frohna, K.; Danaie, M.; Tennyson, E. M.; Macpherson, S.; Abfalterer, A.; Anaya, M.; Chiang, Y.-H.; Crout, P.; Ruggeri, F. S.; Collins,

S.; Grey, C. P.; Walsh, A.; Midgley, P. A.; Stranks, S. D. Stabilized Tilted-Octahedra Halide Perovskites Inhibit Local Formation of Performance-Limiting Phases. *Science* **2021**, *374* (6575), 1598–1605. https://doi.org/10.1126/science.abl4890

(12) Kim, M.; Kim, G.-H.; Lee, T. K.; Choi, I. W.; Choi, H. W.; Jo, Y.; Yoon, Y. J.; Kim, J. W.; Lee, J.; Huh, D.; Lee, H.; Kwak, S. K.; Kim, J. Y.; Kim, D. S. Methylammonium Chloride Induces Intermediate Phase Stabilization for Efficient Perovskite Solar Cells. *Joule* **2019**, *3* (9), 2179–2192. https://doi.org/10.1016/j.joule.2019.06.014

(13) Wang, Z.; Zhou, Y.; Pang, S.; Xiao, Z.; Zhang, J.; Chai, W.; Xu, H.; Liu, Z.; Padture, N. P.; Cui, G. Additive-Modulated Evolution of HC(NH2)2PbI3 Black Polymorph for Mesoscopic Perovskite Solar Cells. *Chem. Mater.* **2015**, *27* (20), 7149–7155. https://doi.org/10.1021/acs.chemmater.5b03169

(14) Cahen, D.; Rakita, Y.; Egger, D. A.; Kahn, A. Surface Defects Control Bulk Carrier Densities in Polycrystalline Pb-Halide Perovskites. *Advanced Materials* **2024**, *36* (50), 2407098. https://doi.org/10.1002/adma.202407098

(15) Umebayashi, T.; Asai, K.; Kondo, T.; Nakao, A. Electronic Structures of Lead Iodide Based Low-Dimensional Crystals. *Phys. Rev. B* **2003**, *67* (15), 155405. https://doi.org/10.1103/PhysRevB.67.155405

(16) Tao, S.; Schmidt, I.; Brocks, G.; Jiang, J.; Tranca, I.; Meerholz, K.; Olthof, S. Absolute Energy Level Positions in Tin- and Lead-Based Halide Perovskites. *Nat Commun* **2019**, *10* (1), 2560. https://doi.org/10.1038/s41467-019-10468-7

(17) Prasanna, R.; Gold-Parker, A.; Leijtens, T.; Conings, B.; Babayigit, A.; Boyen, H.-G.; Toney, M. F.; McGehee, M. D. Band Gap Tuning via Lattice Contraction and Octahedral Tilting in Perovskite Materials for Photovoltaics. *J. Am. Chem. Soc.* **2017**, *139* (32), 11117–11124. https://doi.org/10.1021/jacs.7b04981

(18) Prathapani, S.; Bhargava, P.; Mallick, S. Electronic Band Structure and Carrier Concentration of Formamidinium–Cesium Mixed Cation Lead Mixed Halide Hybrid Perovskites. *Appl. Phys. Lett.* **2018**, *112* (9), 092104. https://doi.org/10.1063/1.5016829

(19) Green, M. A.; Ho-Baillie, A.; Snaith, H. J. The Emergence of Perovskite Solar Cells. *Nature Photon* **2014**, *8* (7), 506–514. https://doi.org/10.1038/nphoton.2014.134

(20) Jung, H. S.; Park, N.-G. Perovskite Solar Cells: From Materials to Devices. *Small* **2015**, *11* (1), 10–25. https://doi.org/10.1002/smll.201402767

(21) Altinkaya, C.; Aydin, E.; Ugur, E.; Isikgor, F. H.; Subbiah, A. S.; De Bastiani, M.; Liu, J.; Babayigit, A.; Allen, T. G.; Laquai, F.; Yildiz, A.; De Wolf, S. Tin Oxide Electron-Selective Layers for Efficient, Stable, and Scalable Perovskite Solar Cells. *Advanced Materials* **2021**, *33* (15), 2005504. https://doi.org/10.1002/adma.202005504

(22) Calió, L.; Kazim, S.; Grätzel, M.; Ahmad, S. Hole-Transport Materials for Perovskite Solar Cells. *Angewandte Chemie International Edition* **2016**, *55* (47), 14522–14545. https://doi.org/10.1002/anie.201601757

(23) Zhang, H.; Park, N.-G. Progress and Issues in P-i-n Type Perovskite Solar Cells. *DeCarbon* **2024**, *3*, 100025. https://doi.org/10.1016/j.decarb.2023.100025

(24) Wang, Y.; Duan, L.; Zhang, M.; Hameiri, Z.; Liu, X.; Bai, Y.; Hao, X. PTAA as Efficient Hole Transport Materials in Perovskite Solar Cells: A Review. *Solar RRL* **2022**, *6* (8), 2200234. https://doi.org/10.1002/solr.202200234

(25) Han, W.; Ren, G.; Liu, J.; Li, Z.; Bao, H.; Liu, C.; Guo, W. Recent Progress of Inverted Perovskite Solar Cells with a Modified PEDOT:PSS Hole Transport

Layer. *ACS Appl. Mater. Interfaces* **2020**, *12* (44), 49297–49322. https://doi.org/10.1021/acsami.0c13576
(26) Xu, L.; Chen, X.; Jin, J.; Liu, W.; Dong, B.; Bai, X.; Song, H.; Reiss, P. Inverted Perovskite Solar Cells Employing Doped NiO Hole Transport Layers: A Review. *Nano Energy* **2019**, *63*, 103860. https://doi.org/10.1016/j.nanoen.2019.103860
(27) Suo, J.; Yang, B.; Bogachuk, D.; Boschloo, G.; Hagfeldt, A. The Dual Use of SAM Molecules for Efficient and Stable Perovskite Solar Cells. *Advanced Energy Materials* **2025**, *15* (2), 2400205. https://doi.org/10.1002/aenm.202400205
(28) Wen, J.; Hu, H.; Chen, C.; McMeekin, D. P.; Xiao, K.; Lin, R.; Liu, Y.; Snaith, H. J.; Tang, J.; Paetzold, U. W.; Tan, H. Present Status of and Future Opportunities for All-Perovskite Tandem Photovoltaics. *Nat Energy* **2025**, *10* (6), 681–696. https://doi.org/10.1038/s41560-025-01782-0
(29) *Best Research-Cell Efficiency Chart | Photovoltaic Research | NLR*. https://www.nlr.gov/pv/cell-efficiency (accessed 2026-08-14)
(30) Lim, J.; Park, N.-G.; Il Seok, S.; Saliba, M. All-Perovskite Tandem Solar Cells: From Fundamentals to Technological Progress. *Energy Environ. Sci.* **2024**, *17* (13), 4390–4425. https://doi.org/10.1039/d3ee03638c
(31) Liu, Z.; Lin, R.; Wei, M.; Yin, M.; Wu, P.; Li, M.; Li, L.; Wang, Y.; Chen, G.; Carnevali, V.; Agosta, L.; Slama, V.; Lempesis, N.; Wang, Z.; Wang, M.; Deng, Y.; Luo, H.; Gao, H.; Rothlisberger, U.; Zakeeruddin, S. M.; Luo, X.; Liu, Y.; Grätzel, M.; Tan, H. All-Perovskite Tandem Solar Cells Achieving >29% Efficiency with Improved (100) Orientation in Wide-Bandgap Perovskites. *Nat. Mater.* **2025**, *24* (2), 252–259. https://doi.org/10.1038/s41563-024-02073-x
(32) Zhang, T.; Hu, C.; Yang, S. Ion Migration: A "Double-Edged Sword" for Halide-Perovskite-Based Electronic Devices. *Small Methods* **2020**, *4* (5), 1900552. https://doi.org/10.1002/smtd.201900552
(33) Yang, T.-Y.; Gregori, G.; Pellet, N.; Grätzel, M.; Maier, J. The Significance of Ion Conduction in a Hybrid Organic–Inorganic Lead-Iodide-Based Perovskite Photosensitizer. *Angewandte Chemie International Edition* **2015**, *54* (27), 7905–7910. https://doi.org/10.1002/anie.201500014
(34) van Reenen, S.; Kemerink, M.; Snaith, H. J. Modeling Anomalous Hysteresis in Perovskite Solar Cells. *J. Phys. Chem. Lett.* **2015**, *6* (19), 3808–3814. https://doi.org/10.1021/acs.jpclett.5b01645
(35) Inaguma, Y.; Matsui, Y.; Shan, Y.-J.; Itoh, M.; Nakamura, T. Lithium Ion Conductivity in the Perovskite-Type LiTaO3-SrTiO3 Solid Solution. *Solid State Ionics* **1995**, *79*, 91–97. https://doi.org/10.1016/0167-2738(95)00036-6
(36) Mizusaki, J.; Arai, K.; Fueki, K. Ionic Conduction of the Perovskite-Type Halides. *Solid State Ionics* **1983**, *11* (3), 203–211. https://doi.org/10.1016/0167-2738(83)90025-5
(37) Khan, M. S.; Islam, M. S.; Bates, D. R. Dopant Substitution and Ion Migration in the LaGaO3-Based Oxygen Ion Conductor. *J. Phys. Chem. B* **1998**, *102* (17), 3099–3104. https://doi.org/10.1021/jp972819d
(38) Eames, C.; Frost, J. M.; Barnes, P. R. F.; O'Regan, B. C.; Walsh, A.; Islam, M. S. Ionic Transport in Hybrid Lead Iodide Perovskite Solar Cells. *Nat Commun* **2015**, *6* (1), 7497. https://doi.org/10.1038/ncomms8497
(39) Thiesbrummel, J.; Milić, J. V.; Deibel, C.; Garnett, E. C.; Tao, S.; Kirchartz, T.; Guerrero, A.; Cameron, P.; Tress, W.; Saiful Islam, M.; Ehrler, B. Ion Migration in Perovskite Solar Cells. *Nat Rev Chem* **2026**, *10* (3), 179–195. https://doi.org/10.1038/s41570-025-00790-8

(40) Calado, P.; Telford, A. M.; Bryant, D.; Li, X.; Nelson, J.; O'Regan, B. C.; Barnes, P. R. F. Evidence for Ion Migration in Hybrid Perovskite Solar Cells with Minimal Hysteresis. *Nat Commun* **2016**, *7* (1), 13831. https://doi.org/10.1038/ncomms13831
(41) Ferdani, D. W.; Pering, S. R.; Ghosh, D.; Kubiak, P.; Walker, A. B.; Lewis, S. E.; Johnson, A. L.; Baker, P. J.; Islam, M. S.; Cameron, P. J. Partial Cation Substitution Reduces Iodide Ion Transport in Lead Iodide Perovskite Solar Cells. *Energy Environ. Sci.* **2019**, *12* (7), 2264–2272. https://doi.org/10.1039/c9ee00476a
(42) Pering, S. R.; Cameron, P. J. The Effect of Multiple Ion Substitutions on Halide Ion Migration in Perovskite Solar Cells. *Mater. Adv.* **2022**, *3* (21), 7918–7924. https://doi.org/10.1039/d2ma00619g
(43) Dey, K.; Ghosh, D.; Pilot, M.; Pering, S. R.; Roose, B.; Deswal, P.; Senanayak, S. P.; Cameron, P. J.; Islam, M. S.; Stranks, S. D. Substitution of Lead with Tin Suppresses Ionic Transport in Halide Perovskite Optoelectronics. *Energy Environ. Sci.* **2024**, *17* (2), 760–769. https://doi.org/10.1039/d3ee03772j
(44) Cho, J.; DuBose, J. T.; Le, A. N. T.; Kamat, P. V. Suppressed Halide Ion Migration in 2D Lead Halide Perovskites. *ACS Materials Lett.* **2020**, *2* (6), 565–570. https://doi.org/10.1021/acsmaterialslett.0c00124
(45) Mathew, P.; Cho, J.; Kamat, P. V. Ramifications of Ion Migration in 2D Lead Halide Perovskites. *ACS Energy Lett.* **2024**, *9* (3), 1103–1114. https://doi.org/10.1021/acsenergylett.4c00093
(46) Hu, T.; Becker, T.; Pourdavoud, N.; Zhao, J.; Brinkmann, K. O.; Heiderhoff, R.; Gahlmann, T.; Huang, Z.; Olthof, S.; Meerholz, K.; Többens, D.; Cheng, B.; Chen, Y.; Riedl, T. Indium-Free Perovskite Solar Cells Enabled by Impermeable Tin-Oxide Electron Extraction Layers. *Advanced Materials* **2017**, *29* (27), 1606656. https://doi.org/10.1002/adma.201606656
(47) Hoffmann, L.; Brinkmann, K. O.; Malerczyk, J.; Rogalla, D.; Becker, T.; Theirich, D.; Shutsko, I.; Görrn, P.; Riedl, T. Spatial Atmospheric Pressure Atomic Layer Deposition of Tin Oxide as an Impermeable Electron Extraction Layer for Perovskite Solar Cells with Enhanced Thermal Stability. *ACS Appl. Mater. Interfaces* **2018**, *10* (6), 6006–6013. https://doi.org/10.1021/acsami.7b17701
(48) Raiford, J. A.; Belisle, R. A.; Bush, K. A.; Prasanna, R.; Palmstrom, A. F.; McGehee, M. D.; Bent, S. F. Atomic Layer Deposition of Vanadium Oxide to Reduce Parasitic Absorption and Improve Stability in n–i–p Perovskite Solar Cells for Tandems. *Sustainable Energy Fuels* **2019**, *3* (6), 1517–1525. https://doi.org/10.1039/C9SE00081J
(49) Chen, K.-T.; Hsu, C.-H.; Ren, F.-B.; Wang, C.; Gao, P.; Wu, W.-Y.; Lien, S.-Y.; Zhu, W.-Z. Influence of Annealing Temperature of Nickel Oxide as Hole Transport Layer Applied for Inverted Perovskite Solar Cells. *J. Vac. Sci. Technol. A* **2021**, *39* (6), 062401. https://doi.org/10.1116/6.0001191
(50) Wu, Y.; Yang, X.; Chen, H.; Zhang, K.; Qin, C.; Liu, J.; Peng, W.; Islam, A.; Bi, E.; Ye, F.; Yin, M.; Zhang, P.; Han, L. Highly Compact TiO2 Layer for Efficient Hole-Blocking in Perovskite Solar Cells. *Appl. Phys. Express* **2014**, *7* (5), 052301. https://doi.org/10.7567/APEX.7.052301
(51) Weiß, A.; Popov, G.; Atosuo, E.; Vihervaara, A.; Jalkanen, P.; Vehkamäki, M.; Leskelä, M.; Ritala, M.; Kemell, M. Atomic Layer Deposition of CsI and CsPbI3. *Chem. Mater.* **2022**, *34* (13), 6087–6097. https://doi.org/10.1021/acs.chemmater.2c01202
(52) Artuk, K.; Turkay, D.; Mensi, M. D.; Steele, J. A.; Jacobs, D. A.; Othman, M.; Yu Chin, X.; Moon, S.-J.; Tiwari, A. N.; Hessler-Wyser, A.; Jeangros, Q.;

Ballif, C.; Wolff, C. M. A Universal Perovskite/C60 Interface Modification via Atomic Layer Deposited Aluminum Oxide for Perovskite Solar Cells and Perovskite–Silicon Tandems. *Advanced Materials* **2024**, *36* (21), 2311745. https://doi.org/10.1002/adma.202311745

(53) Lee, Y. H.; Luo, J.; Son, M.-K.; Gao, P.; Cho, K. T.; Seo, J.; Zakeeruddin, S. M.; Grätzel, M.; Nazeeruddin, M. K. Enhanced Charge Collection with Passivation Layers in Perovskite Solar Cells. *Advanced Materials* **2016**, *28* (20), 3966–3972. https://doi.org/10.1002/adma.201505140

(54) Kim, I. S.; Martinson, A. B. F. Stabilizing Hybrid Perovskites against Moisture and Temperature via Non-Hydrolytic Atomic Layer Deposited Overlayers. *J. Mater. Chem. A* **2015**, *3* (40), 20092–20096. https://doi.org/10.1039/C5TA07186K

(55) Wei, H.; Shi, J.; Xu, X.; Xiao, J.; Luo, J.; Dong, J.; Lv, S.; Zhu, L.; Wu, H.; Li, D.; Luo, Y.; Meng, Q.; Chen, Q. Enhanced Charge Collection with Ultrathin AlOx Electron Blocking Layer for Hole-Transporting Material-Free Perovskite Solar Cell. *Phys. Chem. Chem. Phys.* **2015**, *17* (7), 4937–4944. https://doi.org/10.1039/C4CP04902K

(56) Koushik, D.; Jošt, M.; Dučinskas, A.; Burgess, C.; Zardetto, V.; Weijtens, C.; Verheijen, M. A.; Kessels, W. M. M.; Albrecht, S.; Creatore, M. Plasma-Assisted Atomic Layer Deposition of Nickel Oxide as Hole Transport Layer for Hybrid Perovskite Solar Cells. *J. Mater. Chem. C* **2019**, *7* (40), 12532–12543. https://doi.org/10.1039/C9TC04282B

(57) Brinkmann, K. O.; Becker, T.; Zimmermann, F.; Kreusel, C.; Gahlmann, T.; Theisen, M.; Haeger, T.; Olthof, S.; Tückmantel, C.; Günster, M.; Maschwitz, T.; Göbelsmann, F.; Koch, C.; Hertel, D.; Caprioglio, P.; Peña-Camargo, F.; Perdigón-Toro, L.; Al-Ashouri, A.; Merten, L.; Hinderhofer, A.; Gomell, L.; Zhang, S.; Schreiber, F.; Albrecht, S.; Meerholz, K.; Neher, D.; Stolterfoht, M.; Riedl, T. Perovskite–Organic Tandem Solar Cells with Indium Oxide Interconnect. *Nature* **2022**, *604* (7905), 280–286. https://doi.org/10.1038/s41586-022-04455-0

(58) Palmstrom, A. F.; Eperon, G. E.; Leijtens, T.; Prasanna, R.; Habisreutinger, S. N.; Nemeth, W.; Gaulding, E. A.; Dunfield, S. P.; Reese, M.; Nanayakkara, S.; Moot, T.; Werner, J.; Liu, J.; To, B.; Christensen, S. T.; McGehee, M. D.; van Hest, M. F. A. M.; Luther, J. M.; Berry, J. J.; Moore, D. T. Enabling Flexible All-Perovskite Tandem Solar Cells. *Joule* **2019**, *3* (9), 2193–2204. https://doi.org/10.1016/j.joule.2019.05.009

(59) Shen, H.; Omelchenko, S. T.; Jacobs, D. A.; Yalamanchili, S.; Wan, Y.; Yan, D.; Phang, P.; Duong, T.; Wu, Y.; Yin, Y.; Samundsett, C.; Peng, J.; Wu, N.; White, T. P.; Andersson, G. G.; Lewis, N. S.; Catchpole, K. R. In Situ Recombination Junction between P-Si and TiO2 Enables High-Efficiency Monolithic Perovskite/Si Tandem Cells. *Science Advances* **2018**, *4* (12), eaau9711. https://doi.org/10.1126/sciadv.aau9711

(60) Im, J.-H.; Lee, C.-R.; Lee, J.-W.; Park, S.-W.; Park, N.-G. 6.5% Efficient Perovskite Quantum-Dot-Sensitized Solar Cell. *Nanoscale* **2011**, *3* (10), 4088–4093. https://doi.org/10.1039/C1NR10867K

(61) Di Giacomo, F.; Zardetto, V.; D'Epifanio, A.; Pescetelli, S.; Matteocci, F.; Razza, S.; Di Carlo, A.; Licoccia, S.; Kessels, W. M. M.; Creatore, M.; Brown, T. M. Flexible Perovskite Photovoltaic Modules and Solar Cells Based on Atomic Layer Deposited Compact Layers and UV-Irradiated TiO2 Scaffolds on Plastic Substrates. *Advanced Energy Materials* **2015**, *5* (8), 1401808. https://doi.org/10.1002/aenm.201401808

(62) Roelofs, K. E.; Pool, V. L.; Bobb-Semple, D. A.; Palmstrom, A. F.; Santra, P. K.; Van Campen, D. G.; Toney, M. F.; Bent, S. F. Impact of Conformality and Crystallinity for Ultrathin 4 Nm Compact TiO2 Layers in Perovskite Solar Cells. *Advanced Materials Interfaces* **2016**, *3* (21), 1600580. https://doi.org/10.1002/admi.201600580

(63) Shalan, A. E.; Narra, S.; Oshikiri, T.; Ueno, K.; Shi, X.; Wu, H.-P.; Elshanawany, M. M.; Diau, E. W.-G.; Misawa, H. Optimization of a Compact Layer of TiO2via Atomic-Layer Deposition for High-Performance Perovskite Solar Cells. *Sustainable Energy Fuels* **2017**, *1* (7), 1533–1540. https://doi.org/10.1039/C7SE00220C

(64) Wojciechowski, K.; Stranks, S. D.; Abate, A.; Sadoughi, G.; Sadhanala, A.; Kopidakis, N.; Rumbles, G.; Li, C.-Z.; Friend, R. H.; Jen, A. K.-Y.; Snaith, H. J. Heterojunction Modification for Highly Efficient Organic–Inorganic Perovskite Solar Cells. *ACS Nano* **2014**, *8* (12), 12701–12709. https://doi.org/10.1021/nn505723h

(65) Wojciechowski, K.; Leijtens, T.; Siprova, S.; Schlueter, C.; Hörantner, M. T.; Wang, J. T.-W.; Li, C.-Z.; Jen, A. K.-Y.; Lee, T.-L.; Snaith, H. J. C60 as an Efficient N-Type Compact Layer in Perovskite Solar Cells. *J. Phys. Chem. Lett.* **2015**, *6* (12), 2399–2405. https://doi.org/10.1021/acs.jpclett.5b00902

(66) Baena, J. P. C.; Steier, L.; Tress, W.; Saliba, M.; Neutzner, S.; Matsui, T.; Giordano, F.; Jacobsson, T. J.; Kandada, A. R. S.; Zakeeruddin, S. M.; Petrozza, A.; Abate, A.; Nazeeruddin, M. K.; Grätzel, M.; Hagfeldt, A. Highly Efficient Planar Perovskite Solar Cells through Band Alignment Engineering. *Energy Environ. Sci.* **2015**, *8* (10), 2928–2934. https://doi.org/10.1039/C5EE02608C

(67) Lee, S.-U.; Park, H.; Shin, H.; Park, N.-G. Atomic Layer Deposition of SnO2 Using Hydrogen Peroxide Improves the Efficiency and Stability of Perovskite Solar Cells. *Nanoscale* **2023**, *15* (10), 5044–5052. https://doi.org/10.1039/D2NR06884B

(68) Zhang, X.; Zhou, Y.; Chen, M.; Wang, D.; Chao, L.; Lv, Y.; Zhang, H.; Xia, Y.; Li, M.; Hu, Z.; Chen, Y. Novel Bilayer SnO2 Electron Transport Layers with Atomic Layer Deposition for High-Performance α-FAPbI3 Perovskite Solar Cells. *Small* **2023**, *19* (39), 2303254. https://doi.org/10.1002/smll.202303254

(69) Hultqvist, A.; Aitola, K.; Sveinbjörnsson, K.; Saki, Z.; Larsson, F.; Törndahl, T.; Johansson, E.; Boschloo, G.; Edoff, M. Atomic Layer Deposition of Electron Selective SnOx and ZnO Films on Mixed Halide Perovskite: Compatibility and Performance. *ACS Appl. Mater. Interfaces* **2017**, *9* (35), 29707–29716. https://doi.org/10.1021/acsami.7b07627

(70) Palmstrom, A. F.; Raiford, J. A.; Prasanna, R.; Bush, K. A.; Sponseller, M.; Cheacharoen, R.; Minichetti, M. C.; Bergsman, D. S.; Leijtens, T.; Wang, H.-P.; Bulović, V.; McGehee, M. D.; Bent, S. F. Interfacial Effects of Tin Oxide Atomic Layer Deposition in Metal Halide Perovskite Photovoltaics. *Advanced Energy Materials* **2018**, *8* (23), 1800591. https://doi.org/10.1002/aenm.201800591

(71) Hultqvist, A.; Jacobsson, T. J.; Svanström, S.; Edoff, M.; Cappel, U. B.; Rensmo, H.; Johansson, E. M. J.; Boschloo, G.; Törndahl, T. SnOx Atomic Layer Deposition on Bare Perovskite—An Investigation of Initial Growth Dynamics, Interface Chemistry, and Solar Cell Performance. *ACS Appl. Energy Mater.* **2021**, *4* (1), 510–522. https://doi.org/10.1021/acsaem.0c02405

(72) De Bastiani, M.; Armaroli, G.; Jalmood, R.; Ferlauto, L.; Li, X.; Tao, R.; Harrison, G. T.; Eswaran, M. K.; Azmi, R.; Babics, M.; Subbiah, A. S.; Aydin, E.;

Allen, T. G.; Combe, C.; Cramer, T.; Baran, D.; Schwingenschlögl, U.; Lubineau, G.; Cavalcoli, D.; De Wolf, S. Mechanical Reliability of Fullerene/Tin Oxide Interfaces in Monolithic Perovskite/Silicon Tandem Cells. *ACS Energy Lett.* **2022**, *7* (2), 827–833. https://doi.org/10.1021/acsenergylett.1c02148

(73) Warby, J.; Zu, F.; Zeiske, S.; Gutierrez-Partida, E.; Frohloff, L.; Kahmann, S.; Frohna, K.; Mosconi, E.; Radicchi, E.; Lang, F.; Shah, S.; Peña-Camargo, F.; Hempel, H.; Unold, T.; Koch, N.; Armin, A.; De Angelis, F.; Stranks, S. D.; Neher, D.; Stolterfoht, M. Understanding Performance Limiting Interfacial Recombination in Pin Perovskite Solar Cells. *Advanced Energy Materials* **2022**, *12* (12), 2103567. https://doi.org/10.1002/aenm.202103567

(74) Phung, N.; Verheijen, M.; Todinova, A.; Datta, K.; Verhage, M.; Al-Ashouri, A.; Köbler, H.; Li, X.; Abate, A.; Albrecht, S.; Creatore, M. Enhanced Self-Assembled Monolayer Surface Coverage by ALD NiO in p-i-n Perovskite Solar Cells. *ACS Appl. Mater. Interfaces* **2022**, *14* (1), 2166–2176. https://doi.org/10.1021/acsami.1c15860

(75) Park, H.; Jeong, S.; Kim, E.; Shin, S.; Shin, H. Hole-Transporting Vanadium-Containing Oxide (V2O5–x) Interlayers Enhance Stability of α-FAPbI3-Based Perovskite Solar Cells (∼23%). *ACS Appl. Mater. Interfaces* **2022**, *14* (37), 42007–42017. https://doi.org/10.1021/acsami.2c10901

(76) Bae, H.; Charnas, A.; Sun, X.; Noh, J.; Si, M.; Chung, W.; Qiu, G.; Lyu, X.; Alghamdi, S.; Wang, H.; Zemlyanov, D.; Ye, P. D. Solar-Blind UV Photodetector Based on Atomic Layer-Deposited Cu2O and Nanomembrane β-Ga2O3 Pn Oxide Heterojunction. *ACS Omega* **2019**, *4* (24), 20756–20761. https://doi.org/10.1021/acsomega.9b03149

(77) Iivonen, T.; Heikkilä, M. J.; Popov, G.; Nieminen, H.-E.; Kaipio, M.; Kemell, M.; Mattinen, M.; Meinander, K.; Mizohata, K.; Räisänen, J.; Ritala, M.; Leskelä, M. Atomic Layer Deposition of Photoconductive Cu2O Thin Films. *ACS Omega* **2019**, *4* (6), 11205–11214. https://doi.org/10.1021/acsomega.9b01351

(78) Avila, J. R.; Peters, A. W.; Li, Z.; Ortuño, M. A.; Martinson, A. B. F.; Cramer, C. J.; Hupp, J. T.; Farha, O. K. Atomic Layer Deposition of Cu(I) Oxide Films Using Cu(II) Bis(Dimethylamino-2-Propoxide) and Water. *Dalton Trans.* **2017**, *46* (18), 5790–5795. https://doi.org/10.1039/C6DT02572B

(79) Zhang, Z.; Nallan, H. C.; Coffey, B. M.; Ngo, T. Q.; Pramanik, T.; Banerjee, S. K.; Ekerdt, J. G. Atomic Layer Deposition of Cobalt Oxide on Oxide Substrates and Low Temperature Reduction to Form Ultrathin Cobalt Metal Films. *J. Vac. Sci. Technol. A* **2018**, *37* (1), 010903. https://doi.org/10.1116/1.5063669

(80) Wan, Z.; Zhang, T. F.; Zeng, Z.; Xi, B. Atomic Layer Deposition of CoxOy Films: Oxidants versus Composition. *Advanced Materials Interfaces* **2022**, *9* (14), 2200097. https://doi.org/10.1002/admi.202200097

(81) Jošt, M.; Bertram, T.; Koushik, D.; Marquez, J. A.; Verheijen, M. A.; Heinemann, M. D.; Köhnen, E.; Al-Ashouri, A.; Braunger, S.; Lang, F.; Rech, B.; Unold, T.; Creatore, M.; Lauermann, I.; Kaufmann, C. A.; Schlatmann, R.; Albrecht, S. 21.6%-Efficient Monolithic Perovskite/Cu(In,Ga)Se2 Tandem Solar Cells with Thin Conformal Hole Transport Layers for Integration on Rough Bottom Cell Surfaces. *ACS Energy Lett.* **2019**, *4* (2), 583–590. https://doi.org/10.1021/acsenergylett.9b00135

(82) Datta, K.; Branco, B.; Zhao, Y.; Zardetto, V.; Phung, N.; Bracesco, A.; Mazzarella, L.; Wienk, M. M.; Creatore, M.; Isabella, O.; Janssen, R. A. J. Efficient Continuous Light-Driven Electrochemical Water Splitting Enabled by Monolithic Perovskite-Silicon Tandem Photovoltaics. *Advanced Materials Technologies* **2023**, *8* (2), 2201131. https://doi.org/10.1002/admt.202201131

(83) Koushik, D.; Verhees, W. J. H.; Zhang, D.; Kuang, Y.; Veenstra, S.; Creatore, M.; Schropp, R. E. I. Atomic Layer Deposition Enabled Perovskite/PEDOT Solar Cells in a Regular n–i–p Architectural Design. *Advanced Materials Interfaces* **2017**, *4* (18), 1700043. https://doi.org/10.1002/admi.201700043

(84) Koushik, D.; Verhees, W. J. H.; Kuang, Y.; Veenstra, S.; Zhang, D.; Verheijen, M. A.; Creatore, M.; Schropp, R. E. I. High-Efficiency Humidity-Stable Planar Perovskite Solar Cells Based on Atomic Layer Architecture. *Energy Environ. Sci.* **2017**, *10* (1), 91–100. https://doi.org/10.1039/C6EE02687G

(85) Kokkonen, E.; Lopes da Silva, F.; Mikkelã, M.-H.; Johansson, N.; Huang, S.-W.; Lee, J.-M.; Andersson, M.; Bartalesi, A.; Reinecke, B. N.; Handrup, K.; Tarawneh, H.; Sankari, R.; Knudsen, J.; Schnadt, J.; Såthe, C.; Urpelainen, S. Upgrade of the SPECIES Beamline at the MAX IV Laboratory. *J Synchrotron Rad* **2021**, *28* (2), 588–601. https://doi.org/10.1107/S1600577521000564

(86) Kokkonen, E.; Kaipio, M.; Nieminen, H.-E.; Rehman, F.; Miikkulainen, V.; Putkonen, M.; Ritala, M.; Huotari, S.; Schnadt, J.; Urpelainen, S. Ambient Pressure X-Ray Photoelectron Spectroscopy Setup for Synchrotron-Based in Situ and Operando Atomic Layer Deposition Research. *Rev. Sci. Instrum.* **2022**, *93* (1), 013905. https://doi.org/10.1063/5.0076993

(87) Yeh, J. J.; Lindau, I. Atomic Subshell Photoionization Cross Sections and Asymmetry Parameters: $1 \leqslant Z \leqslant 103$. *Atomic Data and Nuclear Data Tables* **1985**, *32* (1), 1–155. https://doi.org/10.1016/0092-640X(85)90016-6

(88) Scofield, J. H. *Theoretical Photoionization Cross Sections from 1 to 1500 keV.*; UCRL-51326; Lawrence Livermore Laboratory, 1973. https://doi.org/10.2172/4545040

(89) Tanuma, S.; Powell, C. J.; Penn, D. R. Calculations of Electron Inelastic Mean Free Paths. V. Data for 14 Organic Compounds over the 50–2000 eV Range. *Surface and Interface Analysis* **1994**, *21* (3), 165–176. https://doi.org/10.1002/sia.740210302

(90) Stoumpos, C. C.; Malliakas, C. D.; Kanatzidis, M. G. Semiconducting Tin and Lead Iodide Perovskites with Organic Cations: Phase Transitions, High Mobilities, and Near-Infrared Photoluminescent Properties. *Inorg. Chem.* **2013**, *52* (15), 9019–9038. https://doi.org/10.1021/ic401215x

(91) Barrier, J.; Beal, R. E.; Gold-Parker, A.; Vigil, J. A.; Wolf, E.; Waquier, L.; Weadock, N. J.; Zhang, Z.; Schelhas, L. T.; Nogueira, A. F.; McGehee, M. D.; Toney, M. F. Compositional Heterogeneity in CsyFA1−yPb(BrxI1−x)3 Perovskite Films and Its Impact on Phase Behavior. *Energy Environ. Sci.* **2021**, *14* (12), 6394–6405. https://doi.org/10.1039/D1EE01184G

(92) Hanusch, F. C.; Wiesenmayer, E.; Mankel, E.; Binek, A.; Angloher, P.; Fraunhofer, C.; Giesbrecht, N.; Feckl, J. M.; Jaegermann, W.; Johrendt, D.; Bein, T.; Docampo, P. Efficient Planar Heterojunction Perovskite Solar Cells Based on Formamidinium Lead Bromide. *J. Phys. Chem. Lett.* **2014**, *5* (16), 2791–2795. https://doi.org/10.1021/jz501237m

(93) Zhang, M.; Zheng, Z.; Fu, Q.; Chen, Z.; He, J.; Zhang, S.; Yan, L.; Hu, Y.; Luo, W. Growth and Characterization of All-Inorganic Lead Halide Perovskite Semiconductor CsPbBr 3 Single Crystals. *CrystEngComm* **2017**, *19* (45), 6797–6803. https://doi.org/10.1039/C7CE01709J

(94) Chu, D.; Jia, B.; Liu, N.; Zhang, Y.; Li, X.; Feng, J.; Pi, J.; Yang, Z.; Zhao, G.; Liu, Y.; Liu, S. (Frank); Park, N.-G. Lattice Engineering for Stabilized Black FAPbI3 Perovskite Single Crystals for High-Resolution x-Ray Imaging at the Lowest Dose. *Science Advances* **2023**, *9* (35), eadh2255. https://doi.org/10.1126/sciadv.adh2255

(95) Sadhanala, A.; Deschler, F.; Thomas, T. H.; Dutton, S. E.; Goedel, K. C.; Hanusch, F. C.; Lai, M. L.; Steiner, U.; Bein, T.; Docampo, P.; Cahen, D.; Friend, R. H. Preparation of Single-Phase Films of CH3NH3Pb(I1–xBrx)3 with Sharp Optical Band Edges. *J. Phys. Chem. Lett.* **2014**, *5* (15), 2501–2505. https://doi.org/10.1021/jz501332v

(96) Xu, K.; Zhou, L.; Chen, X.; Zhang, S.; Guo, X.; Shou, C.; Lin, Z.; Zhang, J.; Chang, J.; Hao, Y. Solvent Engineering Approach Toward Optimized Phase and Morphology of CsPbBr3 Films for Efficient and Stable Planar Perovskite Solar Cells and Photodetectors. *Advanced Energy and Sustainability Research* **2022**, *3* (11), 2200115. https://doi.org/10.1002/aesr.202200115

(97) Szuber, J.; Czempik, G.; Larciprete, R.; Koziej, D.; Adamowicz, B. XPS Study of the L-CVD Deposited SnO2 Thin Films Exposed to Oxygen and Hydrogen. *Thin Solid Films* **2001**, *391* (2), 198–203. https://doi.org/10.1016/S0040-6090(01)00982-8

(98) Park, B.-E.; Park, J.; Lee, S.; Lee, S.; Kim, W.-H.; Kim, H. Phase-Controlled Synthesis of SnOx Thin Films by Atomic Layer Deposition and Post-Treatment. *Applied Surface Science* **2019**, *480*, 472–477. https://doi.org/10.1016/j.apsusc.2019.03.013

(99) Chistiakova, G.; Mews, M.; Wilks, R. G.; Bär, M.; Korte, L. In-System Photoelectron Spectroscopy Study of Tin Oxide Layers Produced from Tetrakis(Dimethylamino)Tin by Plasma Enhanced Atomic Layer Deposition. *J. Vac. Sci. Technol. A* **2018**, *36* (2), 02D401. https://doi.org/10.1116/1.5015967

(100) Gengenbach, T. R.; Major, G. H.; Linford, M. R.; Easton, C. D. Practical Guides for X-Ray Photoelectron Spectroscopy (XPS): Interpreting the Carbon 1s Spectrum. *J. Vac. Sci. Technol. A* **2021**, *39* (1), 013204. https://doi.org/10.1116/6.0000682

(101) Elam, J. W.; Baker, D. A.; Hryn, A. J.; Martinson, A. B. F.; Pellin, M. J.; Hupp, J. T. Atomic Layer Deposition of Tin Oxide Films Using Tetrakis(Dimethylamino) Tin. *Journal of Vacuum Science & Technology A* **2008**, *26* (2), 244–252. https://doi.org/10.1116/1.2835087

(102) Mullings, M. N.; Hägglund, C.; Bent, S. F. Tin Oxide Atomic Layer Deposition from Tetrakis(Dimethylamino)Tin and Water. *Journal of Vacuum Science & Technology A* **2013**, *31* (6), 061503. https://doi.org/10.1116/1.4812717

(103) Li, N.; Cheng, C.; Wei, H.; Liu, H.; Li, X.; Li, W.; Wang, L. Enhanced Efficiency and Stability of Inverted Perovskite Solar Cells by Interfacial Engineering with Alkyl Bisphosphonic Molecules. *RSC Adv.* **2017**, *7* (67), 42105–42112. https://doi.org/10.1039/C7RA07514F

(104) Li, W.; Li, J.; Niu, G.; Wang, L. Effect of Cesium Chloride Modification on the Film Morphology and UV-Induced Stability of Planar Perovskite Solar Cells. *J. Mater. Chem. A* **2016**, *4* (30), 11688–11695. https://doi.org/10.1039/C5TA09165A

(105) Binek, A.; Hanusch, F. C.; Docampo, P.; Bein, T. Stabilization of the Trigonal High-Temperature Phase of Formamidinium Lead Iodide. *J. Phys. Chem. Lett.* **2015**, *6* (7), 1249–1253. https://doi.org/10.1021/acs.jpclett.5b00380

(106) Liang, Y.; Li, F.; Cui, X.; Lv, T.; Stampfl, C.; Ringer, S. P.; Yang, X.; Huang, J.; Zheng, R. Toward Stabilization of Formamidinium Lead Iodide Perovskites by Defect Control and Composition Engineering. *Nat Commun* **2024**, *15* (1), 1707. https://doi.org/10.1038/s41467-024-46044-x

(107) Bracesco, A. E. A.; Jansen, J. W. P.; Xue, H.; Zardetto, V.; Brocks, G.; Kessels, W. M. M.; Tao, S.; Creatore, M. In Situ IR Spectroscopy Studies of Atomic Layer-Deposited SnO2 on Formamidinium-Based Lead Halide Perovskite. *ACS Appl. Mater. Interfaces* **2023**, *15* (31), 38018–38028. https://doi.org/10.1021/acsami.3c05647
(108) Ma, H.; Jia, Y.; Zhu, G.; Zhang, F.; Rhee, S.; Lee, B.; Liu, C. Study of Cyano and Hydroxyl Groups Modification on the Properties of Porous Carbon Nitride Synthesized by Using a Salt Assistant Method. *Appl. Surf. Sci.* **2020**, *507*, 144885. https://doi.org/10.1016/j.apsusc.2019.144885
(109) Enkvist, C.; Lunell, S.; Sjögren, B.; Brühwiler, P. A.; Svensson, S. The C1s Shakeup Spectra of Buckminsterfullerene, Acenaphthylene, and Naphthalene, Studied by High Resolution X-ray Photoelectron Spectroscopy and Quantum Mechanical Calculations. *J. Chem. Phys.* **1995**, *103* (15), 6333–6342. https://doi.org/10.1063/1.470414
(110) Onoe, J. XPS Study of a Photopolymerized C60 Film. *Phys. Rev. B* **1997**, *55* (15), 10051–10056. https://doi.org/10.1103/PhysRevB.55.10051
(111) Johnson, S. A.; White, K. P.; Tong, J.; You, S.; Magomedov, A.; Larson, B. W.; Morales, D.; Bramante, R.; Dunphy, E.; Tirawat, R.; Perkins, C. L.; Werner, J.; Lahti, G.; Velez, C.; Toney, M. F.; Zhu, K.; McGehee, M. D.; Berry, J. J.; Palmstrom, A. F. Improving the Barrier Properties of Tin Oxide in Metal Halide Perovskite Solar Cells Using Ozone to Enhance Nucleation. *Joule* **2023**, *7* (12), 2873–2893. https://doi.org/10.1016/j.joule.2023.10.009
(112) Liu, Y.; Kim, B. J.; Wu, H.; Boschloo, G.; Johansson, E. M. J. Efficient and Stable FAPbBr3 Perovskite Solar Cells via Interface Modification by a Low-Dimensional Perovskite Layer. *ACS Appl. Energy Mater.* **2021**, *4* (9), 9276–9282. https://doi.org/10.1021/acsaem.1c01512
(113) van den Brand, J.; Snijders, P. C.; Sloof, W. G.; Terryn, H.; de Wit, J. H. W. Acid−Base Characterization of Aluminum Oxide Surfaces with XPS. *J. Phys. Chem. B* **2004**, *108* (19), 6017–6024. https://doi.org/10.1021/jp037877f
(114) Artyushkova, K. Misconceptions in Interpretation of Nitrogen Chemistry from X-Ray Photoelectron Spectra. *J. Vac. Sci. Technol. A* **2020**, *38* (3), 031002. https://doi.org/10.1116/1.5135923
(115) Rakheja, B.; Hultqvist, A.; Varma, R. M.; Martin, N. M.; Radetzky, K.; Riva, S.; Johannesson, E.; Cappel, U. B.; Rensmo, H.; Johansson, E. M. J.; Törndahl, T. Interfacial Chemistry between Formamidinium Lead Trihalide Perovskites and Atomic-Layer-Deposited Tin Oxide. *ACS Appl. Energy Mater.* **2025**, *8* (12), 8467–8478. https://doi.org/10.1021/acsaem.5c00968
(116) Gao, D.; Li, B.; Liu, Q.; Zhang, C.; Yu, Z.; Li, S.; Gong, J.; Qian, L.; Vanin, F.; Schutt, K.; Davis, M. A.; Palmstrom, A. F.; Harvey, S. P.; Long, N. J.; Luther, J. M.; Zeng, X. C.; Zhu, Z. Long-Term Stability in Perovskite Solar Cells through Atomic Layer Deposition of Tin Oxide. *Science* **2024**, *386* (6718), 187–192. https://doi.org/10.1126/science.adq8385

Acta Universitatis Upsaliensis

Digital Comprehensive Summaries of Uppsala Dissertations from the Faculty of Science and Technology 2716

Editor: The Dean of the Faculty of Science and Technology

A doctoral dissertation from the Faculty of Science and Technology, Uppsala University, is usually a summary of a number of papers. A few copies of the complete dissertation are kept at major Swedish research libraries, while the summary alone is distributed internationally through the series Digital Comprehensive Summaries of Uppsala Dissertations from the Faculty of Science and Technology. (Prior to January, 2005, the series was published under the title "Comprehensive Summaries of Uppsala Dissertations from the Faculty of Science and Technology".)

Distribution: publications.uu.se
urn:nbn:se:uu:diva-598586

ACTA UNIVERSITATIS
UPSALIENSIS
2026